UNIVERSIDAD DE SEVILLA

ESCUELA TÉCNICA SUPERIOR DE INGENIEROS

PhD Dissertation

BEM and X-FEM models for the study of static and dynamic fracture in magnetoelectroelastic materials

written by

Ramón Rojas Díaz

Ingeniero Industrial

Supervised by

Prof. Dr. Andrés Sáez Pérez

and

Prof. Dr. Felipe García Sánchez

In fulfillment of the requirements for the European Doctorate Mention at the University of Sevilla

Departamento de Mecánica de los Medios Continuos,

Teoría de Estructuras e Ingeniería del Terreno.

Grupo de Teoría de Estructuras

Sevilla, March 2010

Agradecimientos

La presente Tesis Doctoral es el resultado del trabajo realizado durante los últimos años, y en el que de manera directa o indirecta han intervenido muchas personas. Sirvan estas líneas de agradecimiento a todas ellas.

En primer lugar, quisiera expresar mi más sincera gratitud a mis directores de Tesis, Dr. Andrés Sáez Pérez y Dr. Felipe García Sánchez por todo lo que han hecho por mí. No sólo por la confianza que depositaron en mí, hace ya cuatro años, sino por mucho más. Su atención, paciencia y apoyo, así como por la multitud de oportunidades que me han dado a lo largo de este período, que han permitido mi crecimiento como persona y como investigador.

Durante la realización de esta tesis he tenido la oportunidad de colaborar con diversos Grupos de Investigación. Esto no habría sido posible sin la amabilidad del Profesor Chuanzeng Zhang, del *Departamento de Ingeniería Civil de la Universidad de Siegen* (Alemania), del Profesor Natarajan Sukumar, del *Departamento de Ingeniería Civil y Medioambiental de la Universidad de California* (Davis, USA), y del Profesor Mitsunori Denda, del *Departamento de Ingeniería Mecánica y Aeroespacial de la Universidad de Rutgers* (Piscataway, USA). El excelente trato, su atención y la experiencia y conocimientos transmitidos posibilitaron el máximo aprovechamiento de esos períodos de investigación.

Sería injusto no reconocer a mis compañeros y amigos, Dr. Luis Rodríguez de Tembleque Solano, Luis A. Távara Mendoza, Dr. Michael Wünsche, Federico C. Buroni y Gabriel Hattori da Silva, su apoyo y su ayuda

con todas esas cosas que no aparecen directamente en esta tesis, pero sin las cuales este trabajo no habría sido posible. No puedo olvidarme tampoco de María José Rausell, de su infinita paciencia y asistencia con multitud de asuntos burocráticos.

Y por último, pero no menos importante, a mi familia, en especial a mis padres. Es imposible expresar en unas líneas todo lo que han hecho siempre por mí, pero sin ellos y sin su apoyo y plena confianza en mí y en todas las decisiones que he tomado, esta tesis, como tantas otras cosas, tampoco habría sido posible.

Acknowledgements

The present PhD dissertation is the result of the work carried out during the last years and in which many people, directly or indirectly, took part. I would like to express my gratitude to all of them in these lines.

First of all, I would like to express my sincere appreciation to my PhD advisors, Dr. Andrés Sáez Pérez and Dr. Felipe García Sánchez for all they have done for me. Not only for the confidence they had in me, four years ago already, but for much more. Their attention, patience and support, as well as all the opportunities they gave to me along this period, which have enabled my growth as a person and a researcher.

During the realization of this PhD, I had the opportunity to collaborate in several Research Groups. This would not have been possible without the kindness of Professor Chuanzeng Zhang, from *The Civil Engineering Departament of Siegen University* (Germany), of Professor Natarajan Sukumar, from *The Department of Civil and Environmental Engineering of the University of California at Davis* (USA), and of Professor Mitsunori Denda, from *The Department of Mechanical and Aerospace Engineering of Rutgers, The State University of New Jersey* (Piscataway, USA). The excellent treatment, their attention and experience and knowledge shared with me, allowed the maximum use of those research periods.

It would be unfair not to appreciate my colleagues and friends, Dr. Luis Rodríguez de Tembleque Solano, Luis A. Távara Mendoza, Dr. Michael Wünsche, Federico C. Buroni and Gabriel Hattori da Silva, their support and their help in those things which do not appear directly in this thesis, but

were completely necessary to the realization of this work. I can not forget either María José Rausell, her unlimited patience and help with multitude bureaucratic issues.

And last, but not less important, to my family, specially to my parents. It is impossible to express in a few lines all the things they have always done for me, but without them or their support and full confidence in me and all the decisions I have ever made, this thesis, as many other things, would not have been possible either.

Contents

List of Figures

List of Tables

Chapter 1

Introduction

1.1 Motivations and objectives

The durability and structural integrity of materials used in tools and constructions has been a big concern since ancient times. Nevertheless, mankind have generally developed the abilities for the use of any material before having a full knowledge of its behavior.

That fact happens, for example, with composite and piezoelectric materials and, more recently, with magnetoelectroelastic solids, which have been used for a long time and still nowadays, there exists a huge community of scientists who are working in their characterization.

Magnetoelectroelastic solids are a kind of materials which present the ability of converting energy among mechanic, electric and magnetic fields. This feature makes them very interesting for their use in smart structures applications, such as sensors or actuators. These materials do exist in a natural form, such as $YMnO_3$ or $BiMnO_3$ but, for the use in industrial applications, larger values of the coupling properties are needed. In this case, composites of both piezoelectric and elastomagnetic phases are usually

created. In the resulting solid, an electromagnetic coupling appears which is not present in any constitutive phases (Avellaneda and Harshe, 1994; Nan, 1994; Beneviste, 1995)

Piezoelectric and elastomagnetic effects are usually obtained in non-natural materials after a *polarization process*. This feature, as well as the inherent fragility of those material are causes for defects. Moreover, when two materials with different material properties are joint in a composite, the tendency to develop cracks is increased.

Due to the use these materials receive, the presence of defects not only endanger the structural integrity of the magnetoelectroelastic component, but also their function as sensors/actuators, since flaws may distort the energetic exchange among fields and, thus, the information transmitted in the process.

For all the exposed above, the study of fracture mechanics in magneto-electroelastic media is justified in order to understand the fracture mechanisms. For such purpose, some fracture parameters must be calculated, in order to modelize the effects of the presence of a discontinuity in the field variables.

A deep analysis of bidimensional cracked magnetoelectroelastic solids will be carried out and some numerical tools developed. In particular, based on the Boundary Element Method (BEM) and on the Extended Finite Element Method (X-FEM). Both techniques have been proved as powerful tools for the study of fracture mechanics in different kinds of solids.

In this work, three different kind of problems will be studied

- Cracked solids under combined static electromagnetomechanic loads
- Wave scattering by cracks

- Transient analysis of cracked solids subjected to electromagnetomechanic impact loads

In this work, the hypersingular (also called dual) formulation of the BEM (see e.g., Hong and Chen, 1988 and Portela et al., 1992) will be developed and used for the analysis of all those problems. BEM is based on an integral equation formulation, and the dual formulation implies the use of two different integral equations depending on whether the boundary where the integration is carried out is a crack or not. The formulation presented herein will be obtained following the ideas developed by García-Sánchez and co-workers in several works (2005; 2005a; 2005b; 2008a; 2008b) for the study in anisotropic and piezoelectric solids of both static and dynamic problems.

As it will be deeply discussed in this work, the integral equations may present singular integrands, which will be solved by a regularization process analogous to the one developed by García-Sánchez et al. (2004) for anisotropic solids.

BEM formulations requires knowing the so-called *Green's functions* (or *Fundamental Solution*), which will be used to apply the reciprocity theorem. These functions were available in the literature for the static case when this work was carried out (Liu et al., 2001), but not the dynamic ones. They were obtained by the author following a technique based on the application of the *Radon transform* as it will be presented in the present work.

A X-FEM formulation for the study of static fracture in magnetoelectroelastic cracked solids will be also presented. X-FEM requires the use of some enrichment functions depending on the behavior law of the material studied and, for magnetoelectroelastic solids, such functions were not available in the literature when this work started. In this thesis, those functions will be obtained following a similar procedure to the one developed

by Béchet et al. (2009) for piezoelectric cracked solids.

As it will be seen in this document, when the crack is opened, the medium between the crack surfaces conducts the electric and magnetic fields in a different way as the solid does. The assumption of that conductivity is not a closed topic. Actually, three different conditions are usually considered: two ideal and a more realistic one. In most of this work, the ideal impermeable condition has been adopted , but in the last chapter a deeper analysis of the different crack faces boundary conditions will be carried out, analyzing the implications of them in the fracture parameters.

1.2 State of the knowledge

The number of fracture mechanics problems studied by the use of the numerical techniques used in this work is ample. Nevertheless, the hypersingular BEM and X-FEM had never been used for solving either static or dynamic fracture problems in magnetoelectroelastic solids, to the best of the author's knowledge, when this work was performed.

The number of works in which fracture in magnetoelectroelastic solids were analyzed is relatively limited as compared for other materials such as anisotropic or piezoelectric. In this sense, most of the works were analytical or semianalytical and lack the generality of numerical methods.

1.2.1 Static fracture

Related to static fracture, Liu et al. (2001) derived the 2-D Green's functions for anisotropic magnetoelectroelastic solids with a crack as well as the resulting closed-form expressions for the field intensity factors, based on the extended Stroh's formalism, while Gao et al. (2003a,b,c, 2004) pre-

sented analytic solutions for some basic problems. Sih and coworkers (2003a; 2003b; 2003c; 2003) analyzed the he influence of both electromagnetic fields and the volume fraction of the magnetoelectroelastic composite on crack initiation and growth. In works by Wang and Mai (2003; 2004), the analytical expressions for the stresses, electric displacements and magnetic inductions in the vicinity of the crack tip were derived, as well as path-independent integrals. Using such integrals, fracture behavior of magnetoelectroelastic solids was analyzed by Tian and Rajapakse (2005b).

However, all those analytic procedures are restricted to problems involving simple geometries and loading conditions. Thus, numerical methods become necessary for a deeper study and characterization of fracture behavior of magnetoelectroelastic solids.

It is well known that both BEM and X-FEM present significant advantages over other numerical techniques for the analysis of fracture mechanics problems. Actually, the dual BEM formulation was first used in anisotropic materials by Sollero (1994) and Sollero and Aliabadi (1995). Hypersingular integrals appearing in this formulation are treated by the regularization process presented by Portela et al. (1992), which is limited to the use of straight elements. However, Sáez et al. (1995) developed a regularization process in which the shape of the elements is not a limitation anymore. That process was extended for the study of anisotropic and piezoelectric cracked solids in his PhD thesis by García-Sánchez (1995). In the present work, such formulation will be generalized to the magnetoelectroelastic case.

With respect to the X-FEM, it has been proved as a powerful tool for the study of fracture mechanics and it has been successfully applied to solve crack problems by Möes et al. (1999) in isotropic media, Sukumar et al. (2004) in bimaterials, Asadpoure and Mohammadi (2007) in orthotropic ma-

terials, and Béchet et al. (2009) in piezoelectric media. This last formulation will be generalized in this work to the case of magnetoelectroelastic solids, due to the similarities existing between the formulation of behavior laws in both solids.

The analysis of crack face boundary conditions in magnetoelectroelastic fracture is not a closed topic. Most researchers adopt the impermeable conditions, which establishes that the crack is isolated of the electromagnetic fields. In the other hand, permeable condition implies that cracks conduct electric and magnetic fields. However, both assumptions are not completely realistic, and it is possible to say that a consistent crack face boundary condition will be between them.

In works by Wang and Mai (2006) and Wang and Han (2006b), ideal crack faces boundary conditions for a single crack in an infinite domain were analyzed analitically, while Wang and Mai (2007) studied a more realistic boundary condition by the use of a classical finite elements approach.

In this thesis, a new algorithm to solve multiple semipermeable cracks problem using the hypersingular BEM formulation and based in the one developed by Denda (2008) for piezoelectric materials is presented.

1.2.2 Dynamic fracture

The analysis of dynamic fracture is even more limited than in statics. Moreover, in time-harmonic problems the majority of such analysis deals with anti-plane fracture, using semi-analytical solution methods. Zhou and coworkers (2005a; 2005b; 2006a; 2006b; 2008) used the Schmidt method to investigate the dynamic behavior of several configurations of interface cracks in magnetoelectroelastic composites under harmonic elastic anti-plane shear waves. Hu and Li (2005) derived the analytical solution for an anti-plane

Griffith moving crack inside an infinite magnetoelectroelastic medium under the assumption of permeable crack faces and later extended this study to the case of an anti-plane Griffith crack moving at the interface between two dissimilar magnetoelectroelastic media (Hu et al., 2006).

With respect transient analysis, most of the works have been carried out by analytical or semi-analytical techniques for antiplane configurations as well. Li (2005) investigated the transient response of a magnetoelectroelastic medium containing a crack along the poling direction subjected to antiplane mechanical and inplane electric and magnetic impacts. Feng and coworkers analyzed the dynamic anti-plane problem for a functionally graded magnetoelectroelastic strip containing an internal crack perpendicular to the boundary, under both magnetoelectrically impermeable or permeable boundary conditions on the crack faces in 2006, and the dynamic behavior induced by a penny-shaped crack in a magnetoelectroelastic layer subjected to prescribed stress or prescribed displacement at the layer surfaces for both impermeable and permeable cracks, in 2007. Su et al. (2007) studied the problem of an arbitrary number of interface cracks between dissimilar magneto-electro-elastic strips under out-of-plane mechanical and in-plane magneto-electrical impacts. Yong and Zhou (2007) considered the transient anti-plane problem of a magnetoelectroelastic strip containing a crack vertical to the boundary. Liang (2008) derived the solution for the dynamic behavior of two parallel symmetric cracks in functionally graded piezoelectric/piezomagnetic materials subjected to harmonic antiplane shear waves. Feng and Pan (2008) investigated the anti-plane problem for an interfacial crack between two dissimilar magnetoelectroelastic plates subjected to anti-plane mechanical and in-plane magneto-electrical impact loadings under different combinations of magnetically and electri-

cally permeable/impermeable surface condictions on the crack. More recently, Sladek et al. (2008) presented a meshless method based on the local Petrov-Galerkin approach for stationary and transient dynamic crack analysis in two-dimensional and three-dimensional axisymmetric magnetoelectroelastic solids with continuously varying material properties. Finally, Zhong et al. (2009) analyzed analytically the transient response of a cracked magnetoelectroelastic material subjected to in-plane sudden impacts.

In this work, the numerical study of dynamic problems will be performed by the use of the BEM. The fundamental solutions or Green's functions play a key role in the formulation and resulting accuracy of the method. Although the 2-D and 3-D dynamic fundamental solutions for anisotropic elastic and piezoelectric media have been studied in detail, dynamic Green's functions for 2-D and 3-D fully anisotropic magnetoelectroelastic materials were still unavailable in the literature to the author's knowledge when this work was done. Thus, the procedure to obtain the time-harmonic fundamental solution will be presented in this work for 2-D and 3-D magnetoelectroelastic solids and implemented in a dual BEM code for bidimensional solids. The importance of these Green's functions is not limited to their use in BEM, but they are also a key ingredient in other analytical and numerical techniques such as eigenstrain approaches or dislocation methods.

To obtain these functions, an extension of the Radon transform technique developed by Wang and Achenbach (1994, 1995) for anisotropic elastic solids will be carried out in order to derive the dynamic Green's functions for 2-D and 3-D anisotropic magnetoelectroelastic media subjected to time-harmonic loading conditions. This procedure had been successfully applied by Denda et al. (2004) and Wang and Zhang (2005) to derive the funda-

mental solutions for dynamic piezoelectricity.

For the transient (time-domain) analysis carried out in this work, the time discretization will be performed by approximating the convolution product by the use of Lubich's quadratures, which require the fundamental solution in terms of the Laplace paramater. This fundamental solution may be obtained following a similar procedure to the one developed for the obtaining of the time-harmonic one, as it will be analyzed in this work. Representative examples of the use of Lubich's quadratures for solving time-domain problems are the viscoelastic and the dynamic poroelastic problems, which have been investigated by Schanz (1999), Gaul and Schanz (1999) and Schanz (2001), or the transient elastodynamic crack analysis of anisotropic solids presented by Zhang (2002b) and García-Sánchez et al. (2008b).

Both time-harmonic and time-domain formulations will be obtained following the ideas presented by García-Sánchez et al. (2005b; 2008a; 2008b) and Sáez et al. (2006) for anisotropic and piezoelectric materials.

1.3 Organization of the document

This document is organized in seven chapters. After this introduction, in the second chapter the fundamentals of magnetoelectroelasticity as well as of the implications of the couplings in the static and dynamic fracture mechanics will be analyzed.

In chapter 3, one of the numerical techniques used in this work will be introduced: the hypersingular formulation of the Boundary Element Method. The method will be briefly described as well as all the fundamental solutions needed for the study of static and dynamic problems. In

chapter 4, the proposed formulation will be validated and several problems will be solved in order to extract some conclusions about the behavior of magnetoelectroelastic solids.

In chapter 5, a second technique, the Extended Finite Element Method will be introduced for the study of static fracture mechanics, and the new crack tip enrichment functions needed for its formulation, derived. Some problems will be solved and the results will be compared with those obtained by the use of the hypersingular formulation of the Boundary Element Method previously described.

In chapters 3 to 5, the ideal impermeable crack face boundary condition is assumed. In chapter 6, however, different crack face boundary conditions such as the permeable and the more realistic semipermeable one will be analyzed for static problems.

Finally, in the seventh and last chapter, the conclusions extracted during the realization of the present work will be summarized and possible future developments proposed.

Chapter 2

Analysis of cracked magnetoelectroelastic solids

2.1 Introduction

In this chapter, a review of the linear elastic fracture mechanics in bidimensional magnetoelectroelastic media will be presented, considering both static and dynamic loading.

First, the behavior of these solids will be described paying special attention to the generalized plane problem and showing the procedure to solve it based in the Stroh's formalism. Some extended variables (also called generalized variables) which allow the treatment of the problem in an elastic-like fashion, will be defined, and both static and dynamic problems will be considered. New fracture parameters involving the electric and magnetic effects will be also defined, and the implications of those effects in both external and crack faces boundary conditions, described

2.2 Governing equations for statics in in magneto-electroelastic media

2.2.1 Governing equations

The magnetoelectroelastic effect consists in the coupling between the elastic, the electric and the magnetic fields. This statement means that, under the action of mechanical loads, both electric and magnetic fields are induced. In the opposite way, if either an electric or a magnetic field are applied, a mechanical deformation is produced, as well as a magnetic or an electric field, respectively. Thus, new variables appear in the behavior law of magnetoelectroelastic solids.

These variables are the electric and magnetic potentials, $\phi(\mathbf{x})$ and $\varphi(\mathbf{x})$, the electric and magnetic fields, $\mathbf{E}(\mathbf{x})$ and $\mathbf{H}(\mathbf{x})$, the electric displacement and magnetic induction, $\mathbf{D}(\mathbf{x})$ and $\mathbf{B}(\mathbf{x})$ and the electric charge density and the electric current density, $f^e(\mathbf{x})$ and $f^m(\mathbf{x})$.

The constitutive equations relating the mechanical stresses and elastic strains with those new variables are given by (see, e.g., Jiang and Pan, 2004; Liu et al., 2001; Soh and Liu, 2005)

$$\sigma_{ij} = c_{ijkl}\varepsilon_{kl} - e_{lij}E_l - h_{lij}H_l \tag{2.1a}$$

$$D_i = e_{ikl}\varepsilon_{kl} + \epsilon_{il}E_l + \beta_{il}H_l \tag{2.1b}$$

$$B_i = h_{ikl}\varepsilon_{kl} + \beta_{il}E_l + \gamma_{il}H_l \tag{2.1c}$$

where all the indices vary from 1 to 3 and σ_{ij} denote the components of the Cauchy stress tensor, D_i the electric displacements and B_i the magnetic inductions; ε_{ij} are the components of the small-strain elastic tensor and E_i and H_i are the electric and magnetic fields, respectively. c_{ijkl}, ϵ_{il} and γ_{il}

are the elastic stiffness tensor, the dielectric permittivities and the magnetic permeabilities, respectively, whereas e_{lij}, h_{lij} and β_{il} are the piezoelectric, piezomagnetic and electromagnetic coupling coefficients, respectively.

Small displacement gradients are assumed, so that the linearized strain-displacement relations hold. The mechanical stresses and the electric and magnetic fields are related with the elastic displacements and the electric and magnetic potentials as follows

$$\varepsilon_{ij} = \frac{1}{2}(u_{i,j} + u_{j,i}) \tag{2.2a}$$

$$E_i = -\phi_{,i} \tag{2.2b}$$

$$H_i = -\varphi_{,i} \tag{2.2c}$$

The summation rule on repeated indices is implied and a comma stands for spatial partial differentiation. The governing equations are given by the equilibrium equations

$$\sigma_{ij,j} = -f_i^{mech} \tag{2.3a}$$

and by the Maxwell equations

$$D_{i,i} = f^e \tag{2.3b}$$

$$B_{i,i} = f^m \tag{2.3c}$$

In which it has been considered the quasi-static assumption of the electric and magnetic fields. Such assumption can be adopted because characteristic frequencies in pure mechanical and pure electromagnetic problems are very different (say by 3 orders of magnitude). Therefore, the changes of

the electromagnetic fields can be assumed to be immediate (Parton and Kudryatsev, 1988).

Following the notation first introduced by Barnett and Lothe (1975) for piezoelectricity, some generalized (also called extended) vectors and tensors are defined so that the problem can be formulated in an elastic-like way. In this way, the displacement vector is extended with the electric and magnetic potentials as

$$u_I = \begin{cases} u_i, & \text{I=1,2,3} \\ \phi, & \text{I=4} \\ \varphi, & \text{I=5,} \end{cases} \tag{2.4}$$

where the lowercase subscripts (elastic) vary from 1 to 3, whereas the uppercase ones (extended) vary from 1 to 5. The external volume forces vector is extended with the electric charge density and the electric current density as follows

$$f_I = \begin{cases} f_i^{mech}, & \text{I=1,2,3} \\ -f^e, & \text{I=4} \\ -f^m, & \text{I=5,} \end{cases} \tag{2.5}$$

The stresses tensor is now extended with the electric displacement and the magnetic induction as

$$\sigma_{Ij} = \begin{cases} \sigma_{ij}, & \text{I=1,2,3} \\ D_j, & \text{I=4} \\ B_j, & \text{I=5,} \end{cases} \tag{2.6}$$

with an associated generalized traction vector corresponding to a unit normal $\mathbf{n} = (n_1, n_2)$ given by

$$p_I = \sigma_{Ij} n_j = \begin{cases} p_i = \sigma_{ij} n_j, & \text{I=1,2,3} \\ D_n = D_j n_j, & \text{I=4} \\ B_n = B_j n_j, & \text{I=5,} \end{cases} \tag{2.7}$$

The strains tensor is generalized with the electromagnetic fields

$$\varepsilon_{Ij} = \begin{cases} \varepsilon_{ij}, & \text{I=1,2,3} \\ -E_j, & \text{I=4} \\ -H_j, & \text{I=5,} \end{cases} \tag{2.8}$$

Thus, equilibrium equations can be expressed as

$$\sigma_{Ij,j} = f_I \tag{2.9}$$

The constitutive equations (2.1) may be then recast is a more compact form to yield

$$\sigma_{Ij} = C_{jIKl} u_{K,l} \tag{2.10}$$

where the material properties have been grouped together into a generalized elasticity tensor defined as

$$C_{iJKl} = \begin{cases} c_{ijkl} & J,K = 1,2,3 \\ e_{lij} & J = 1,2,3;\ K = 4 \\ h_{lij} & J = 1,2,3;\ K = 5 \\ e_{ikl} & J = 4;\ K = 1,2,3 \\ -\epsilon_{il} & J,K = 4 \\ -\beta_{il} & J = 4;\ K = 5 \\ h_{ikl} & J = 5;\ K = 1,2,3 \\ -\beta_{il} & J = 5;\ K = 4 \\ -\gamma_{il} & J,K = 5 \end{cases} \tag{2.11}$$

where the following symmetries hold

$$\begin{gathered} c_{ijkl} = c_{jkil} = c_{ijlk} = c_{klij} \ \ ; \ \ e_{lij} = e_{lji} \\ h_{lij} = h_{lji} \ \ ; \ \ \epsilon_{ij} = \epsilon_{ji} \ \ ; \ \ \beta_{ij} = \beta_{ji} \ \ ; \ \ \gamma_{ij} = \gamma_{ji} \end{gathered} \tag{2.12}$$

and, using the extended notation, that symmetry takes the form

$$C_{iJKl} = C_{lKJi} \tag{2.13}$$

For stable materials, c_{ijkl}, ϵ_{ij} and γ_{ij} are positive definite for any real non-zero tensor $\boldsymbol{\varepsilon}$ and vectors $\mathbf{E}$ and $\mathbf{H}$. i.e.,

$$c_{ijkl}\varepsilon_{ij}\varepsilon_{kl} > 0 \ \ ; \ \ \epsilon_{ij}E_iE_j > 0 \ \ ; \ \ \gamma_{ij}H_iH_j > 0 \tag{2.14}$$

which can be expressed in the extended notation as

$$C_{jIKl}\varepsilon_{Ij}\varepsilon_{Kl} > 0 \tag{2.15}$$

Most common magnetoelectroelastic solids in industrial applications are composites of piezoelectric and elastomagnetic ceramics, in which electromechanical and magnetomechanical couplings have been induced by a polarization process which rearrange the originally isotropic crystalline structures. Thus, anisotropy is an important feature in magnetoelectroelastic materials.

Ting (1996), established for anisotropic materials that, when some terms of the behavior matrix vanish, plane and antiplane problems can be studied separately. This statement can be generalized to magnetoelectroelastic solids and, for such purpose, it is convenient to use the contracted Voigt notation that reduces the fourth-order elastic and third-order piezoelectric and piezomagnetic tensors to second-order matrices. In this way, using the relation between the indices $11 \rightarrow 1$, $22 \rightarrow 2$, $33 \rightarrow 3$, $23 \rightarrow 4$, $31 \rightarrow 5$, $12 \rightarrow 6$, the behavior law given by equation (2.1) may be rewritten in a matrix form. Let us assume now, that some terms of the behavior matrix vanish, being the resulting matrix like the following

$$
\begin{pmatrix} \sigma_{11} \\ \sigma_{22} \\ \sigma_{33} \\ \sigma_{23} \\ \sigma_{13} \\ \sigma_{12} \\ D_1 \\ D_2 \\ D_3 \\ B_1 \\ B_2 \\ B_3 \end{pmatrix} =
\begin{pmatrix}
c_{11} & c_{12} & c_{13} & 0 & 0 & 0 & \dots \\
c_{12} & c_{22} & c_{23} & 0 & 0 & 0 & \dots \\
c_{13} & c_{23} & c_{33} & 0 & 0 & 0 & \dots \\
0 & 0 & 0 & c_{44} & c_{45} & 0 & \dots \\
0 & 0 & 0 & c_{45} & c_{55} & 0 & \dots \\
c_{16} & c_{26} & c_{36} & 0 & 0 & c_{66} & \dots \\
e_{11} & e_{12} & e_{13} & 0 & 0 & e_{16} & \dots \\
e_{21} & e_{22} & e_{23} & 0 & 0 & e_{26} & \dots \\
0 & 0 & 0 & e_{34} & e_{35} & e_{36} & \dots \\
h_{11} & h_{12} & h_{13} & 0 & 0 & h_{16} & \dots \\
h_{21} & h_{22} & h_{23} & 0 & 0 & h_{26} & \dots \\
0 & 0 & 0 & h_{34} & h_{35} & h_{36} & \dots
\end{pmatrix}
$$

$$
\begin{pmatrix}
\dots & e_{11} & e_{21} & 0 & h_{11} & h_{21} & 0 \\
\dots & e_{12} & e_{22} & 0 & h_{12} & h_{22} & 0 \\
\dots & e_{13} & e_{23} & 0 & h_{13} & h_{23} & 0 \\
\dots & 0 & 0 & e_{34} & 0 & 0 & h_{34} \\
\dots & 0 & 0 & e_{35} & 0 & 0 & h_{35} \\
\dots & e_{16} & e_{26} & e_{36} & h_{16} & h_{26} & h_{36} \\
\dots & -\epsilon_{11} & -\epsilon_{12} & 0 & -\beta_{11} & -\beta_{12} & 0 \\
\dots & -\epsilon_{12} & -\epsilon_{22} & 0 & -\beta_{12} & -\beta_{22} & 0 \\
\dots & 0 & 0 & -\epsilon_{33} & 0 & -\beta_{32} & -\beta_{33} \\
\dots & -\beta_{11} & -\beta_{12} & 0 & -\gamma_{11} & -\gamma_{12} & 0 \\
\dots & -\beta_{12} & -\beta_{22} & 0 & -\gamma_{12} & -\gamma_{22} & 0 \\
\dots & 0 & 0 & -\beta_{33} & 0 & 0 & -\gamma_{33}
\end{pmatrix}
\begin{pmatrix} \varepsilon_{11} \\ \varepsilon_{22} \\ \varepsilon_{33} \\ 2\varepsilon_{23} \\ 2\varepsilon_{13} \\ 2\varepsilon_{12} \\ -E_1 \\ -E_2 \\ -E_3 \\ -H_1 \\ -H_2 \\ -H_3 \end{pmatrix}
\tag{2.16}
$$

In that case, $x_1 - x_2$ would be a symmetry plane and the plane and the antiplane problems may be separated yielding to the following behavior laws. For plane problems

$$
\begin{pmatrix} \sigma_{11} \\ \sigma_{22} \\ \sigma_{12} \\ D_1 \\ D_2 \\ B_1 \\ B_2 \end{pmatrix} =
\begin{pmatrix}
c_{11} & c_{12} & c_{16} & e_{11} & e_{21} & h_{11} & h_{21} \\
c_{12} & c_{22} & c_{26} & e_{12} & e_{22} & h_{12} & h_{22} \\
c_{16} & c_{26} & c_{66} & e_{16} & e_{26} & h_{16} & h_{26} \\
e_{11} & e_{12} & e_{16} & -\epsilon_{11} & -\epsilon_{12} & -\beta_{11} & -\beta_{12} \\
e_{21} & e_{22} & e_{26} & -\epsilon_{12} & -\epsilon_{22} & -\beta_{12} & -\beta_{22} \\
h_{11} & h_{12} & h_{16} & -\beta_{11} & -\beta_{12} & -\gamma_{11} & -\gamma_{12} \\
h_{21} & h_{22} & h_{26} & -\beta_{12} & -\beta_{22} & -\gamma_{12} & -\gamma_{22}
\end{pmatrix}
\begin{pmatrix} \varepsilon_{11} \\ \varepsilon_{22} \\ 2\varepsilon_{12} \\ -E_1 \\ -E_2 \\ -H_1 \\ -H_2 \end{pmatrix}
\tag{2.17}
$$

being $\varepsilon_{33} = 0$ and $\sigma_{33} = c_{13}\varepsilon_{11} + c_{23}\varepsilon_{22} + 2c_{36}\varepsilon_{12} - e_{13}E_1 - e_{23}E_2 - h_{13}B_1 - h_{23}B_2$ for plane strain and $\varepsilon_{33} = (-1/c_{33})(c_{13}\varepsilon_{11} + c_{23}\varepsilon_{22} + 2c_{36}\varepsilon_{12} - e_{13}E_1 - e_{23}E_2 - h_{13}B_1 - h_{23}B_2)$ and $\sigma_{33} = 0$ for plain stress.

The antiplane problem law is now given by

$$\begin{pmatrix} \sigma_{23} \\ \sigma_{13} \\ D_3 \\ B_3 \end{pmatrix} = \begin{pmatrix} c_{44} & c_{45} & e_{34} & h_{34} \\ c_{45} & c_{55} & e_{35} & h_{35} \\ e_{34} & e_{35} & -\epsilon_{33} & -\beta_{33} \\ h_{34} & h_{35} & -\beta_{33} & -\gamma_{33} \end{pmatrix} \begin{pmatrix} 2\varepsilon_{23} \\ 2\varepsilon_{13} \\ -E_3 \\ -H_3 \end{pmatrix} \tag{2.18}$$

Let us now remark that the plane stress state, defined as that in which the stress tensor components are contained in a plane is mathematically equivalent to the plane strain state, but modifying the elastic constants as proposed by Lekhnitskii (1963). And, in the same way, an antiplane stress state may be defined as that in which only σ_{13} and σ_{23} are different to zero and independent of x_3.

Most extended magnetoelectroelastic materials present a transversely isotropic behavior. If we assume that $x_1 - x_3$ is the isotropy plane, the behavior law for the plane problem may be rewritten as follows

$$\begin{pmatrix} \sigma_{11} \\ \sigma_{22} \\ \sigma_{12} \\ D_1 \\ D_2 \\ B_1 \\ B_2 \end{pmatrix} = \begin{pmatrix} c_{11} & c_{12} & 0 & 0 & e_{21} & 0 & h_{21} \\ c_{12} & c_{22} & 0 & 0 & e_{22} & 0 & h_{22} \\ 0 & 0 & c_{66} & e_{16} & 0 & h_{16} & 0 \\ 0 & 0 & e_{16} & -\epsilon_{11} & 0 & -\beta_{11} & 0 \\ e_{21} & e_{22} & 0 & 0 & -\epsilon_{22} & 0 & -\beta_{22} \\ 0 & 0 & h_{16} & -\beta_{11} & 0 & -\gamma_{11} & 0 \\ h_{21} & h_{22} & 0 & 0 & -\beta_{22} & 0 & -\gamma_{22} \end{pmatrix} \begin{pmatrix} u_{1,1} \\ u_{2,2} \\ u_{1,2} + u_{2,1} \\ \phi_{,1} \\ \phi_{,2} \\ \varphi_{,1} \\ \varphi_{,2} \end{pmatrix} \tag{2.19}$$

Boundary conditions

Expressions (2.1), (2.2) and (2.3) constitute a differential equations system which needs the application of some boundary conditions to be solved.

These conditions may be

- *Natural boundary conditions*, when the generalized tractions are known in some points of the boundary.

$$p_I(\mathbf{x}_0) = \sigma_{Ij} \cdot n_j|_{\mathbf{x}=\mathbf{x}_0} = \overline{p_I} \quad , \quad if \quad \mathbf{x_0} \in \Gamma_p$$

- *Essential boundary conditions*, when the generalized displacements are known in some points of the boundary.

$$u_I(\mathbf{x}_0) = \overline{u_I} \quad , \quad if \quad \mathbf{x_0} \in \Gamma_u$$

where Γ is the external boundary of the magnetoelectroelastic domain, being $\Gamma = \Gamma_t \bigcup \Gamma_u$ and $\Gamma_t \bigcap \Gamma_u = \emptyset$.

The boundary conditions on the crack surfaces need special considerations and will be analyzed in section 2.4.1.

2.2.2 Solution of the static plane problem in magnetoelectroelastic materials

Liu et al. (2001), by the use of the extended notation introduced above, established the generalized displacements and stresses fields in terms of complex potentials, in an analogous way to the procedure carried out by Suo, Kuo, Barnett and Willis (1992) for piezoelectric materials.

Thus, in a magnetoelectroelastic solid, under generalized plane conditions, extended displacements and stresses, are given by the following expressions

$$u_I = \{u_i, \phi, \varphi\} = 2\mathrm{Re}\left(\sum_{J=1}^{5} A_{IJ} f_J(z_J)\right) \tag{2.20}$$

$$\sigma_{1I} = \{\sigma_{1i}, D_1, B_1\} = -2\mathrm{Re}\left(\sum_{J=1}^{5} B_{IJ}\mu_J f'_J(z_J)\right) \tag{2.21}$$

$$\sigma_{2I} = \{\sigma_{2i}, D_2, B_2\} = 2\mathrm{Re}\left(\sum_{J=1}^{5} B_{IJ} f'_J(z_J)\right) \tag{2.22}$$

where Re stands for the real part, whilst I,J=1,2,4,5 for plane problems and I,J=3,4,5 for antiplane problems.

μ_J, A_{IJ} and B_{IJ} are complex values which can be obtained from the material properties, z_J is the transformation of the real domain into the complex plane ($z_J = x_1 + \mu_J x_2$) to define a point locationand f is an arbitrary analytic function which must be obtained for each problem.

To determine all those complex values, a procedure based in the extension of the Stroh's formalism to magnetoelectroelastic solid will be presented. That extension is analogous to the one developed by Barnett and Lothe (1975) for the piezoelectric case, based on the formulation by Eshelby, Read and Shockley (1953) for anisotropic materials. The tensors $\mathbf{A}$ and $\mathbf{B}$, depending on the materials properties, can be computed from the following eigenvalues problem:

$$\left(\begin{array}{c|c} -\mathbf{L}^{-1}\mathbf{M} & -\mathbf{L}^{-1} \\ \hline \mathbf{Z} - \mathbf{M}^T\mathbf{L}^{-1}\mathbf{M} & -\mathbf{M}^T\mathbf{L}^{-1} \end{array}\right)\left(\begin{array}{c} \mathbf{A}_M \\ \hline \mathbf{B}_M \end{array}\right) = \mu_M \left(\begin{array}{c} \mathbf{A}_M \\ \hline \mathbf{B}_M \end{array}\right) \tag{2.23}$$

with no sum on index M, and being $\mathbf{L}$, $\mathbf{M}$ and $\mathbf{Z}$ the tensors defined as follows

$$\mathbf{Z} := \mathbf{C}_{1IJ1} \quad ; \quad \mathbf{M} := \mathbf{C}_{2IJ1} \quad ; \quad \mathbf{L} := \mathbf{C}_{2IJ2} \tag{2.24}$$

and μ_J, the roots of the characteristic equation of the material, are four complex conjugated pairs, but only the four of them with positive imaginary part are considered in equations (2.20-??).

Let us remark that the existence of the inverse of C_{2IJ2} is guaranteed because of the positive definite character of the behavior matrix as defined in (2.15).

2.3 Governing equations for dynamics in in magnetoelectroelastic media

In those cases where boundary conditions of the problem have a strong dependency on the time variable, inertial effects must be considered in the equations.

In the present work two different dynamic problems have been considered: time-harmonic and general transient problems.

2.3.1 Dynamic governing equations

Considering the time as an independent variable as well as the inertial effects, the extended dynamic behavior law and the kinematic relations are

$$\sigma_{Ij}(x_m,t) = C_{jIKl}\varepsilon_{Ij}(x_m,t) \tag{2.25}$$

$$\varepsilon_{ij}(x_m,t) = \frac{1}{2}[u_{i,j}(x_m,t) + u_{j,i}(x_m,t)] \tag{2.26a}$$

$$E_j(x_m,t) = -\phi_{,j}(x_m,t) \tag{2.26b}$$

$$B_j(x_m,t) = -\varphi_{,j}(x_m,t) \tag{2.26c}$$

while the dynamic equilibrium equation is

$$\sigma_{Ij,j}(x_m,t) + f_I(x_m,t) = \rho\delta^*_{IK}\ddot{u}_K(x_m,t) \tag{2.27}$$

where ρ is the density of the material, the superscript $\cdot$ stands for temporal derivative and δ^*_{JK} is the generalized Kronecker delta, defined by

$$\delta^*_{IK} = \begin{cases} \delta_{JK} & I,K = 1,2 \\ 0 & \text{otherwise} \end{cases} \tag{2.28}$$

Let us remark that, due to the quasi-static assumption for the electric and magnetic fields, no electric nor magnetic inertial effects are considered.

2.3.2 Time-harmonic problem

Time-harmonic problems are those in which all the time dependent variables vary as $\sin(\omega t)$ or $\cos(\omega t)$. Thus, time dependency may be expressed in the form $e^{\pm i\omega t}$, where ω is the angular frequency and i is the unit imaginary number. In this case, only the real or the imaginary part would have a physical meaning. Time-harmonic problems are relevant in elastodynamics since dynamic excitations may be decomposed in a Fourier series expansion, the so-called harmonic expansion. With it, the linear system response may be obtained by the superposition of the response to each of the harmonic terms.

In these problems all the variables, in every point of the space, will be a function of an amplitude and a frequency. Thus, if $\mathbf{v}$ is a generic field variable, its value for an instant of time t may be expressed as

$$\mathbf{v}(x_m, t) = \mathbf{v}(x_m, \omega)e^{\pm i\omega t} \tag{2.29}$$

where $\mathbf{v}(x_m, \omega)$ is the amplitude. With this notation, the extended equilibrium equation can be rewritten as

$$\sigma_{Ij,j}(x_m, \omega) + f_I(x_m, \omega) = -\rho\delta^*_{IK}\omega^2 u_K(x_m, \omega) \tag{2.30}$$

while the extended behavior law and compatibility equations are

$$\sigma_{Ij}(x_m, \omega) = C_{jIKl}\varepsilon_{Ij}(x_m, \omega) \tag{2.31}$$

$$\varepsilon_{ij}(x_m, \omega) = \frac{1}{2}[u_{i,j}(x_m, \omega) + u_{j,i}(x_m, \omega)] \tag{2.32a}$$

$$E_j(x_m, \omega) = -\phi_{,j}(x_m, \omega) \tag{2.32b}$$

$$B_j(x_m, \omega) = -\varphi_{,j}(x_m, \omega) \tag{2.32c}$$

2.4 Linear elastic fracture mechanics in magneto-electroelastic media

In this section, the different crack face boundary conditions which may be considered in magnetoelectroelastic cracked solids will be first presented. After that, the near-tip generalized displacements and stresses fields in a cracked magnetoelectroelastic solid, will be introduced. In those expressions, it will be noticed that the electric and magnetic potentials have, as the mechanical displacement do, a $\sqrt{r}$ behavior, while the electric displacement and magnetic induction present an asymptotic $1/\sqrt{r}$ behavior, as the traditional mechanical stresses in isotropic and anisotropic materials have, being r the distance from the crack tip to the point where the extended displacements and/or extended stresses are being evaluated.

After studying those expressions, the implications of the presence of cracks in dynamic problems will be presented, paying special attention to the diffraction of time-harmonic waves when they impinge on defects.

It will be seen that the variable fields in cracked solids are characterized by certain fracture parameters, the so-called field intensity factors: stress intensity factors (SIF), electric displacement intensity factor (EDIF) and magnetic induction intensity factor (MIIF). In this section, thus, some procedure to calculate them, will be also presented.

2.4.1 Crack face boundary conditions

An important issue that must be considered are the boundary conditions on the crack surfaces. This is not a closed topic and, as in crack problems in other multifield solids such as piezoelectric materials, three different conditions may be considered. Those boundary conditions will be described

briefly in this section, and in deep detail in a chapter 6.

While the mechanical boundary conditions on the crack surfaces for an opening crack is always traction free, the electromagnetic boundary conditions comes in different degrees of shielding the electric displacement and magnetic induction, defined, respectively, by the electric permittivity and by the magnetic permeability of the medium in between the crack faces. Then, noting with " $+$ " and " $-$ " the upper and the lower crack surfaces, a crack along the x_1-axis can be considered as

(i) *Fully impermeable crack.* The normal electric displacement and magnetic induction on the crack surfaces are zero, so

$$D_2^+ = D_2^- = 0 \tag{2.33a}$$

$$B_2^+ = B_2^- = 0 \tag{2.33b}$$

which means that the crack is extended tractions free on its surface.

(ii) *Fully permeable crack.* In this case, the crack does not obstruct any electric or magnetic field, what implies that

$$D_2^+ = D_2^- \;\; ; \;\; \phi^+ - \phi^- = 0 \tag{2.34a}$$

$$B_2^+ = B_2^- \;\; ; \;\; \varphi^+ - \varphi^- = 0 \tag{2.34b}$$

(iii) *Semipermeable crack.* This condition, which gives a more realistic boundary condition for opened cracks, was proposed by Wang and Mai (2006) as a generalization of the one proposed by Hao and Shen (1994) and Parton and Kudryatsev (1988) for piezoelectric solids.

$$D_2^+ = D_2^- \;\; ; \;\; D_2^c(u_2^+ - u_2^-) = -\epsilon_0(\phi^+ - \phi^-) \tag{2.35a}$$

$$B_2^+ = B_2^- \;\; ; \;\; B_2^c(u_2^+ - u_2^-) = -\gamma_0(\varphi^+ - \varphi^-) \tag{2.35b}$$

where, since $D_2^+ = D_2^-$ and $B_2^+ = B_2^-$, the upperindex c has been used to denote either of the crack surfaces. Moreover ϵ_0 is the permittivity of the medium between the crack faces and γ_0 its permeability. Let us remark that the semipermeable boundary condition is reduced to the impermeable one when $\varepsilon_0 = 0$ and $\gamma_0 = 0$, and to the permeable one when the jump in the electric and magnetic potential vanish.

However, the impermeable boundary condition is the most used in the scientific literature and will be the one considered in most of this work.

2.4.2 Crack-tip asymptotic fields

As it has been already said, in magnetoelectroelastic solids some variables appear in the behavior law, different to the only mechanical ones. These variables will present a discontinuity due to the presence of the crack. Moreover, as it has been pointed out above, the generalized displacements and stresses present, respectively, a $\sqrt{r}$ and $1/\sqrt{r}$ behavior, being r the distance to the crack tip. Consequently, some new fracture parameters must be defined. Thus, in a magnetoelectroelastic material, as well as the traditional stress intensity factors (SIF), an electric displacement intensity factor (EDIF) and a magnetic induction intensity factor (MIIF) are needed to model the near tip behavior. All those parameters will receive the generic name of Extended Stress Intensity Factors (ESIF).

In elastic problems, the three crack opening modes I, II and III are identified with a discontinuity in mechanical displacements in the local crack coordinate system. Now, in magnetoelectroelastic problems, the new extended stress intensity factors, which are usually called as K_{IV} and K_V, are related to the jump in the electric and the magnetic potentials.

Under those conditions and if a polar coordinates system (r, θ) with the origin at the crack tip is used (see figure 2.1), the near tip extended displacements fields can be expressed in the following way (see e.g. Wang and Mai, 2003 and, more recently, Rao and Kuna, 2008)

$$u_I(r,\theta) = \sqrt{\frac{2}{\pi}} \mathrm{Re}\left(K_N A_{IM} B_{MN}^{-1} \sqrt{r\left(\cos\theta + \mu_M \sin\theta\right)} \right) \tag{2.36}$$

whereas the stresses fields can be expressed as

$$\sigma_{Ij}(r,\theta) = (-1)^j \sqrt{\frac{1}{2\pi}} \mathrm{Re}\left(K_N B_{IM} B_{MN}^{-1} \frac{\delta_{j1}\mu_M + \delta_{j2}}{\sqrt{r\left(\cos\theta + \mu_M \sin\theta\right)}} \right) \tag{2.37}$$

where the summation over N comprises all the fracture modes: K_I, and K_{II} denote the traditional mechanical SIF, whereas K_{IV} and K_V characterize the jump in the electric and magnetic fields over the crack. In (2.36) and (2.37), the tensors $\mathbf{A}$ and $\mathbf{B}$, depending on the materials properties, can be computed from the eigenvalue problem defined in (2.23).

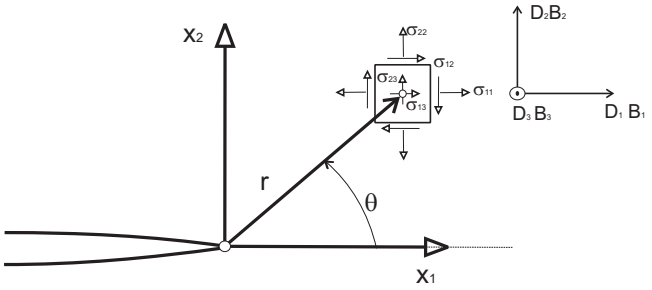

Figure 2.1: Extended stresses and reference system around the crack tip

2.4.3 Near-tip extended displacement fields based on Laurent's series expansion

As it will be studied in chapter 5, the asymptotic terms of the generalized displacement fields in the vicinity of a crack tip must be included in the for-

mulation of the Extended Finite Element Method (X-FEM) to describe the discontinuity imposed by the crack. For this purpose, it is more convenient to derive the asymptotic fields in terms of Laurent's series expansions. The procedure to obtain them, which is similar to the one followed by Scherzer and Kuna (2004) for piezoelectric materials, will be now introduced.

In this work orthotropic magnetoelectroelastic media under generalized plane strain conditions are considered for the X-FEM applications. In such case, the constitutive relations (2.10) may be further reduced (Tian and Rajapakse, 2005c), to

$$\begin{pmatrix} \varepsilon_{11} \\ \varepsilon_{22} \\ 2\varepsilon_{12} \\ E_1 \\ E_2 \\ H_1 \\ H_2 \end{pmatrix} = \begin{pmatrix} a_{11} & a_{12} & 0 & 0 & b_{21} & 0 & d_{21} \\ a_{12} & a_{22} & 0 & 0 & b_{22} & 0 & d_{22} \\ 0 & 0 & a_{33} & b_{13} & 0 & d_{13} & 0 \\ 0 & 0 & -b_{13} & \delta_{11} & 0 & \Delta_{11} & 0 \\ -b_{21} & -b_{22} & 0 & 0 & \delta_{22} & 0 & \Delta_{22} \\ 0 & 0 & -d_{13} & \Delta_{11} & 0 & \zeta_{11} & 0 \\ -d_{21} & -d_{22} & 0 & 0 & \Delta_{22} & 0 & \zeta_{22} \end{pmatrix} \begin{pmatrix} \sigma_{11} \\ \sigma_{22} \\ \sigma_{12} \\ D_1 \\ D_2 \\ B_1 \\ B_2 \end{pmatrix} \tag{2.38}$$

where the terms in the matrix are listed in appendix A.

Let us now introduce some potential functions with the following definitions:

$$\sigma_{11} = U(x_1, x_2)_{,22}, \quad \sigma_{22} = U(x_1, x_2)_{,11}, \quad \sigma_{12} = -U(x_1, x_2)_{,12} \tag{2.39a}$$

$$D_1 = \chi(x_1, x_2)_{,2}, \quad D_2 = -\chi(x_1, x_2)_{,1} \tag{2.39b}$$

$$B_1 = \vartheta(x_1, x2)_{,2}, \quad B_2 = -\vartheta(x_1, x2)_{,1} \tag{2.39c}$$

The equilibrium equations (2.9) are satisfied automatically because of the definitions of the potentials. Substituting (2.38) in the kinematic relations (2.2), and expressing the field variables through the potentials previously defined in equation (2.39), it is possible to obtain

$$
\begin{aligned}
&a_{11}U_{,2222} + a_{22}U_{,1111} + (2a_{12} + a_{33})U_{,1122} \\
&- (b_{21} + b_{13})\chi_{,122} - b_{22}\chi_{,111} \\
&- (d_{21} + d_{13})\vartheta_{,122} - d_{22}\vartheta_{,111} = 0
\end{aligned} \tag{2.40a}
$$

$$
\begin{aligned}
&(b_{21} + b_{13})U_{,122} + b_{22}U_{,111} + \delta_{11}\chi_{,22} + \delta_{22}\chi_{,11} \\
&+ \Delta_{11}\vartheta_{,22} + \Delta_{22}\vartheta_{,11} = 0
\end{aligned} \tag{2.40b}
$$

$$
\begin{aligned}
&(d_{21} + d_{13})U_{,122} + d_{22}U_{,111} + \Delta_{11}\chi_{,22} + \Delta_{22}\chi_{,11} \\
&+ \zeta_{11}\vartheta_{,22} + \zeta_{22}\vartheta_{,11} = 0
\end{aligned} \tag{2.40c}
$$

Defining now the following operators

$$L_4 = a_{22}\frac{\partial^4}{\partial x_1^4} + a_{11}\frac{\partial^4}{\partial x_4^2} + (2a_{11} + a_{33})\frac{\partial^4}{\partial x_1^2 x_2^2} \tag{2.41a}$$

$$L_3 = b_{22}\frac{\partial^3}{\partial x_1^3} + (b_{21} + b_{13})\frac{\partial^4}{\partial x_1 x_2^2} \tag{2.41b}$$

$$M_3 = d_{22}\frac{\partial^3}{\partial x_1^3} + (d_{21} + d_{13})\frac{\partial^4}{\partial x_1 x_2^2} \tag{2.41c}$$

$$L_2 = \delta_{22}\frac{\partial^2}{\partial x_1^2} + \delta_{11}\frac{\partial^2}{\partial x_2^2} \tag{2.41d}$$

$$M_2 = \Delta_{22}\frac{\partial^2}{\partial x_1^2} + \Delta_{11}\frac{\partial^2}{\partial x_2^2} \tag{2.41e}$$

$$P_2 = \zeta_{22}\frac{\partial^2}{\partial x_1^2} + \zeta_{11}\frac{\partial^2}{\partial x_2^2} \tag{2.41f}$$

the compatibility equations can be reduced to a partial differential equation of eight order for $U(x_1, x_2)$ following a similar procedure to the one developed by Sosa (1991) for piezoelectric materials

$$L_4U(x_1,x_2) - L_3\chi(x_1,x_2) - M_3\vartheta(x_1,x_2) = 0 \tag{2.42a}$$

$$L_3U(x_1,x_2) + L_2\chi(x_1,x_2) + M_2\vartheta(x_1,x_2) = 0 \tag{2.42b}$$

$$M_3U(x_1,x_2) + M_2\chi(x_1,x_2) + P_2\vartheta(x_1,x_2) = 0 \tag{2.42c}$$

And solving now in terms of the potential $U(x_1,x_2)$

$$[L_4(L_2P_2 - M_2^2) + L_3(L_3P_2 - 2M_3M_2) + L_2M_3^2]U = 0 \tag{2.43}$$

which solution can be given in the form

$$U(x_1,x_2) = U(x_1 + \mu x_2), \quad \text{with} \quad \mu = \mathrm{Re}(\mu) + i\mathrm{Im}(\mu) \tag{2.44}$$

where μ is a complex number.

Substituting now (2.44) in equation (2.43), the characteristic equation of magnetoelectroelastic media can be expressed as

$$\begin{aligned}&[a_{11}\mu^4 + (2a_{12}+a_{33})\mu^2 + a_{22}][(\Delta_{11}\mu^2+\Delta_{22})^2 - (\delta_{11}\mu^2+\delta_{22})(\zeta_{11}\mu^2+\zeta_{22})]\\ &- [(b_{21}+b_{13})\mu^2 + b_{22}]^2(\zeta_{11}\mu^2+\zeta_{22}) - [(d_{21}+d_{13})\mu^2+d_{22}]^2(\delta_{11}\mu^2+\delta_{22})\\ &+ 2[(b_{21}+b_{13})\mu^2+b_{22}][(d_{21}+d_{13})\mu^2+d_{22}](\Delta_{11}\mu^2+\Delta_{22}) = 0\end{aligned} \tag{2.45}$$

The eight roots of that equation (which are actually four conjugate complex pairs) are the same which can be obtained by solving the eigenvalues problem defined by equation (2.23). The general solution for $U(x_1,x_2)$ can be built up by means of those roots μ_i as

$$U(x_1,x_2) = \sum_{i=1}^{8} U_i(x_1 + \mu_i x_2)$$

And now, since the potentials $\chi(x_1, x_2)$ and $\vartheta(x_1, x_2)$ can be calculated from $U(x_1, x_2)$, every magnetoelectromechanical variable can be obtained by means of the potential $U(x_1, x_2)$ by substituting in the system of equations defined in (2.42).

The generalized displacement solution around the crack tip is now derived in an unbounded domain as the one shown in the figure 2.2, where x_2 is the polarization direction. The material coordinate system is rotated by an angle α so that any polarization direction can be considered. In order to satisfy the considered crack face boundary conditions, it becomes necessary to expand the general solution in Laurent-like series (see Mußchelichwilli, 1971 and Savin, 1968), using general power functions for $U_i(x_1 + \mu_i x_2)$

$$U(x_1, x_2) = \sum_k \sum_{i=1}^{8} d_i(\lambda_k)(x_1 + \mu_i x_2)^{\lambda_k + 2} \tag{2.46}$$

where the origin of the coordinate system has been taken at the crack-tip and $d_i(\lambda_k)$ are free coefficients of the series expansion at the origin and can be obtained only from the overall solution of the considered boundary conditions problem. λ_k are generally complex and represent the number of roots of the solvability equation for the crack faces boundary conditions considered.

Considering now a polar coordinates system (see figure 2.2) with origin at the crack tip, and taking into account that the eight roots μ_i are actually four complex conjugate pairs, the potential $U(r, \theta)$ in (2.46) can be rewritten as

$$U(r,\theta) = \sum_{i=1}^{4} d_i(\lambda) r(\cos(\theta-\alpha) + \mu_i \sin(\theta-\alpha))^{\lambda+2} + \sum_{i=1}^{4} \overline{d_i(\lambda)} r(\cos(\theta-\alpha) + \overline{\mu_i} \sin(\theta-\alpha))^{\lambda+2} \tag{2.47}$$

where μ_i and $\overline{\mu_i}$ must be combined mutually for obtaining a real λ, which would be the combination of two complex λ_k.

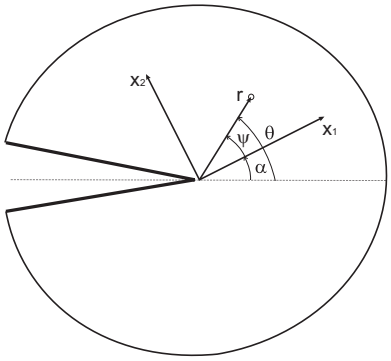

Figure 2.2: Definition of the material axes around the crack tip

The real representation of each term in (2.46) for each pair μ_i and $\overline{\mu_i}$ can be obtained as extension of those obtained by Scherzer and Kuna (2004) for piezoelectric materials and gives expressions as

$$e_i p^{\lambda+2} \cos\left[(\lambda+2)(\kappa+\frac{\pi}{2})\right] + f_i p^{\lambda+2} \sin\left[(\lambda+2)(\kappa+\frac{\pi}{2})\right], \tag{2.48a}$$

with

$$p = r\sqrt{(|\mu_K|^2 - 1)(\sin\psi)^2 + \mathrm{Re}(\mu_i)(\sin 2\psi)} \tag{2.48b}$$

$$\kappa = \arctan\frac{1 + \mathrm{Re}(\mu_i)\tan(\psi)}{|\mathrm{Im}(\mu_i)|\tan(\psi)} \tag{2.48c}$$

$$d_i(\lambda) = e_i(\lambda) + if_i(\lambda) \tag{2.48d}$$

$$\psi = \theta - \alpha \tag{2.48e}$$

If λ_k is complex, then the terms of equations (2.48) must be combined with the resulting terms of considering $\overline{\lambda_k}$, so that real values of $U(x_1, x_2)$ are obtained and, thus, real values of the other potentials $\chi(x_1, x_2)$ and $\vartheta(x_1, x_2)$.

The homogeneous boundary condition at the crack surfaces for an impermeable crack ($\sigma_{\theta\theta}(r, \theta = \pm\pi) = \sigma_{r\theta}(r, \theta = \pm\pi) = 0$, $D_\theta(r, \theta = \pm\pi) = 0$ and $B_\theta(r, \theta = \pm\pi) = 0$) define a linear system of equations for the eight unknown coefficients e_i and f_i and their complex conjugate pairs. Naming $\mathbf{X}$ a vector containing those unknowns variables, the system of equation would have the form

$$\mathbf{S}(\lambda) \cdot \mathbf{X} = 0 \tag{2.49}$$

and now it is necessary to point out that for the impermeable crack face boundary condition considered in most of this work, an infinite number of λ_k can be obtained so that the previous system of equation has a solution

$$\lambda_1 = -1/2; \quad \lambda_2 = 0; \quad \lambda_3 = 1/2; \quad \lambda_4 = 1...$$

A value of $\lambda_1 = -\frac{1}{2}$ generates four independent eigenvectors, based on the coefficients $e_i(\lambda_1)$ and $f_i(\lambda_1)$ (and their respective conjugate complex pairs) so that four independent singular eigenfunctions, which incorporate the classical $1/\sqrt{r}$ crack tip singularity, can be constructed in an analogous

way as done by Béchet et al. (2009) for piezoelectric solids. These independent eigenfunctions shall be used in chapter 5 for obtaining the crack tip enrichment functions needed for the X-FEM formulation.

2.4.4 Wave scattering

Wave propagation is an important topic in solid mechanics. A description of that phenomena was given by Graff (1975): *the effect of a sharply applied, localized disturbance in a medium soon transmits or 'spreads' to other parts of the medium.*

Applications of wave phenomena can be found in nearly every field of engineering. Quantitative non-destructive testing, seismology, geophysics and, as in this work, dynamic fracture mechanics.

Wave scattering phenomenon consists in the superposition of the incident field and the diffracted one. Thus, the process to obtain the solution for this kind of problems is carried out by means of the superposition principle, which is illustrated in figure 2.3. The original problem consists in a wave impinging on a (extended) tractions free crack and can be decomposed into two subproblems. The first one implies a wave traveling along a non-cracked solid, whilst the second one is a crack subjected on its surfaces to a field, equal to the incident one but with the opposite sign.

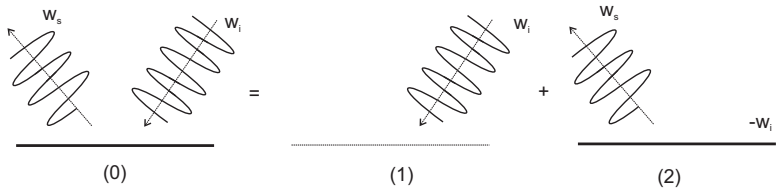

Figure 2.3: Superposition principle applied to wave scattering problems

Let us remark that the scattered wave field must satisfy the radiation condition (Eringen and Suhubi, 1975). BEM presents an important advantage respect to other numerical techniques when dealing with infinite or semi-infinite domains, since only the internal boundaries need to be meshed and the radiation conditions at infinity are automatically satisfied (see, e.g., Dominguez, 1993).

2.4.5 Calculation of extended stress intensity factors

As it has been said, stress intensity factors must be understood now in an extended way (ESIF). There are several methods to determine the ESIF from the numerically computed field variables. The extrapolation method and the interaction integrals approach are next sketched.

- **Stresses or displacement method**

This method, since requires a lower postprocess of the obtained field variables, is the the most direct one. It consists in the substitution of the values of the variables obtained numerically, in the expressions (2.36-2.37), getting some expressions from which is possible to obtain the ESIF.

This method is the one that will be used in all the BEM (static and dynamic) computations performed in this work and will be analyzed in detail in a later section.

- **Interaction integral method**

This method is based on the use of path independent integrals, such as the *J-integral*, which was first introduced by Rice (1968), who defined a path independent line integral which is equal to the unit energy release rate G. Once that integral is evaluated, the computation of the ESIF can be carried

out inmediately. In works by Suo et al. (1992) and Pak (1992) the *J-integral* was extended to piezoelectric materials, while Tian and Rajapakse (2005b) did it for magnetoelectroelastic solids.

Such integrals may be defined for each mechanical fracture modes considered in plane problems as

$$\begin{aligned} J_1 = \oint_C [\frac{1}{2}(\sigma_{ij}\varepsilon_{ij} - D_i E_i - B_i H_i)dx_2 - n_i \sigma_{ip} u_{p,1} ds \\ - n_i D_i \varphi_{,1} ds - n_i B_i \phi_{,1} ds] \end{aligned} \tag{2.50}$$

$$\begin{aligned} J_2 = \oint_C [-\frac{1}{2}(\sigma_{ij}\varepsilon_{ij} - D_i E_i - B_i H_i)dx_1 - n_i \sigma_{ip} u_{p,2} ds \\ - n_i D_i \varphi_{,2} ds - n_i B_i \phi_{,2} ds] \end{aligned} \tag{2.51}$$

where C is any closed line around the crack tip.

The interaction integral method will require the additional use of an auxiliary state which satisfies the boundary conditions of the problem, as well as the actual state under study. The contour *J-integral* for the sum of the two states can be defined as

$$J^{(S)} = J^{(act)} + J^{(aux)} + M \tag{2.52}$$

where $J^{(act)}$ and $J^{(aux)}$ are associated, respectively, with the actual and auxiliary states, while M is the interaction integral. By choosing appropriate auxiliary states, and using the expressions of the *J-integral* in terms of the ESIF, these may be obtained by solving a linear system of equations. This procedure will be exposed in detail in chapter 5, devoted to the X-FEM. In this work, this method will be used in an equivalent domain form.

Chapter 3

Hypersingular formulation of the BEM. Fundamental solutions and numerical implementation

3.1 Introduction

The main objective of this work is to develop BEM models for the study of static and dynamic fracture mechanics problems in magnetoelectroelastic solids. In this chapter, in order to make the document self-contained, the hypersingular formulation of the BEM will be briefly introduced.

It is known as fundamental solution (or Green's function) the displacement solution to the problem of a point load (in an extended sense for magnetoelectroelastic solids) in an infinite domain. The BEM is based in the application of the reciprocity theorem (Betti's theorem for static prob-

lems; Graffi's theorem for dynamic ones), between this problem and the one under consideration. The application of that theorem shall lead to the integral equation that, once it is solved, will provide the sought solution (see for further details works by Brebbia and Domínguez, 1992 and Dominguez, 1993; both for the simply elastic case).

In this chapter the fundamental solution for static problems already available in the literature will be described. Nevertheless, the dynamic Green's functions were not available when this work was carried out, so the obtaining process for it, based on the use of the Radon's transform, will be also described in this chapter.

3.2 The Boundary Element Method (BEM)

Let Ω be a domain with a boundary Γ, as the one showed in figure 3.1. Let us define a reference coordinates system x_i and two compatible loading states, each one defined by a displacement field ($\mathbf{u}$ and $\mathbf{u}^*$), boundary tractions ($\mathbf{p}$ and $\mathbf{p}^*$) and volume forces ($\mathbf{f}$ and $\mathbf{f}^*$). The static reciprocity theorem between both states is

$$\begin{aligned} &\int_\Omega \rho f_I^*(\mathbf{x}) u_I(\mathbf{x})\, d\Omega + \int_\Gamma \rho p_I^*(\mathbf{x}) u_I(\mathbf{x})\, d\Gamma = \\ &= \int_\Omega \rho f_I(\mathbf{x}) u_I^*(\mathbf{x})\, d\Omega + \int_\Gamma \rho p_I(\mathbf{x}) u_I^*(\mathbf{x})\, d\Gamma \end{aligned} \tag{3.1}$$

where ρ is the material density. Let us consider now as the state "*" the corresponding to an infinite domain with an unit point load located in $\boldsymbol{\xi}$. That load, for the static case, takes the form

$$\rho f_I^* = \delta(\mathbf{x} - \boldsymbol{\xi})\delta_{IJ} \tag{3.2}$$

where $\mathbf{x}$ is a generic point in the domain, $\delta(\cdot)$ is the Dirac's delta function, while δ_{IJ} is the Krönecker's delta functions. The displacement and traction solution of that problem can be expressed as

$$u^*_{IJ}(\boldsymbol{\xi}, \mathbf{x}) \qquad ; \qquad p^*_{IJ}(\boldsymbol{\xi}, \mathbf{x}) \tag{3.3}$$

In equation (3.3), the first index indicates the component of the solution vector while the second one denotes the direction in which the loading is applied; $\boldsymbol{\xi}$ is the point where the load is applied (from now on, *collocation point*) while $\mathbf{x}$ is the point where the solution is evaluated (from now on, *observation point*). That solution is known in the whole domain, including the points where the external boundary Γ is located. The equation (3.1) can now be rewritten, when no volumetric forces are involved, as

$$u_J(\xi) + \int_\Gamma p^*_{IJ}(\boldsymbol{\xi}, \mathbf{x}) u_I(\mathbf{x})\, d\Gamma = \int_\Gamma u^*_{IJ}(\boldsymbol{\xi}, \mathbf{x}) p_I(\mathbf{x})\, d\Gamma \tag{3.4}$$

This last equation indicates that, once $u_J(\mathbf{x})$ and $p_J(\mathbf{x})$ are known in the boundary, the values of those field variables may be known in any point of the domain $\boldsymbol{\xi}$. Thus, it is first necessary to know the solution in the boundary.

For such purpose, some transformations must be done in (3.4). A point $\boldsymbol{\xi}$ on the boundary will be taken but, since that point must belong to the domain, the external boundary will be modified with a semicircumference of radius r, whose center is the point $\boldsymbol{\xi}$, as shown in figure 3.1. Once the equation (3.4) is applied, the radius will be taken to zero.

Due to the modification in the external boundary introduced, integrals in equation (3.4) may be decomposed as follows

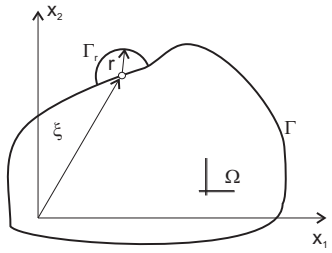

Figure 3.1: Domain modification for the obtaining of the BIE

$$\int_{\Gamma} p^*_{IJ}(\boldsymbol{\xi},\mathbf{x})u_I(\mathbf{x})\,d\Gamma = \int_{\Gamma_r} p^*_{IJ}(\boldsymbol{\xi},\mathbf{x})u_I(\mathbf{x})\,d\Gamma + \\ + \int_{\Gamma-\Gamma_r} p^*_{IJ}(\boldsymbol{\xi},\mathbf{x})u_I(\mathbf{x})\,d\Gamma \tag{3.5}$$

$$\int_{\Gamma} u^*_{IJ}(\boldsymbol{\xi},\mathbf{x})p_I(\mathbf{x})\,d\Gamma = \int_{\Gamma_r} u^*_{IJ}(\boldsymbol{\xi},\mathbf{x})p_I(\mathbf{x})\,d\Gamma + \\ + \int_{\Gamma-\Gamma_r} u^*_{IJ}(\boldsymbol{\xi},\mathbf{x})p_I(\mathbf{x})\,d\Gamma \tag{3.6}$$

Taking now limits in (3.5), the first term becomes

$$\lim_{r\to 0}\int_{\Gamma_r} p^*_{IJ}(\boldsymbol{\xi},\mathbf{x})u_I(\mathbf{x})\,d\Gamma = u_I(\mathbf{x})\lim_{r\to 0}\int_{\Gamma_r} p^*_{IJ}(\boldsymbol{\xi},\mathbf{x})\,d\Gamma = c_{IJ}u_I(\xi) \tag{3.7}$$

where it has been considered that tractions have a $1/r$ behavior when r tends to zero. Since $d\Gamma \sim O[r]$, the integral in that equation does not vanish, so

$$c_{IJ} = \lim_{r\to 0}\int_{\Gamma_r} p^*_{IJ}(\boldsymbol{\xi},\mathbf{x})\,d\Gamma \tag{3.8}$$

which is the so-called free term, which is related with the domain geometry.

The second term in (3.5) becomes, after taking limits,

$$\lim_{r\to 0}\int_{\Gamma-\Gamma_r} p^*_{IJ}(\boldsymbol{\xi},\mathbf{x})u_I(\mathbf{x})\,d\Gamma = \fint_{\Gamma} p^*_{IJ}(\boldsymbol{\xi},\mathbf{x})u_I(\mathbf{x})\,d\Gamma \tag{3.9}$$

Where $\fint$ indicates *Cauchy's principal value* integration.

If the limit $r \to 0$ is now considered in (3.6), the first term becomes

$$\lim_{r\to 0}\int_{\Gamma_r} u^*_{IJ}(\boldsymbol{\xi},\mathbf{x})p_I(\mathbf{x})\,d\Gamma = p_I(\xi)\lim_{r\to 0}\int_{\Gamma_r} u^*_{IJ}(\boldsymbol{\xi},\mathbf{x})\,d\Gamma = 0 \tag{3.10}$$

That integral vanishes when the distance between the observation and collocation points tends to zero, because the displacement fields present a $O[ln(r)]$ asymptotic behavior, while $d\Gamma$ has a $O[r]$ behavior.

The second term in (3.6) becomes

$$\lim_{r\to 0}\int_{\Gamma-\Gamma_r} u^*_{IJ}(\boldsymbol{\xi},\mathbf{x})p_I(\mathbf{x})\,d\Gamma = \fint_{\Gamma} u^*_{IJ}(\boldsymbol{\xi},\mathbf{x})p_I(\mathbf{x})\,d\Gamma \tag{3.11}$$

Thus, equation (3.4) may be rewritten for every point in the boundary as

$$c_{IJ}u_J(\xi) + \fint_{\Gamma} p^*_{IJ}(\boldsymbol{\xi},\mathbf{x})u_I(\mathbf{x})\,d\Gamma = \fint_{\Gamma} u^*_{IJ}(\boldsymbol{\xi},\mathbf{x})p_I(\mathbf{x})\,d\Gamma \tag{3.12}$$

The equation (3.12) is the so-called displacement boundary integral equation which, for magnetoelectroelastic solids, is defined in an extended way.

If the boundary Γ is discretized in E elements

$$\Gamma = \sum_{e=1}^{e=E}\Gamma_e \tag{3.13}$$

and in those elements, the continuous functions $u_J(x)$ and $p_J(x)$ are defined by interpolation of the values in a certain number n of nodes, by the use of known interpolation functions $\phi_q(x)$. Then

$$u_I(x) = \sum_{q=1}^{q=n} \phi_q(x) u_I(x^q) = \sum_{q=1}^{q=n} \phi_q(x) u_I^q \tag{3.14}$$

$$p_I(x) = \sum_{q=1}^{q=n} \phi_q(x) p_I(x^q) = \sum_{q=1}^{q=n} \phi_q(x) p_I^q \tag{3.15}$$

and equation (3.12) can be rewritten as follows

$$\begin{aligned} c_{IJ} u_J(\xi) + \sum_{e=1}^{e=E} \sum_{q=1}^{q=n} \int_{\Gamma_e} p_{IJ}^*(\boldsymbol{\xi}, \mathbf{x}) \phi_q(x) u_I^q \, d\Gamma \; = \\ = \sum_{e=1}^{e=E} \sum_{q=1}^{q=n} \int_{\Gamma_e} u_{IJ}^*(\boldsymbol{\xi}, \mathbf{x}) \phi_q(x) p_I^q \, d\Gamma \end{aligned} \tag{3.16}$$

So a problem in which the unknown variables are continuous functions has been transformed into one in which they are the values of those functions in $N = n \cdot E$ nodal points.

If that equation is obtained for all the points established in the boundary, an algebraic equation as the following is obtained

$$c_{IJ} u_J + \widehat{H}_{IJ} u_J = G_{IJ} p_J \Longrightarrow H_{IJ} u_J = G_{IJ} p_J \tag{3.17}$$

If tractions and displacements boundary conditions are now applied and (3.17) is rearranged in a proper way, a system of equations in which the known and unknown variables are separated is obtained

$$\mathbf{A}\mathbf{x} = \mathbf{b} \tag{3.18}$$

Finally, from the field variables in the boundary, the displacement values in any point of the domain can be obtained by the equation (3.4) and the tractions, in general, by the use of the kinematic relations. However, as it will be exposed in section 3.3, in the hypersingular formulation of the BEM, tractions are obtained directly by the application of a different boundary integral equation.

The extension of the previous formulation to the time-harmonic case can be done inmediately by means of the elastodynamic reciprocity theorem by Graffi (1946). The expression of this theorem is analogous to (3.1) but including the dependency of the variables with the frequency. The resulting time-harmonic boundary integral equation, obtained after a similar procedure as the one followed in the static case, is then

$$c_{IJ}u_J(\boldsymbol{\xi},\omega) + \int_\Gamma p^*_{IJ}(\boldsymbol{\xi},\mathbf{x},\omega)u_I(\mathbf{x},\omega)\,d\Gamma = \int_\Gamma u^*_{IJ}(\boldsymbol{\xi},\mathbf{x},\omega)p_I(\mathbf{x},\omega)\,d\Gamma \quad (3.19)$$

where ω denotes the considered frequency, while the expression for a time-harmonic point load is $\rho f^*_I = \delta(\mathbf{x}-\xi)\delta_{IJ}e^{-i\omega t}$.

In relation to the transient analysis, the boundary integral equation takes the form (for further details, see Dominguez, 1993)

$$c_{IJ}u_J(\xi,t) + \int_\Gamma p^*_{IJ}(\boldsymbol{\xi},\mathbf{x},t) * u_I(\mathbf{x},t)\,d\Gamma = \int_\Gamma u^*_{IJ}(\boldsymbol{\xi},\mathbf{x},t) * p_I(\mathbf{x},t)\,d\Gamma \quad (3.20)$$

in which the time integration is carried out by the Riemann convolution product (denoted by $*$), which can be defined as

$$f(t) = g(t) * h(t) = \int_0^t g(t-\tau)h(t)\,d\tau \quad (3.21)$$

Unlike the conventional time-domain BEM (see for details works by Tan et al., 2005a,b; Zhang, 2002b), the time-domain BEM formulation presented in this work applies the Laplace-domain instead of the time-domain elastodynamic fundamental solutions. This is specially advantageous in cases where time-domain dynamic fundamental solutions are not available but their Laplace-transforms can be obtained.

The time integration has been carried out by means of Lubich's quadrature formula (1988a; 1988b), which establishes that, if a time interval is divided in K subintervals of the same length Δt, convolution product of two functions can be approximated by the following quadrature

$$f(k\cdot\Delta t)=\int_0^{k\cdot\Delta t} g(t-\tau)h(t)\,d\tau \cong \sum_{j=0}^{k}\omega_{k-j}(\Delta t)h(j\cdot\Delta t) \tag{3.22}$$

where the weights are related with the Laplace transform of the $g(t)$ function, $\overline{g}(\cdot)$, as

$$\omega_k(\Delta t)=\frac{r^{-k}}{K}=\sum_{m=0}^{K-1}\overline{g}\left(\frac{\delta(\zeta_m)}{\Delta t}\right)e^{-2\pi i n m/K}, \qquad k=0,1,2,...,K \tag{3.23}$$

being i the imaginary unit number and

$$\delta(\varsigma_m)=\sum_{j=1}^{2}(1-\zeta_m)^j/2 \;\;;\;\; \zeta_m=r\cdot e^{-2\pi i k m/K} \;\;;\;\; r=\epsilon^{1/(2K)} \tag{3.24}$$

where ϵ is the numerical error in computing the Laplace transform $\overline{g}(\cdot)$, which is of the order $O(\sqrt{\epsilon})$. Previous works (see, e.g. García-Sánchez and Zhang, 2007b) reveal that when ϵ is between 10^{-6} and 10^{-12}, changes in the results are negligible.

3.3 Hypersingular BEM formulation for fracture mechanics problem in magnetoelectroelastic solids

3.3.1 Introduction

Geometrical modelization of a crack is carried out by two coincident surfaces. This fact implies numerical troubles when trying to solve fracture mechanics problems with the BEM: since two equal equations are obtained for both crack surfaces, a degeneration of the system of equations is provoked. To solve that issue, there exist three possibilities.

The first one is the use of *specific fundamental solutions* over domains which include the crack, as proposed by Snyder and Cruse (1975) for anisotropic plates. This method present a big inconvenient since it needs tailored Green's functions for each problem crack geometry.

Another solution is the so-called *subregions method*, which consists in the introduction of a fictitious surface which separate the original domain in two subdomains so that each crack face belongs to one of them. Thus, different equations for each crack surface are obtained, although now is necessary to apply equilibrium and compatibility equations on the interface which separates both domains. There exist many works in which this technique has been applied for anisotropic and piezoelectric materials, such as those by Ishikawa (1990) and Daví and Milazzo (2001).

Another possibility, the one adopted in this work, is the use of the *hypersingular (dual) formulation of the BEM*. It consists in the application of the (extended) displacement boundary integral equation (EDBIE), presented in the previous section, to the external boundary and one of the crack faces, and another boundary integral equation to the other crack face. This new integral equation is obtained by derivation of the EDBIE respect to the

collocation point, as done by Iokamidis (1983) and Hong and Chen (1988), being the main problem of this method the numerical evaluation of the singular and hypersingular integrals which appear when the collocation point belongs to the element where the integration is carried out.

Portela et al. (1992) and Sollero and Aliabadi (1995) applied this method to bidimensional isotropic and anisotropic fracture mechanics problem, but the way they solve the integrals requires the use of straight elements. This restriction can be avoided by the use of the more general treatment of the hypersingular integrals introduced for isotropic behavior by Sáez et al. (1995), and later generalized by García-Sánchez et al. for anisotropic and piezoelectric solids (2004; 2005a).

3.3.2 Dual BEM for fracture mechanics problems

In this section the hypersingular BEM formulation will be first introduced for static fracture mechanics problems, being this formulation extended later on to the frequency and time domains, in sections 3.3.3 and 3.3.4, respectively.

Degeneration of the system of equations. Traction boundary integral equation

Let Ω be a 2-D magnetoelectroelastic cracked domain with boundary Γ as the one shown in figure 3.2, so that $\Gamma = \Gamma_B \cup \Gamma_{crack}$, where Γ_B is the external non-cracked boundary and $\Gamma_{crack} = \Gamma_+ \cup \Gamma_-$ are the two geometrically coincident crack surfaces.

As it has been said, if the EDBIE is applied to all the boundaries, then a degenerated system of equation will be obtained, since both crack faces are geometrically coincident. The dual or hypersingular formulation of

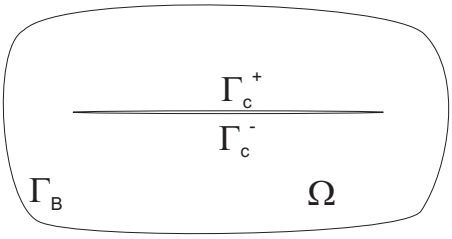

Figure 3.2: Boundaries in a cracked domain

the BEM considers two boundary integral representations to overcome that problem: the extended displacement (EDBIE) and the so-called extended traction (ETBIE) boundary integral equation. To obtain this new equation, we start whith the EDBIE for an internal point (3.4) which will be derivated with respect to the collocation point. After applying the relations given by equations (2.2) and the constitutive equations, equations (2.1), the following equation is obtained:

$$C_{sJKr}\frac{\partial u_K(\boldsymbol{\xi})}{\partial \xi_r} + C_{sJKr}\int_\Gamma \frac{\partial p^*_{KJ}(\boldsymbol{\xi},\mathbf{x})}{\partial \xi_r} u_I(\mathbf{x})\, d\Gamma \; = \\ = C_{sJKr}\int_\Gamma \frac{\partial u^*_{KI}(\boldsymbol{\xi},\mathbf{x})}{\partial \xi_r} p_I(\mathbf{x})\, d\Gamma \tag{3.25}$$

Now, since the extended stress tensor in the collocation point is $\sigma_{sK}(\xi) = C_{sIKr}u_{I,r}$, by multiplying the previous equation by the unit normal on that point ($\mathbf{N}(\xi)$), the extended tractions on that point are obtained

$$p_J(\boldsymbol{\xi}) + \int_\Gamma s^*_{IJ}(\boldsymbol{\xi},\mathbf{x}) u_I(\mathbf{x})\, d\Gamma \; = \int_\Gamma d^*_{IJ}(\boldsymbol{\xi},\mathbf{x}) p_I(\mathbf{x})\, d\Gamma \tag{3.26}$$

where

$$d^*_{IK}(\boldsymbol{\xi},\mathbf{x}) = N_s(\boldsymbol{\xi}) C_{sIJr} u^*_{KJ,r}(\boldsymbol{\xi},\mathbf{x}) \tag{3.27}$$

$$s^*_{IK}(\boldsymbol{\xi}, \mathbf{x}) = N_s(\boldsymbol{\xi}) C_{sIJr} p^*_{KJ,r}(\boldsymbol{\xi}, \mathbf{x}) \tag{3.28}$$

Now, following for equation (3.26) a similar procedure to the one carried out for the EDBIE, the extended traction boundary integral equation (ETBIE) is obtained as

$$c_{IJ} p_J(\boldsymbol{\xi}) + \oint\!\!\!\!\!\!= \int_\Gamma s^*_{IJ}(\boldsymbol{\xi}, \mathbf{x}) u_I(\mathbf{x})\, d\Gamma = \int_\Gamma d^*_{IJ}(\boldsymbol{\xi}, \mathbf{x}) p_I(\mathbf{x})\, d\Gamma \tag{3.29}$$

where $\oint\!\!\!\!\!\!=$ indicates *Hadamard finite part* integral.

The hypersingular formulation of the BEM consist on the application of the EDBIE to the external boundary and one of the crack faces and the application of the ETBIE on the other crack surface.

Boundary integral equations in terms of the extended crack opening displacements

In this section it will be demonstrated that is possible to reduce de dual BEM formulation in fracture mechanic problems to the application of the EDBIE to the external boundaries and the ETBIE to only one of the crack faces.

Let us rewrite equations (3.12) and (3.29) to keep the order in the exposition, considering that $\Gamma = \Gamma_B + \Gamma_c^+ + \Gamma_c^-$

EDBIE if $\xi \in \Gamma_B, \Gamma_c^-$

$$c_{IJ} u_J(\boldsymbol{\xi}) + \int_\Gamma p^*_{IJ}(\boldsymbol{\xi}, \mathbf{x}) u_I(\mathbf{x})\, d\Gamma = \int_\Gamma u^*_{IJ}(\boldsymbol{\xi}, \mathbf{x}) p_I(\mathbf{x})\, d\Gamma \tag{3.30}$$

ETBIE if $\xi \in \Gamma_c^+$

$$p_J(\boldsymbol{\xi}) + \oint\!\!\!\!\!\!= \int_\Gamma s^*_{IJ}(\boldsymbol{\xi}, \mathbf{x}) u_I(\mathbf{x})\, d\Gamma = \int_\Gamma d^*_{IJ}(\boldsymbol{\xi}, \mathbf{x}) p_I(\mathbf{x})\, d\Gamma \tag{3.31}$$

Considering now that

$$\oint_{\Gamma_c^-} p^*_{IJ}(\boldsymbol{\xi},\mathbf{x})u_I(\mathbf{x}^-)\,d\Gamma = -\oint_{\Gamma_c^+} p^*_{IJ}(\boldsymbol{\xi},\mathbf{x})u_I(\mathbf{x}^+)\,d\Gamma \tag{3.32a}$$

$$\oint_{\Gamma_c^-} u^*_{IJ}(\boldsymbol{\xi},\mathbf{x})p_I(\mathbf{x}^-)\,d\Gamma = \oint_{\Gamma_c^+} u^*_{IJ}(\boldsymbol{\xi},\mathbf{x})p_I(\mathbf{x}^+)\,d\Gamma \tag{3.32b}$$

$$\oint_{\Gamma_c^-} s^*_{IJ}(\boldsymbol{\xi},\mathbf{x})u_I(\mathbf{x}^-)\,d\Gamma = -\oint_{\Gamma_c^+} s^*_{IJ}(\boldsymbol{\xi},\mathbf{x})u_I(\mathbf{x}^+)\,d\Gamma \tag{3.32c}$$

$$\oint_{\Gamma_c^-} d^*_{IJ}(\boldsymbol{\xi},\mathbf{x})p_I(\mathbf{x}^-)\,d\Gamma = \oint_{\Gamma_c^+} d^*_{IJ}(\boldsymbol{\xi},\mathbf{x})p_I(\mathbf{x}^+)\,d\Gamma \tag{3.32d}$$

Calling now $\Delta u_I(x)$ and $\Delta p_I(x)$, respectively, to the jump in the generalized displacement and the sum of the extended tractions on the crack surfaces (according to definition in equation 2.7)

$$\begin{aligned}\Delta u_I(\mathbf{x}) = (u_1(\mathbf{x}^+) - u_1(\mathbf{x}^-), u_2(\mathbf{x}^+) - u_2(\mathbf{x}^-), \dots \\ \dots, \phi(\mathbf{x}^+) - \phi(\mathbf{x}^-), \varphi(\mathbf{x}^+) - \varphi(\mathbf{x}^-))\end{aligned} \tag{3.33}$$

$$\begin{aligned}\Delta p_I(\mathbf{x}) = (p_1(\mathbf{x}^+) + p_1(\mathbf{x}^-), p_2(\mathbf{x}^+) + p_2(\mathbf{x}^-), \dots \\ \dots D_n(\mathbf{x}^+) + D_n(\mathbf{x}^-), B_n(\mathbf{x}^+) + B_n(\mathbf{x}^-))\end{aligned} \tag{3.34}$$

then the boundary integral equations can be rewritten, respectively, as

$$\begin{aligned}c_{IJ}u_J(\boldsymbol{\xi}) + \oint_{\Gamma_B} p^*_{IJ}(\boldsymbol{\xi},\mathbf{x})u_I(\mathbf{x})\,d\Gamma + \int_{\Gamma_c^+} p^*_{IJ}(\boldsymbol{\xi},\mathbf{x})\Delta u_I(\mathbf{x})\,d\Gamma = \\ = \oint_{\Gamma_B} u^*_{IJ}(\boldsymbol{\xi},\mathbf{x})p_I(\mathbf{x})\,d\Gamma + \int_{\Gamma_c^+} u^*_{IJ}(\boldsymbol{\xi},\mathbf{x})\Delta p_I(\mathbf{x})\,d\Gamma\end{aligned} \tag{3.35}$$

$$p_J(\boldsymbol{\xi}) + \int_{\Gamma_B} s^*_{IJ}(\boldsymbol{\xi},\mathbf{x}) u_I(\mathbf{x})\, d\Gamma + \Xint= \int_{\Gamma_c^+} s^*_{IJ}(\boldsymbol{\xi},\mathbf{x}) \Delta u_I(\mathbf{x})\, d\Gamma =$$
$$= \int_{\Gamma_B} d^*_{IJ}(\boldsymbol{\xi},\mathbf{x}) p_I(\mathbf{x})\, d\Gamma + \Xint= \int_{\Gamma_c^+} d^*_{IJ}(\boldsymbol{\xi},\mathbf{x}) \Delta p_I(\mathbf{x})\, d\Gamma \tag{3.36}$$

In this work all the cases studied present impermeable and self-equilibrated cracks, what implies that, on the crack, $\Delta p_J(\mathbf{x}) = 0$. In this case, the dual BEM formulation can be expressed as

If $\boldsymbol{\xi} \in \Gamma_B$

$$c_{IJ} u_J(\boldsymbol{\xi}) + \Xint= \int_{\Gamma_B} p^*_{IJ}(\boldsymbol{\xi},\mathbf{x}) u_I(\mathbf{x})\, d\Gamma + \int_{\Gamma_c^+} p^*_{IJ}(\boldsymbol{\xi},\mathbf{x}) \Delta u_I(\mathbf{x})\, d\Gamma =$$
$$= \Xint= \int_{\Gamma_B} u^*_{IJ}(\boldsymbol{\xi},\mathbf{x}) p_I(\mathbf{x})\, d\Gamma \tag{3.37}$$

If $\boldsymbol{\xi} \in \Gamma_c^+$

$$p_J(\boldsymbol{\xi}) + \int_{\Gamma_B} s^*_{IJ}(\boldsymbol{\xi},\mathbf{x}) u_I(\mathbf{x})\, d\Gamma + \Xint= \int_{\Gamma_c^+} s^*_{IJ}(\boldsymbol{\xi},\mathbf{x}) \Delta u_I(\mathbf{x})\, d\Gamma =$$
$$= \Xint= \int_{\Gamma_B} d^*_{IJ}(\boldsymbol{\xi},\mathbf{x}) p_I(\mathbf{x})\, d\Gamma \tag{3.38}$$

3.3.3 Extension to the time-harmonic domain

The extension of the static extended boundary integral equations (3.37-3.38) to the frequency domain is inmediate by means of the elastodynamic reciprocity theorem by Graffi (1946), including the dependency of the variables with the frequency. Thus, if impermeable cracks are considered, extended BIE can be expressed as

If $\boldsymbol{\xi} \in \Gamma_B$

$$c_{IJ}u_J(\boldsymbol{\xi},\omega) + \oint_{\Gamma_B} p^*_{IJ}(\boldsymbol{\xi},\mathbf{x},\omega)u_I(\mathbf{x},\omega)\,d\Gamma + \int_{\Gamma_c^+} p^*_{IJ}(\boldsymbol{\xi},\mathbf{x},\omega)\Delta u_I(\mathbf{x},\omega)\,d\Gamma =$$
$$= \oint_{\Gamma_B} u^*_{IJ}(\boldsymbol{\xi},\mathbf{x},\omega)p_I(\mathbf{x},\omega)\,d\Gamma \tag{3.39}$$

If $\boldsymbol{\xi} \in \Gamma_c^+$

$$p_J(\boldsymbol{\xi},\omega) + \int_{\Gamma_B} s^*_{IJ}(\boldsymbol{\xi},\mathbf{x},\omega)u_I(\mathbf{x},\omega)\,d\Gamma + \oint_{\Gamma_c^+} s^*_{IJ}(\boldsymbol{\xi},\mathbf{x},\omega)\Delta u_I(\mathbf{x},\omega)\,d\Gamma =$$
$$= \oint_{\Gamma_B} d^*_{IJ}(\boldsymbol{\xi},\mathbf{x},\omega)p_I(\mathbf{x},\omega)\,d\Gamma \tag{3.40}$$

3.3.4 Extension to the time domain. Time-stepping scheme

Boundary integral equations in the time domain take the form

If $\boldsymbol{\xi} \in \Gamma_B$

$$c_{IJ}u_J(\boldsymbol{\xi},t) + \oint_{\Gamma_B} p^*_{IJ}(\boldsymbol{\xi},\mathbf{x},t) * u_I(\mathbf{x},t)\,d\Gamma + \int_{\Gamma_c^+} p^*_{IJ}(\boldsymbol{\xi},\mathbf{x},t) * \Delta u_I(\mathbf{x},t)\,d\Gamma =$$
$$= \oint_{\Gamma_B} u^*_{IJ}(\boldsymbol{\xi},\mathbf{x},t) * p_I(\mathbf{x},t)\,d\Gamma \tag{3.41}$$

If $\boldsymbol{\xi} \in \Gamma_c^+$

$$p_J(\boldsymbol{\xi},t) + \int_{\Gamma_B} s^*_{IJ}(\boldsymbol{\xi},\mathbf{x},t) * u_I(\mathbf{x},t)\,d\Gamma + \oint_{\Gamma_c^+} s^*_{IJ}(\boldsymbol{\xi},\mathbf{x},t) * \Delta u_I(\mathbf{x},t)\,d\Gamma =$$
$$= \oint_{\Gamma_B} d^*_{IJ}(\boldsymbol{\xi},\mathbf{x},t) * p_I(\mathbf{x},t)\,d\Gamma \tag{3.42}$$

The Riemann convolution product (denoted by $*$), is carried out by means of Lubich's quadratures as defined by equations (3.22-3.24), leading, after

spatial discretization to the Laplace-domain system matrices, $\bar{\boldsymbol{G}}(s_m)$ and $\bar{\boldsymbol{H}}(s_m)$, which can be computed by

$$\bar{\boldsymbol{G}}(s_m) = \begin{cases} \sum_{e=1}^{E} \int_{\Gamma_e} u^*_{IJ}(\boldsymbol{\xi}, \boldsymbol{x}, s_m)\, \phi_q(\boldsymbol{x})\, d\Gamma, & \text{for EDBIE,} \\ \sum_{e=1}^{E} \int_{\Gamma_e} d^*_{IJ}(\boldsymbol{\xi}, \boldsymbol{x}, s_m)\, \phi_q(\boldsymbol{x})\, d\Gamma, & \text{for ETBIE,} \end{cases} \tag{3.43}$$

$$\bar{\boldsymbol{H}}(s_m) = \begin{cases} \sum_{e=1}^{E} \int_{\Gamma_e} p^*_{IJ}(\boldsymbol{\xi}, \boldsymbol{x}, s_m)\, \phi_q(\boldsymbol{x})\, d\Gamma, & \text{for EDBIE,} \\ \sum_{e=1}^{E} \int_{\Gamma_e} s^*_{IJ}(\boldsymbol{\xi}, \boldsymbol{x}, s_m)\, \phi_q(\boldsymbol{x})\, d\Gamma, & \text{for ETBIE.} \end{cases} \tag{3.44}$$

where $s_m = \delta(\zeta_m)/\Delta t$ is the Laplace parameter, and u^*_{IJ}, p^*_{IJ}, d^*_{IJ} and s^*_{IJ} are the terms of the fundamental solution, as described in section 3.6.

Taking into account the approximation of the Riemann convolution integral redefined in equations (3.22-3.24), the system matrix at the $(k-j)^{th}$ time-step can be obtained by

$$\boldsymbol{G}^{k-j} = \frac{r^{-(k-j)}}{K} \sum_{m=0}^{K-1} \bar{\boldsymbol{G}}(s_m)\, e^{-2\pi i (k-j) m/K}, \tag{3.45}$$

$$\boldsymbol{H}^{k-j} = \frac{r^{-(k-j)}}{K} \sum_{m=0}^{K-1} \bar{\boldsymbol{H}}(s_m)\, e^{-2\pi i (k-j) m/K}, \tag{3.46}$$

And now, once that both spatial and time discretizations have been performed, the following time scheme is obtained

$$\sum_{j=0}^{k} \boldsymbol{H}^{k-j} \cdot \boldsymbol{u}^j = \sum_{j=0}^{k} \boldsymbol{G}^{k-j} \cdot \boldsymbol{p}^j, \qquad k = 0, 1, 2, ..., K \tag{3.47}$$

where $\boldsymbol{G}^{k-j}$ and $\boldsymbol{H}^{k-j}$ are the time-domain system matrices at the $(k-j)^{th}$ time-step, being k the total number of time-steps considered, $\boldsymbol{u}^j$ is the

vector containing the discrete boundary displacements and the extended crack opening displacements (ECOD), and $\boldsymbol{p}^j$ is the vector containing the discrete boundary tractions.

By considering now the boundary conditions, equation (3.47) can be rearranged as

$$\sum_{j=0}^{k} \boldsymbol{A}^{k-j} \cdot \boldsymbol{x}^j = \boldsymbol{y}^j \,, \tag{3.48}$$

where $\boldsymbol{A}^{k-j}$ is the rearranged system matrix, $\boldsymbol{x}^j$ is the vector containing the unknown boundary quantities, and $\boldsymbol{y}^j$ is the vector containing the prescribed or known boundary quantities. If zero initial conditions ($u_I(\mathbf{x},t) = \dot{u}_I(\mathbf{x},t) = 0$ for $t \leq 0$) are considered, equation (3.48) leads to the following explicit time-stepping scheme, as proposed by Zhang (2000, 2002a, 2005)

$$\boldsymbol{x}^k = \left(\boldsymbol{A}^0\right)^{-1} \cdot \left(\boldsymbol{y}^k - \sum_{j=1}^{k-1} \boldsymbol{A}^{k-j} \cdot \boldsymbol{x}^j \right) \tag{3.49}$$

for computing the unknown ECOD at the n^{th} time-step. In equation (3.49), $\left(\boldsymbol{A}^0\right)^{-1}$ is the inverse of the system matrix $\boldsymbol{A}^0$ at the time-step $n = 0$.

3.3.5 Meshing strategy

For the discretization of the geometry and field variables, quadratic elements have been used.

Numerical evaluation of the ETBIE requires C^1 continuity of the displacement to ensure the continuity of its derivatives and, thus, the continuity of tractions after the derivation on the node. To fulfill this requirement, discontinuous quadratic elements with the two extreme collocation nodes

shifted towards the center of the element are used to mesh the crack, as it has been done in previous works (García-Sánchez et al., 2004), following the formulation developed by Sáez et al. (1995). According to this, two different elements have been considered in this work: continuous and discontinuous elements.

In *continuous elements* the same points (the extremes and the middle point of the element) are used to define the geometry and field variables. Shape functions for these elements (*geometric shape functions*) are the following ones

$$\phi_{1G}(\zeta) = \frac{1}{2}\zeta(\zeta - 1) \;\; ; \;\; \phi_{2G}(\zeta) = (1 - \zeta^2) \;\; ; \;\; \phi_{3G}(\zeta) = \frac{1}{2}\zeta(\zeta + 1) \quad (3.50)$$

where ζ is the natural coordinate, which vary between -1 and +1.

In *discontinuous elements*, for the geometric discretization, the shape functions already seen (equation 3.50) are used, while for the field variables new shape functions will be used. In them, as it has been said, the extreme collocation points are moved towards the center. These functions, the so-called *calculus shape functions* will be equal to one in the points $\zeta = \zeta_1, 0, \zeta_2$ instead of in $\zeta = -1, 0, 1$. The expressions for them are

$$\begin{aligned} &\phi_1(\zeta) = \frac{\zeta(\zeta - \zeta_2)}{\zeta_1(\zeta_1 - \zeta_2)} \;\; ; \;\; \phi_2(\zeta) = \frac{(\zeta - \zeta_1)(\zeta - \zeta_2)}{\zeta_1\zeta_2} \;\; ; \\ &\phi_3(\zeta) = \frac{\zeta(\zeta - \zeta_1)}{\zeta_2(\zeta_2 - \zeta_1)} \end{aligned} \quad (3.51)$$

Both *geometric* and *calculus shape functions* are represented in figure 3.3. In this work values of $\zeta_1 = -3/4$ and $\zeta_2 = 3/4$ have been taken, as it was done by Sáez et al. (1995).

Finally, in boundaries which are intersected by a crack, a discontinuous element will also be used, but only the node on the extreme intersected is

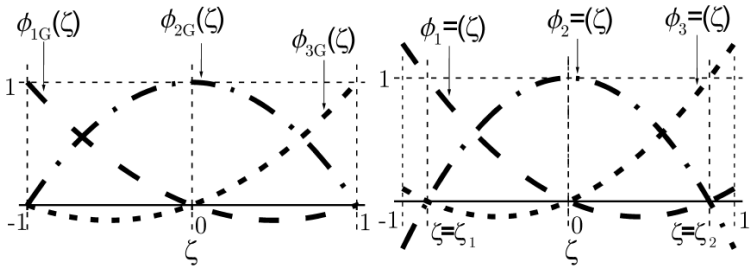

Figure 3.3: Geometric (left) and calculus (right) shape functions

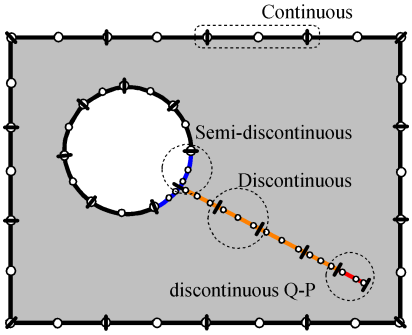

Figure 3.4: Elements used in the domain discretization

shifted towards the center. In figure 3.4 the disposition of the elements used in the work, depending on the boundary which they belong is summarized. Note that another element, the so-called *discontinuous quarter point element* appears in it. This element, which is used to modelize properly the asymptotic behavior of the field variables around the crack tip, is studied in detail in section 3.7.

3.4 Green's functions and numerical evaluation of the integrals. Static case

3.4.1 Fundamental solutions

Fundamental solution corresponding to the response of a homogeneous bidimensional magnetoelectroelastic solid, due to the application of an unit static extended point force is available in the literature (see e.g. works by Liu et al., 2001 and Jiang and Pan, 2004). That solution is obtained by means of the generalized Stroh's formalism (1958), following a similar procedure to the one developed by Barnett and Lothe (1975) for piezoelectric materials. Consequently, the expressions of the Green's functions present big similarities with those previously developed for anisotropic and piezoelectric materials and used in works by García-Sánchez et al. (2004; 2005; 2005a).

Thus, extended displacement in the observation point $\mathbf{x} = (x_1, x_2)$, in the J-direction when a (extended) point load in the collocation point $\boldsymbol{\xi} = (\xi_1, \xi_2)$ is applied in the I-direction, can be expressed as

$$u^*_{IJ}(z^x_M, z^\xi_M) = -\frac{1}{\pi}\mathrm{Re}(A_{JM}Q_{MI}\ln(z^x_M - z^\xi_M)) \tag{3.52}$$

By the application of the kinematic relations and the behavior law, one can obtain the expressions for the extended tractions Green's functions

$$p^*_{IJ}(z^x_M, z^\xi_M) = \frac{1}{\pi}\mathrm{Re}\left(B_{JM}Q_{MI}\frac{\mu_M n_1 - n_2}{z^x_M - z^\xi_M}\right) \tag{3.53}$$

where $\mathbf{n}$ is the unit external normal at the observation point. In both equations (3.52-3.53), Re stands for the real part, the summation rule over repeated indices applies, and z_K and z^0_K are the transformation into the complex plane of the physical coordinates of the observation and collocation

points, by the use of the following transformation:

$$z_K^x = x_1 + \mu_K x_2 \tag{3.54}$$

$$z_K^\xi = \xi_1 + \mu_K \xi_2 \tag{3.55}$$

being μ_K the roots of the characteristic equation of the material, defined by (2.45), with positive imaginary part. Let us remark that those roots can also be obtained as well as the columns of the matrices $\mathbf{A}$ and $\mathbf{B}$, by solving the eigenvalues problem defined in (2.23).

Moreover, the matrix $\mathbf{Q}$ can be calculated as

$$\mathbf{Q} = \mathbf{A}^{-1}\left(\mathbf{M}^{-1} + \overline{\mathbf{M}}^{-1}\right)^{-1} \quad ; \quad \mathbf{M} = i\mathbf{A}\mathbf{B}^{-1} \tag{3.56}$$

The derivatives of the fundamental solution displacements and tractions needed to compute the kernels s_{IJ}^* and d_{IJ}^* in the ETBIE (3.38) are then obtained as

$$u_{IJ,k}^*(\mathbf{x},\boldsymbol{\xi}) = \frac{\partial u_{IJ}^*(\mathbf{x},\boldsymbol{\xi})}{\partial \xi_k} = \frac{1}{\pi}\,\mathrm{Re}\left[A_{IM}Q_{MJ}\frac{\delta_{k1}+\mu_M\delta_{k2}}{z_M^x - z_M^\xi}\right] \tag{3.57}$$

$$\begin{aligned} p_{IJ,k}^*(\mathbf{x},\boldsymbol{\xi}) &= \frac{\partial p_{IJ}^*(\mathbf{x},\boldsymbol{\xi})}{\partial \xi_k} = \\ &= \frac{1}{\pi}\,\mathrm{Re}\left[B_{IM}Q_{MJ}\frac{\mu_M n_1 - n_2}{(z_M^x - z_M^\xi)^2}(\delta_{k1}+\mu_M\delta_{k2})\right] \end{aligned} \tag{3.58}$$

3.4.2 Numerical evaluation of singular and hypersingular integrals

As it could be seen in section 3.4.1, all the terms of the fundamental solution present functional dependencies to the distances in the complex plane

between the collocation and the observation point, $\left(z_M^x - z_M^\xi\right)$. That dependency in u_{IJ}^* has the form $\ln\left(z_M^x - z_M^\xi\right)$, while in the terms p_{IJ}^* and d_{IJ}^*, the dependency present a $1/\left(z_M^x - z_M^\xi\right)$ form and, finally, the kernels s_{IJ}^* show a $1/\left(z_M^x - z_M^\xi\right)^2$ dependency.

In all those cases, when the observation point approaches the collocation one, some numerical issues arise. In particular, logarithmically singular, strongly singular and hypersingular integrals, respectively, must be evaluated, while if the integration is carried out in elements which do not contain the collocation point, standard Gauss quadratures are used.

Weakly singular integrals

These are the integrals which contain the displacement Green's function:

$$\oint_{\Gamma_B} u_{IJ}^*(\boldsymbol{\xi}, \mathbf{x}) p_I(\mathbf{x})\, d\Gamma \tag{3.59}$$

Introducing now in that equation the expression of the Green's function, and approximating the tractions by the nodal values and shape functions, equation (3.59) leads to integrals of the form

$$I_w = \oint_{\Gamma_e} \ln(z_K^x - z_K^\xi)\phi\, d\Gamma \tag{3.60}$$

where, for the sake of clarity, the terms that only depend on the material properties have been removed from equation (3.60). The kernels present a $0\left[\ln(z_M^x - z_M^\xi)\right]$ singularity when the the observation and collocation point approach, i.e. $\mathbf{x} \to \xi$. These kind of integrals are solved by the use of specific logarithmic quadratures when $\xi \in \Gamma_e$.

Strongly singular integrals

Strongly singular kernels present a $0\left[1/(z_M^x - z_M^\xi)\right]$ singularity when the integration is performed in the element where the collocation point belong to and are the following

$$\int\!\!\!\!\!\!\diagup_{\Gamma_B} p_{IJ}^*(\boldsymbol{\xi}, \mathbf{x}) u_I(\mathbf{x})\, d\Gamma \qquad ; \qquad \int\!\!\!\!\!\!\diagup_{\Gamma_c} d_{IJ}^*(\boldsymbol{\xi}, \mathbf{x}) \Delta p_I(\mathbf{x})\, d\Gamma \tag{3.61}$$

Let us remark that when impermeable crack boundary condition or self-equilibrated cracks are considered ($\Delta p_J = 0$), d_{IJ}^* kernels will never present a singular behavior. However, in order to complete the exposition of this work, the integration of these singular integrals is presented.

If the expressions of the Green's functions are introduced in (3.61), after the geometric discretizations and nodal approximations of the nodal variables, the integrals to be evaluated present the following form

$$I_{s1} = \int\!\!\!\!\!\!\diagup_{\Gamma_e} \frac{\mu_K n_1 - n_2}{z_K^x - z_K^\xi} \phi\, d\Gamma \tag{3.62}$$

$$I_{s2} = \int\!\!\!\!\!\!\diagup_{\Gamma_e} \frac{\mu_K N_1 - N_2}{z_K^x - z_K^\xi} \phi\, d\Gamma \tag{3.63}$$

where $\mathbf{n} = (n_1, n_2)$ and $\mathbf{N} = (N_1, N_2)$ are, respectively, the unit normal at the observation point and at the collocation point and, again, the terms which only depend on the material properties have been removed from those equations.

For solving numerically these integrals a change of variable is carried out, which transform every element in the boundary, Γ_e, to the complex plane. Thus, the new variable is the distance in the complex plane between both collocation and observation points:

$$\chi_K = z_K^x - z_K^\xi = (x_1 - \xi_1) + \mu_K (x_2 - \xi_2) \tag{3.64}$$

The jacobian of the transformation is

$$\frac{d\chi_K}{d\Gamma} = \frac{d\chi_K}{dx_1}\frac{dx_1}{d\Gamma} + \frac{d\chi_K}{dx_2}\frac{dx_2}{d\Gamma} \tag{3.65}$$

where

$$\frac{d\chi_K}{dx_1} = 1 \qquad ; \qquad \frac{d\chi_K}{dx_2} = \mu_K \tag{3.66}$$

$$\frac{dx_1}{d\Gamma} = \cos(\theta) = -n_2 \qquad ; \qquad \frac{dx_2}{d\Gamma} = \sin(\theta) = n_1 \tag{3.67}$$

As figure 3.5 illustrates, the substitution of (3.66) and (3.67) in the jacobian, leads to the following expression for it

$$\frac{d\chi_K}{d\Gamma} = \mu_K n_1 - n_2 \tag{3.68}$$

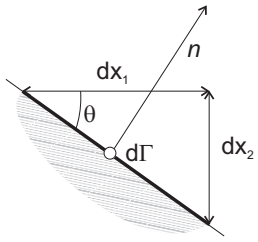

Figure 3.5: Differential element in the boundary

Numerical evaluation of I_{s1}

If the expression for the jacobian, equation (3.66) is introduced in (3.62), the strongly singular integral, I_{s1} may be rewritten as

$$I_{s1} = \int\!\!\!\!\!\!-_{\Gamma_e} \frac{\mu_K n_1 - n_2}{z_K^x - z_K^\xi} \phi \, d\Gamma = \int\!\!\!\!\!\!-_{\Gamma_e} \frac{1}{\chi_K} \phi \, d\chi_K \tag{3.69}$$

which could be easily decomposed into

$$I_{s1} = \int\!\!\!\!\!\!\diagup_{\Gamma_e} \frac{1}{\chi_K}\phi\, d\chi_K = \int\!\!\!\!\!\!\diagup_{\Gamma_e} \frac{1}{\chi_K}(\phi \pm 1)\, d\chi_K = \int_{\Gamma_e} \frac{1}{\chi_K}(\phi - 1)\, d\chi_K + \\ + \int\!\!\!\!\!\!\diagup_{\Gamma_e} \frac{1}{\chi_K}\, d\chi_K = I_{s1}^{(R)} + I_{s1}^{(S)} \tag{3.70}$$

$I_{s1}^{(R)}$ is a regular integral which can be determined by an ordinary Gauss quadratures scheme, while $I_{s1}^{(S)}$ is still singular, but with the following analytical solution

$$I_{s1}^{(S)} = \ln(\chi_K)|_{\Gamma_e} \tag{3.71}$$

Numerical evaluation of I_{s2}

When χ_K is introduced in (3.63), it yields to

$$I_{s2} = \int\!\!\!\!\!\!\diagup_{\Gamma_e} \frac{\mu_K N_1 - N_2}{\chi_K}\phi d\Gamma \tag{3.72}$$

To regularize that integral, $d\chi_K/d\Gamma$ is added and subtracted, leading to the following integral

$$I_{s2} = \int_{\Gamma_e} \frac{\mu_K N_1 - N_2 - (d\chi_K/d\Gamma)}{\chi_K}\phi d\Gamma + \int\!\!\!\!\!\!\diagup_{\Gamma_e} \frac{1}{\chi_K}\phi d\chi_K \tag{3.73}$$

where the first term is a regular integral and the second one is the already seen I_{s1} integral.

Hypersingular integrals

Hypersingular kernels present a $O\left[\frac{1}{(z_K^x - z_K^\xi)^2}\right]$ singularity when $\mathbf{x} \to \boldsymbol{\xi}$. These integrals are those which contain the term s_{IJ}^* in the TBIE

$$\oint\!\!\!\!\!\!= \int_{\Gamma_c} s^*_{IJ}(\boldsymbol{\xi}, \mathbf{x}) u_I(\mathbf{x})\, d\Gamma \tag{3.74}$$

After the discretization procedure, hypersingular integrals to be evaluated may be rewritten as

$$I_h = \oint\!\!\!\!\!\!= \int_{\Gamma_e} \frac{\mu_K n_1 - n_2}{(z^x_K - z^\xi_K)^2} \phi\, d\Gamma \tag{3.75}$$

And now, considering the change of variable proposed in the previous section, hypersingular integral can be expressed as a function of χ_K as follows

$$I_h = \oint\!\!\!\!\!\!= \int_{\Gamma_e} \frac{\mu_K n_1 - n_2}{(z^x_K - z^\xi_K)^2} \phi\, d\Gamma = \oint\!\!\!\!\!\!= \int_{\Gamma_e} \frac{1}{\chi^2_K} \phi\, d\chi_K \tag{3.76}$$

Let us now consider the Taylor series expansion of $\phi = f(\chi_K)$ around $\chi_K = 0$

$$\phi(\chi_K \approx 0) = \phi(\chi_K = 0) + \left.\frac{d\phi}{d\chi_K}\right|_{\chi_K=0} \chi_K + O[\chi^2_K] = \phi_0 + \phi'_0 \chi_K + O[\chi^2_K] \tag{3.77}$$

Adding and subtracting the two first terms of that expansion to ϕ in equation (3.76), the hypersingular integral can now be decomposed in the addition of three different integrals

$$I_h = \oint\!\!\!\!\!\!= \int_{\Gamma_e} \frac{1}{\chi^2_K} \phi\, d\chi_K = \oint\!\!\!\!\!\!= \int_{\Gamma_e} \frac{1}{\chi^2_K} (\phi \pm (\phi_0 + \phi'_0 \chi_K))\, d\chi_K =$$
$$\int_{\Gamma_e} \frac{\phi - (\phi_0 + \phi'_0 \chi_K)}{\chi^2_K}\, d\chi_K + \phi_0 \oint\!\!\!\!\!\!= \int_{\Gamma_e} \frac{1}{\chi^2_K} \phi\, d\chi_K + \phi'_0 \oint\!\!\!\!\!\!= \int_{\Gamma_e} \frac{1}{\chi_K} \phi\, d\chi_K \tag{3.78}$$

The first of those integrals is a regular one, the third one has been analyzed in the strongly singular integrals section while the second integral is still hypersingular but with an analytical solution

$$\phi_0 \oint_{\Gamma_e} \frac{1}{\chi_K^2} \phi \, d\chi_K = -\phi_0 \left. \frac{1}{\chi_K} \right|_{\Gamma_e} \tag{3.79}$$

This regularization procedure is simple and generic since it is not restricted to the use of straight elements on the crack. It presents another advantage against other methods which use specific quadratures for the numerical evaluation of hypersingular integrals (see e.g. Pan, 1997, 1999): a higher precision is obtained since the numerical integration is performed only over regular integrals.

3.5 Green's functions and numerical evaluation of the integrals. Time-harmonic case

3.5.1 Introduction

In this section, the Radon transform (Ludwig, 1966; Deans, 1983) is used to derive 3D and 2D time-harmonic dynamic fundamental solution for magnetoelectroelastic problems. This transform has been successfully applied by Wang and Achenbach (1994; 1995) to derive dynamic Green's functions for anisotropic and linear elastic solids, and byDenda et al. (2004) and Wang and Zhang (2005) to derive them for piezoelectric solids. The most interesting feature of Radon transform is that reduces 3D or 2D wave equations to 1D equations of the same kind, but easier to deal with. Once the 1D wave equations are solved, the solutions of the 3D and the 2D equations of motion will follow by a simple application of the inverse Radon transform

to yield the Green's functions in the form of surface integrals over a unit sphere.

Thus, as for anisotropic elastic and piezoelectric solids, the dynamic Green's functions are expressed as surface integrals over a unit sphere in the 3-D case and as line integrals over a unit circumference in the 2-D case. The dynamic Green's functions derived in this way can be further decomposed into a singular and a regular part. The singular part corresponds to the static magnetoelectroelastic Green's functions, whilst the regular part represents the contribution of the inertial terms in the equations of motion.

In this work, although Green's functions will be implemented only for 2-D problems, they will also be presented for the 3-D case, since the procedure to obtain them is analogous to the bidimensional one, except for the different expressions for the Radon transform (and their corresponding inverse Radon transform). After presenting them, the numerical solution of the integrals will be analyzed.

3.5.2 Fundamental solutions

3-D time-harmonic Green's functions

Time-harmonic Green's functions are defined as the response of an infinite homogeneous linear magnetoelectroelastic solid when a generalized time-harmonic point force is applied at the origin in the x_J-direction

$$F_M(\mathbf{x},t) = \delta_{JM}\delta(\mathbf{x})\delta e^{-i\omega t} \tag{3.80}$$

where ω is the angular frequency of excitation, $\delta(\mathbf{x})$ is the Dirac's delta function while δ_{JM} is the generalized Kronecker's delta function. The resulting generalized displacement field in the K-direction can be expressed,

in the steady state of harmonic motion, as

$$u_K(\mathbf{x},t) = u^*_{KM}(\mathbf{x},\omega)\mathbf{e}^{-i\omega t} \tag{3.81}$$

Substituting (3.81) into the generalized equations of motion (2.27) leads to

$$C_{iJKl}u^*_{KM,il}(\mathbf{x},\omega) + \rho\omega^2\delta_{JK}u^*_{KM}(\mathbf{x},\omega) = -\delta_{JM}\delta(\mathbf{x}) \tag{3.82}$$

The application of the Radon transform (see Appendix B) to that equation yields

$$\Gamma_{JK}\partial_s^2\,\widehat{u^*}_{KM}(s,\omega) + \rho\omega^2\delta_{JK}\widehat{u^*}_{KM}(s,\omega) = -\delta_{JM}\delta(s) \tag{3.83}$$

where s is the parameter of the Radon-transform, defined by $s = \boldsymbol{\eta}\cdot\mathbf{x}$ with $\boldsymbol{\eta}$ being a unit normal vector which defines the position on a unit radius sphere whose center is the observation point, andΓ_{JK} is the generalized Christoffel tensor defined as by

$$\Gamma_{JK} = C_{iJKl}n_in_l \tag{3.84}$$

The solution to equations (3.83) may be obtained as the superposition of the following three cases:

A. Generalized displacements due to the application of a mechanical point load

When a mechanical point load is applied at the origin $\mathbf{x} = 0$ in the x_m-direction, the elastic displacements u_{km} in the x_k direction, the electric potential u_{4m} and the magnetic potential u_{5m}, all of them evaluated at a point $\mathbf{x}$, are obtained from the following set of equations

$$\Gamma_{jk}\partial_s^2\,\widehat{u^*}_{km} + \Gamma_{j4}\partial_s^2\widehat{u^*}_{4m} + \Gamma_{j5}\partial_s^2\,\widehat{u^*}_{5m} + \rho\omega^2\delta_{jk}\widehat{u^*}_{km} = -\delta_{jm}\delta(s) \tag{3.85a}$$

$$\Gamma_{4k}\partial_s^2\,\widehat{u^*}_{km} + \Gamma_{44}\partial_s^2\widehat{u^*}_{4m} + \Gamma_{45}\partial_s^2\,\widehat{u^*}_{5m} = 0 \tag{3.85b}$$

$$\Gamma_{5k}\partial_s^2\,\widehat{u^*}_{km} + \Gamma_{54}\partial_s^2\widehat{u^*}_{4m} + \Gamma_{55}\partial_s^2\,\widehat{u^*}_{5m} = 0 \tag{3.85c}$$

B. Generalized displacements due to the application of a point charge

The elastic displacements in the x_k direction (u_{k4}), the electric potential (u_{44}) and the magnetic potential (u_{54}),all of them evaluated at a generic point $\mathbf{x}$, due to the application of an electrical point charge at the origin $\mathbf{x} = 0$, are obtained from the following set of equations

$$\Gamma_{jk}\partial_s^2\,\widehat{u^*}_{k4} + \Gamma_{j4}\partial_s^2\widehat{u^*}_{44} + \Gamma_{j5}\partial_s^2\,\widehat{u^*}_{54} + \rho\omega^2\delta_{jk}\widehat{u^*}_{k4} = 0 \tag{3.86a}$$

$$\Gamma_{4k}\partial_s^2\,\widehat{u^*}_{k4} + \Gamma_{44}\partial_s^2\widehat{u^*}_{44} + \Gamma_{45}\partial_s^2\,\widehat{u^*}_{54} = -\delta(s) \tag{3.86b}$$

$$\Gamma_{5k}\partial_s^2\,\widehat{u^*}_{k4} + \Gamma_{54}\partial_s^2\widehat{u^*}_{44} + \Gamma_{55}\partial_s^2\,\widehat{u^*}_{54} = 0 \tag{3.86c}$$

C. Generalized displacements due to the application of a magnetic monopole

The elastic displacements at a point $\mathbf{x}$ in the x_k direction (u_{k4}), the electric potential at $\mathbf{x}$ (u_{44}) and the magnetic potential at $\mathbf{x}$ (u_{54}) due to the application of magnetic monopole at the origin $\mathbf{x} = 0$, are obtained from the following set of equations

$$\Gamma_{jk}\partial_s^2\,\widehat{u^*}_{k5} + \Gamma_{j4}\partial_s^2\widehat{u^*}_{45} + \Gamma_{j5}\partial_s^2\,\widehat{u^*}_{55} + \rho\omega^2\delta_{jk}\widehat{u^*}_{k5} = 0 \tag{3.87a}$$

$$\Gamma_{4k}\partial_s^2\,\widehat{u^*}_{k5} + \Gamma_{44}\partial_s^2\widehat{u^*}_{45} + \Gamma_{45}\partial_s^2\,\widehat{u^*}_{55} = 0 \tag{3.87b}$$

$$\Gamma_{5k}\partial_s^2\,\widehat{u^*}_{k5} + \Gamma_{54}\partial_s^2\widehat{u^*}_{45} + \Gamma_{55}\partial_s^2\,\widehat{u^*}_{55} = -\delta(s) \tag{3.87c}$$

Let us first consider the case in which a mechanical point load is applied. From equations (3.85b) and (3.85c), the expressions of $\widehat{u^*}_{4m}$ and $\widehat{u^*}_{5m}$ as a function of $\widehat{u^*}_{km}$ may be obtained

$$\partial_s^2\,\widehat{u^*}_{4m} = \frac{\Gamma_{4k}\Gamma_{55} - \Gamma_{45}\Gamma_{5k}}{\Gamma_{45}\Gamma_{54} - \Gamma_{44}\Gamma_{55}}\partial_s^2\widehat{u^*}_{km} = \alpha_{k4}\partial_s^2\,\widehat{u^*}_{km} \tag{3.88}$$

$$\partial_s^2\,\widehat{u^*}_{5m} = \frac{\Gamma_{44}\Gamma_{5k} - \Gamma_{4k}\Gamma_{54}}{\Gamma_{45}\Gamma_{54} - \Gamma_{44}\Gamma_{55}}\partial_s^2\widehat{u^*}_{km} = \alpha_{k5}\partial_s^2\,\widehat{u^*}_{km} \tag{3.89}$$

The substitution of these relations in equation (3.85a) yields

$$\{Z_{jk}\partial_s^2 + \rho\omega^2\delta_{jk}\}\widehat{u^*}_{km} = -\delta_{jm}\delta(s) \tag{3.90}$$

where

$$Z_{jk} = \Gamma_{jk} + \alpha_{k4}\Gamma_{j4} + \alpha_{k5}\Gamma_{j5} \tag{3.91}$$

is the so-called reduced Christoffel tensor, which is symmetric and positive definite since (2.15) applies, and α_{k4} and α_{k5} are defined in equations (3.88) and (3.89). Thus, its eigenvalues are real-valued and positive. Recalling them as $\lambda_q = \rho c_q^2$, being c_q the phase velocities, they are obtained as the roots of the following characteristic equations

$$\det(Z_{jk} - \rho c_q^2\delta_{jk}) = 0 \tag{3.92}$$

Calling V_{jq} to the q-th eigenvector of Z_{jk}

$$Z_{jk}V_{kq} = \lambda_q V_{jq} \qquad \text{(no sum on q)} \tag{3.93}$$

it holds that

$$V_{jp}V_{jq} = \delta_{pq} \quad ; \quad V_{iq}V_{jq} = \delta_{ij} \tag{3.94}$$

so that these eigenvectors may be taken as orthonormal bases. $\widehat{u^*}_{km}$ can be then expressed in the new bases by applying the following transformation

$$\widehat{u^*}'_{hm} = V_{kh}\widehat{u^*}_{km} \quad \Longleftrightarrow \quad \widehat{u^*}_{km} = V_{kh}\widehat{u^*}'_{hm} \tag{3.95}$$

The substitution of this bases transformation into equation (3.90) and the premultiplication of the resulting equation by V_{jq} lead to

$$\{V_{jq}Z_{jk}V_{kh}\partial_s^2 + \rho\omega^2 V_{jq}\delta_{jk}V_{kh}\}\widehat{u^*}'_{hm} = -\delta_{jm}V_{jq}\delta(s) \tag{3.96}$$

That equation may be further reduced to a 1-D wave equation (for each fixed q and m) by considering the relations given by equations (3.93) and (3.94)

$$\{\lambda_q \partial_s^2 + \rho\omega^2\}\widehat{u^*}'_{qm} = -V_{mq}\delta(s) \tag{3.97}$$

whose solution is given by the wave equation

$$\overline{u^*}_{qm} = \frac{iV_{mq}}{2\rho c_q^2 k_q} e^{ik_q|s|} \tag{3.98}$$

where k_q is the wave number

$$k_q = \frac{\omega}{c_q} \tag{3.99}$$

The consideration of the inverse bases transformation (3.95) leads to

$$\widehat{u^*}_{km} = \frac{iV_{kq}V_{mq}}{2\rho c_q^2 k_q} e^{ik_q|s|} \tag{3.100}$$

Following now an analogous procedure to the one proposed Wang and Achenbach (1995) for anisotropic solids the resolution of the complete eigenvalue problem defined by (3.92) will be avoided. This procedure is based in the idea that $V_{kq}V_{mq}$ in equation (3.100) may be computed as

$$V_{kq}V_{mq} = \frac{E^q_{km}}{E^q_{pp}} \tag{3.101}$$

where

$$E^q_{km} = \mathrm{adj}\{Z_{km} - \rho c_q^2 \delta_{km}\} \tag{3.102}$$

Considering now the most general case in which the three phase velocities c_q are distinct, the equation (3.100) can be expressed as

$$\widehat{u^*}_{km} = \frac{iE^q_{km}}{2\rho c_q^2 k_q E^q_{pp}} e^{ik_q|s|} \tag{3.103}$$

Finally, the application of the inverse Radon transform leads to the u^*_{km} terms of the Green's functions

$$u^*_{km} = \frac{-1}{8\pi^2} \int\limits_{|\boldsymbol{\eta}|=1} \partial_s^2 \widehat{u^*}_{km} dS(\boldsymbol{\eta}) =$$
$$= \frac{1}{16\pi^2} \int\limits_{|\boldsymbol{\eta}|=1} \frac{E^q_{km}}{\rho c_q^2 E^q_{pp}} \left\{2\delta(\boldsymbol{\eta}\cdot\mathbf{x}) + ik_q\right\} e^{ik_q|\boldsymbol{\eta}\cdot\mathbf{x}|} dS(\boldsymbol{\eta}) \tag{3.104}$$

where the domain of integration is defined by the surface of a unit sphere $|\boldsymbol{\eta}| = 1$.

In the same way, the substitution of equation (3.103) into (3.88) and (3.89), and the application of the inverse Radon transform yields

$$u^*_{4m} = \frac{1}{16\pi^2} \int\limits_{|\boldsymbol{\eta}|=1} \frac{\alpha_{l4} E^q_{km}}{\rho c_q^2 E^q_{pp}} \left\{2\delta(\boldsymbol{\eta}\cdot\mathbf{x}) + ik_q\right\} e^{ik_q|\boldsymbol{\eta}\cdot\mathbf{x}|} dS(\boldsymbol{\eta}) \tag{3.105}$$

$$u^*_{5m} = \frac{1}{16\pi^2} \int\limits_{|\boldsymbol{\eta}|=1} \frac{\alpha_{l5} E^q_{km}}{\rho c_q^2 E^q_{pp}} \left\{2\delta(\boldsymbol{\eta}\cdot\mathbf{x}) + ik_q\right\} e^{ik_q|\boldsymbol{\eta}\cdot\mathbf{x}|} dS(\boldsymbol{\eta}) \tag{3.106}$$

An analogous procedure for *Problem B* and *Problem C* will let us to obtain the other terms of the fundamental solution. For *Problem B*, $\partial_s^2\widehat{u^*}_{44}$ and $\partial_s^2\widehat{u^*}_{54}$ may be expressed as functions of $\partial_s^2\widehat{u^*}_{k4}$ from equations (3.86b) and (3.86c) yielding to

$$\partial_s^2\widehat{u^*}_{44} = \alpha_{k4}\partial_s^2\widehat{u^*}_{k4} + \frac{\Gamma_{55}}{\alpha}\,\delta(s) \tag{3.107}$$

$$\partial_s^2\widehat{u^*}_{54} = \alpha_{k5}\partial_s^2\widehat{u^*}_{k4} - \frac{\Gamma_{54}}{\alpha}\,\delta(s) \tag{3.108}$$

where

$$\alpha = \Gamma_{45}\Gamma_{54} - \Gamma_{44}\Gamma_{55} \tag{3.109}$$

and the application of the inverse Radon transform will lead to

$$\begin{aligned} u^*_{44} &= \frac{-1}{8\pi^2}\int\limits_{|\boldsymbol{\eta}|=1} \partial_s^2 \widehat{u^*}_{44} dS(\boldsymbol{\eta}) \\ &= \frac{1}{16\pi^2}\int\limits_{|\boldsymbol{\eta}|=1} \alpha_{l4}\alpha_{j4}\frac{E^q_{lj}}{\rho c_q^2 E^q_{pp}}\left\{2\delta(\boldsymbol{\eta}\cdot\mathbf{x}) + ik_q\right\} e^{ik_q|\boldsymbol{\eta}\cdot\mathbf{x}|} dS(\boldsymbol{\eta}) \\ &- \frac{1}{8\pi^2}\int\limits_{|\boldsymbol{\eta}|=1} \frac{\Gamma_{55}}{\alpha}\delta(\boldsymbol{\eta}\cdot\mathbf{x}) dS(\boldsymbol{\eta}) \end{aligned} \tag{3.110}$$

$$\begin{aligned} u^*_{54} &= \frac{-1}{8\pi^2}\int\limits_{|\boldsymbol{\eta}|=1} \partial_s^2 \widehat{u^*}_{54} dS(\boldsymbol{\eta}) \\ &= \frac{1}{16\pi^2}\int\limits_{|\boldsymbol{\eta}|=1} \alpha_{l5}\alpha_{j4}\frac{E^q_{lj}}{\rho c_q^2 E^q_{pp}}\left\{2\delta(\boldsymbol{\eta}\cdot\mathbf{x}) + ik_q\right\} e^{ik_q|\boldsymbol{\eta}\cdot\mathbf{x}|} dS(\boldsymbol{\eta}) \\ &+ \frac{1}{8\pi^2}\int\limits_{|\boldsymbol{\eta}|=1} \frac{\Gamma_{54}}{\alpha}\delta(\boldsymbol{\eta}\cdot\mathbf{x}) dS(\boldsymbol{\eta}) \end{aligned} \tag{3.111}$$

Similarly, solution of *Problem C* will lead to

$$\begin{aligned} u^*_{55} &= \frac{1}{16\pi^2}\int\limits_{|\boldsymbol{\eta}|=1} \alpha_{l5}\alpha_{j5}\frac{E^q_{lj}}{\rho c_q^2 E^q_{pp}}\left\{2\delta(\boldsymbol{\eta}\cdot\mathbf{x}) + ik_q\right\} e^{ik_q|\boldsymbol{\eta}\cdot\mathbf{x}|} dS(\boldsymbol{\eta}) \\ &- \frac{1}{8\pi^2}\int\limits_{|\boldsymbol{\eta}|=1} \frac{\Gamma_{44}}{\alpha}\delta(\boldsymbol{\eta}\cdot\mathbf{x}) dS(\boldsymbol{\eta}) \end{aligned} \tag{3.112}$$

So, finally, the dynamic time-harmonic magnetoelectroelastic displacement Green's functions just obtained, which present a symmetry property such as $u^*_{KM}(\mathbf{x},\omega) = u^*_{MK}(\mathbf{x},\omega)$, may be recast into a compact form as

$$\begin{aligned} u^*_{KM} &= \frac{1}{16\pi^2}\int\limits_{|\boldsymbol{\eta}|=1} \frac{\varepsilon^q_{KM}}{\rho c_q^2 E^q_{pp}}\left\{2\delta(\boldsymbol{\eta}\cdot\mathbf{x}) + ik_q\right\} e^{ik_q|\boldsymbol{\eta}\cdot\mathbf{x}|} dS(\boldsymbol{\eta}) \\ &+ \frac{1}{8\pi^2}\int\limits_{|\boldsymbol{\eta}|=1} \Lambda_{KM}\delta(\boldsymbol{\eta}\cdot\mathbf{x}) dS(\boldsymbol{\eta}) \end{aligned} \tag{3.113}$$

where

$$\varepsilon^q_{KM} = \begin{cases} E^q_{km} & K,M = 1,2,3 \\ \alpha^K_l E^q_{lm} & K = 4,5 \quad ; \quad M = 1,2,3 \\ \alpha^K_l \alpha^M_j E^q_{lj} & K,M = 4,5 \end{cases} \tag{3.114}$$

and

$$\Lambda_{KM} = \frac{1}{\alpha}\left\{\Gamma_{KM}(\delta_{4K}\delta_{5M} + \delta_{5K}\delta_{4M}) - \frac{\Gamma_{44}\Gamma_{55}}{\Gamma_{KM}}(\delta_{4K}\delta_{4M} + \delta_{5K}\delta_{5M})\right\}$$

The obtained time-harmonic Green's functions may be split into a singular part plus a regular frequency dependent part. This decomposition is very useful for BEM implementation purposes, since the singular part coincides with the static solution except for a constant

$$u^*_{KM}(\mathbf{x},\omega) = u^{*S}_{KM}(\mathbf{x}) + u^{*R}_{KM}(\mathbf{x},\omega) \tag{3.115}$$

where

$$u^{*R}_{KM} = \frac{1}{16\pi^2}\int\limits_{|\boldsymbol{\eta}|=1} \frac{\varepsilon^q_{KM}}{\rho c_q^2 E^q_{pp}}\left\{2\delta(\boldsymbol{\eta}\cdot\mathbf{x}) + ik_q\right\} e^{ik_q|\boldsymbol{\eta}\cdot\mathbf{x}|}\, dS(\boldsymbol{\eta}) \tag{3.116}$$

$$u^{*S}_{KM} = \frac{1}{8\pi^2}\int\limits_{|\boldsymbol{\eta}|=1} \Lambda_{KM}\delta(\boldsymbol{\eta}\cdot\mathbf{x})\, dS(\boldsymbol{\eta}) \tag{3.117}$$

As the static singular part, fundamental solution recently derived by Buroni and Sáez (2010) can be used. Finally, the extended traction Green's functions as well as the kernels d^*_{IJ} and s^*_{IJ} needed for the implementation of the ETBIE may be obtained via the frequency-domain equivalent equations to (??-3.28)

$$p^*_{IK}(\boldsymbol{\xi},\mathbf{x},\omega) = N_s(\xi)C_{sIJr}u^*_{KJ,r}(\boldsymbol{\xi},\mathbf{x},\omega) \tag{3.118}$$

$$d^*_{IK}(\boldsymbol{\xi},\mathbf{x},\omega) = N_s(\xi)C_{sIJr}u^*_{KJ,r}(\boldsymbol{\xi},\mathbf{x},\omega) \tag{3.119}$$

$$s^*_{IK}(\boldsymbol{\xi},\mathbf{x},\omega) = N_s(\xi)C_{sIJr}p^*_{KJ,r}(\boldsymbol{\xi},\mathbf{x},\omega) \tag{3.120}$$

2-D time-harmonic Green's functions

The 2-D Green's functions may be obtained following the same procedure as for the 3-D case. In 2-D the lowercase (elastic) subscripts take values 1 and 2 only, whilst the uppercase (extended) subscripts take values 1, 2, 4 (electric) and 5 (magnetic). In this way, Green's functions are obtained in the form of line integrals along a unit circumference $|\mathbf{n}| = 1$ as (see works by Wang and Achenbach, 1994 or Wang and Zhang, 2005 for further details)

$$u^*_{KM}(\boldsymbol{\xi}, \mathbf{x}, \omega) = u^{*S}_{KM}(\boldsymbol{\xi}, \mathbf{x}) + u^{*R}_{KM}(\boldsymbol{\xi}, \mathbf{x}, \omega) \tag{3.121}$$

where

$$\begin{aligned} u^{*S}_{KM}(\boldsymbol{\xi}, \mathbf{x}) = &-\frac{1}{4\pi^2} \int\limits_{|\boldsymbol{\eta}|=1} \frac{\varepsilon^q_{KM}}{\rho c_q^2 E^q_{pp}} \log|\boldsymbol{\eta}\cdot\mathbf{x}|\, dL(\boldsymbol{\eta}) - \\ &-\frac{1}{4\pi^2} \int\limits_{|\boldsymbol{\eta}|=1} \Lambda_{KM} \log|\boldsymbol{\eta}\cdot\mathbf{x}|\; dL(\boldsymbol{\eta}) \end{aligned} \tag{3.122}$$

$$u^{*R}_{KM}(\boldsymbol{\xi}, \mathbf{x}, \omega) = \frac{1}{16\pi^2} \int\limits_{|\boldsymbol{\eta}|=1} \frac{\varepsilon^q_{KM}}{\rho c_q^2 E^q_{yy}} \Phi^R(k_q, |\boldsymbol{\eta}\cdot\mathbf{x}|)\, dL(\boldsymbol{\eta})$$

where, as it has already been said, the singular part coincides with the static fundamental solution except for a constant, ε^q_{KM} is given by (3.114) and

$$\Phi^R(k_q, |\boldsymbol{\eta}\cdot\mathbf{x}|) = \Phi(k_q|\boldsymbol{\eta}\cdot\mathbf{x}|) + 2\log(|\boldsymbol{\eta}\cdot\mathbf{x}|) \tag{3.123}$$

with

$$\Phi(\zeta) = i\pi e^{i\zeta} - 2[\cos(\zeta)ci(\zeta) + \sin(\zeta)si(\zeta)] \tag{3.124}$$

and ci and si are the integral cosine and the integral sine functions, which are defined as

$$ci(\zeta) = -\int\limits_{\zeta}^{\infty} \frac{\cos z}{z} dz \quad ; \quad si(\zeta) = -\int\limits_{\zeta}^{\infty} \frac{\sin z}{z} dz \tag{3.125}$$

The extended traction Green's functions may be obtained by the substitution of u^*_{KM} into the frquency domain equivalent generalized Hooke's law (3.118), while the kernels needed for the implementation of the ETBIE may be determined as in equations (3.119) and (3.120).

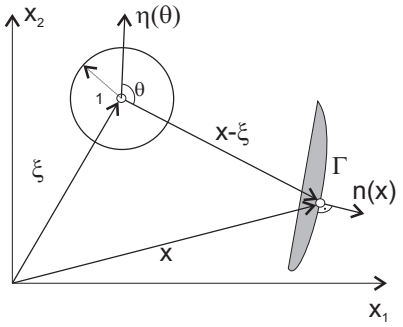

Figure 3.6: Integration circumference for frequency domain fundamental solution

The implementation of the fundamental solution will imply a double integration. One over the element and another one over a unit circle centered at the observation point, as shown in figure 3.6, where it can be noticed that the term $|\boldsymbol{\eta} \cdot \mathbf{x}|$ is equal to $|\mathbf{x} - \boldsymbol{\xi}| \cos(\theta)$

3.5.3 Numerical evaluation of the integrals

As it has been said, time-harmonic Green's functions may be split into a regular and a singular part, and so has been done in this work with the kernels needed for the implementation of the fundamental solution, in both EDBIE and ETBIE.

As we already know the singular part coincides with the static fundamental solution, except for a constant. Thus, the integration of it, will be

carried out as it has been analyzed in a previous section 3.4.2.

All the regular parts of the time-harmonic fundamental solution can be expressed as follows

$$u^{*R}_{KM}(\boldsymbol{\xi},\mathbf{x},\omega) = \frac{1}{8\pi^2}\int_{-\pi}^{\pi} \gamma^q_{KM}\Phi^R(k_q,|\mathbf{x}-\boldsymbol{\xi}||\cos\theta|)\,d\theta \tag{3.126}$$

$$p^{*R}_{KM}(\boldsymbol{\xi},\mathbf{x},\omega) = \frac{1}{8\pi^2}\int_{-\pi}^{\pi} \gamma^q_{KJ}\overline{\Gamma}_{MJ}k_q\Upsilon(k_q|\mathbf{x}-\boldsymbol{\xi}||\cos\theta|)\mathrm{sign}(\cos\theta)\,d\theta \tag{3.127}$$

$$\begin{aligned} d^{*R}_{KM}(\boldsymbol{\xi},\mathbf{x},\omega) &= \\ &= -\frac{1}{8\pi^2}\int_{-\pi}^{\pi} \overline{\overline{\Gamma}}_{KJ}\gamma^q_{MJ}k_q\Upsilon(k_q|\mathbf{x}-\boldsymbol{\xi}||\cos\theta|)\mathrm{sign}(\cos\theta)\,d\theta \end{aligned} \tag{3.128}$$

$$s^{*R}_{KM}(\boldsymbol{\xi},\mathbf{x},\omega) = -\frac{1}{8\pi^2}\int_{-\pi}^{\pi} \overline{\overline{\Gamma}}_{KJ}\gamma^q_{JS}\overline{\Gamma}_{MS}k_q^2\Phi(k_q|\mathbf{x}-\boldsymbol{\xi}||\cos\theta|)\,d\theta \tag{3.129}$$

where

- $\gamma^q_{KM} = \varepsilon^q_{KM}/(\rho c_q^2 E^q_{yy})$ and ρc_q^2, E^q_{yy} and ε^q_{KM} were defined, respectively, in equations (3.92), (3.102) and (3.114).

- $\overline{\Gamma}_{JK} = C_{rJKl}n_r\eta_l$ and $\overline{\overline{\Gamma}}_{JK} = C_{rJKl}N_r\eta_l$, being n_r, N_r and η_l the unit outward normals in the observation and collocation point and to the integration circumference, respectively.

- $\Upsilon(s) = -\pi e^{(is)} - 2[\cos(s)si(s) - \sin(s)ci(s)]$, where i is the imaginary unit number and si and ci are, respectively, the integral sine and cosine, as defined in equation(3.125).

Introducing now the expressions of the regular part of the fundamental solution into both boundary integral equations, the integrals to be solved are the following

$$I_1 = \int_{\Gamma_e} \left[\int_{-\pi}^{\pi} \gamma_{KM}^q \Phi^R(k_q, |\mathbf{x} - \boldsymbol{\xi}||\cos\theta|) d\theta \right] d\Gamma \tag{3.130}$$

$$I_2 = \int_{\Gamma_e} \left[\int_{-\pi}^{\pi} \gamma_{KJ}^q \overline{\Gamma}_{MJ} k_q \Upsilon(k_q|\mathbf{x} - \boldsymbol{\xi}||\cos\theta|) \mathrm{sign}(\cos\theta) d\theta \right] d\Gamma \tag{3.131}$$

$$I_3 = \int_{\Gamma_e} \left[\int_{-\pi}^{\pi} \overline{\overline{\Gamma}}_{KJ} \gamma_{MJ}^q k_q \Upsilon(k_q|\mathbf{x} - \boldsymbol{\xi}||\cos\theta|) \mathrm{sign}(\cos\theta) d\theta \right] d\Gamma \tag{3.132}$$

$$I_4 = \int_{\Gamma_e} \left[\int_{-\pi}^{\pi} \overline{\overline{\Gamma}}_{KJ} \gamma_{JS}^q \overline{\Gamma}_{MS} k_q^2 \Phi(k_q|\mathbf{x} - \boldsymbol{\xi}||\cos\theta|) d\theta \right] d\Gamma \tag{3.133}$$

The first three integrals can be evaluated with ordinary Gauss quadratures. Nevertheless, in the integrand in I_4 it appears again the function Φ, which have two main features. The first one is that it presents a $O\left[\ln\left(|\mathbf{x} - \boldsymbol{\xi}||\cos\left(\theta\right)|\right)\right]$ singularity when the collocation point tends to the observation one, and when $\theta \to \pm\pi/2$. The other characteristic is that it present and oscillatory behavior proportional to the product between the wave number, k_q and the distance between both the collocation and observation points.

The logarithmic singularity has been treated with logarithmic quadratures, while the oscillatory behavior would require the implementation of asymptotic approximations (Sáez and Domínguez, 2000), when high frequencies are involved or far field problems are analyzed.

3.6 Green's functions and numerical evaluation of the integrals. Time-domain case

In this work, the resolution of time-domain (transient) problems has been carried out by means of Lubich's convolution quadratures. The use of them allows the use of a Laplace domain fundamental solution instead of a time domain one. An important feature of these quadratures is that, although Laplace-domain Green's functions are used, not numerical inverse Laplace transformation is needed. This fact provides numerical stability to the method and makes the spatial and temporal discretizations rather independent.

The procedure to obtain Laplace domain fundamental solution is analogous to the one presented by Wang and Zhang (2005) for piezoelectric solids, based in the application of the Radon transform to the magnetoelectroelastic problem, as done in section 3.5.2. Consequently, Green's functions will present similar mathematical structure and the resulting fundamental solution can be split in a singular and a regular part, being the singular part equal to the static fundamental solution except for a constant. The expressions for the regular part of the Green's functions are

$$u^{*R}_{KM}(\boldsymbol{\xi}, \mathbf{x}, s) = \frac{1}{8\pi^2} \int_{-\pi}^{\pi} \gamma^q_{KM} \Psi^R \left(s/c_q, |\mathbf{x} - \boldsymbol{\xi}||\cos\theta|\right) \, d\theta \tag{3.134}$$

$$\begin{aligned} &p^{*R}_{KM}(\boldsymbol{\xi}, \mathbf{x}, s) = \\ &= \frac{1}{8\pi^2} \int_{-\pi}^{\pi} \gamma^q_{KJ} \overline{\Gamma}_{MJ} \frac{s}{c_q} \Psi' \left((s/c_q)|\mathbf{x} - \boldsymbol{\xi}||\cos\theta|\right) \operatorname{sign}(\cos\theta) \, d\theta \end{aligned} \tag{3.135}$$

$$d_{KM}^{*R}(\boldsymbol{\xi},\mathbf{x},s) = \\ = -\frac{1}{8\pi^2}\int_{-\pi}^{\pi}\overline{\overline{\Gamma}}_{KJ}\gamma_{MJ}^{q}\frac{s}{c_q}\Psi'\left((s/c_q)|\mathbf{x}-\boldsymbol{\xi}||\cos\theta|\right)\mathrm{sign}(\cos\theta)\,d\theta \qquad (3.136)$$

$$s_{KM}^{*R}(\boldsymbol{\xi},\mathbf{x},s) = \\ = -\frac{1}{8\pi^2}\int_{-\pi}^{\pi}\overline{\overline{\Gamma}}_{KJ}\gamma_{JS}^{q}\overline{\Gamma}_{MS}\left(\frac{s}{c_q}\right)^2\Psi\left((s/c_q)|\mathbf{x}-\boldsymbol{\xi}||\cos\theta|\right)\,d\theta \qquad (3.137)$$

where s is the Laplace parameter and

- γ_{KM}^{q}, $\overline{\Gamma}_{JK}$ and $\overline{\overline{\Gamma}}_{JK}$ were defined in section 3.5.3.
- $\Psi(z) = -[e^{-z}Ei(z) + e^{z}Ei(-z)]$, being z a complex variable and $Ei(z)$ the exponential integral defined as

$$\mathrm{Ei}(z) = -\int_{-1}^{\infty}\frac{e^{-zt}}{t}dt\;;\;\; \mathrm{Ei}(-z) = -\int_{1}^{\infty}\frac{e^{-zt}}{t}dt\,, \qquad (3.138)$$

Introducing now the expressions of the regular part of the fundamental solution into both boundary integral equations, the integrals to be solved are the following

$$I_1 = \int_{\Gamma_e}\left[\int_{-\pi}^{\pi}\gamma_{KM}^{q}\Psi^{R}\left(s/c_q,|\mathbf{x}-\boldsymbol{\xi}||\cos\theta|\right)\,d\theta\right]d\Gamma \qquad (3.139)$$

$$I_2 = \int_{\Gamma_e}\left[\int_{-\pi}^{\pi}\gamma_{KJ}^{q}\overline{\Gamma}_{MJ}\frac{s}{c_q}\Psi'\left((s/c_q)|\mathbf{x}-\boldsymbol{\xi}||\cos\theta|\right)\mathrm{sign}(\cos\theta)d\theta\right]\,d\Gamma \qquad (3.140)$$

$$I_3 = \int_{\Gamma_e}\left[\int_{-\pi}^{\pi}\overline{\overline{\Gamma}}_{KJ}\gamma_{MJ}^{q}\frac{s}{c_q}\Psi'\left((s/c_q)|\mathbf{x}-\boldsymbol{\xi}||\cos\theta|\right)\mathrm{sign}(\cos\theta)d\theta\right]\,d\Gamma \qquad (3.141)$$

$$I_4 = \int_{\Gamma_e}\left[\int_{-\pi}^{\pi}\overline{\overline{\Gamma}}_{KJ}\gamma_{JS}^{q}\overline{\Gamma}_{MS}\left(\frac{s}{c_q}\right)^2\Psi\left((s/c_q)|\mathbf{x}-\boldsymbol{\xi}||\cos\theta|\right)d\theta\right]\,d\Gamma \qquad (3.142)$$

The way to evaluate those integrals is analogous to the time-harmonic case and their numerical computation has been analyzed in section 3.5.3.

3.7 Computation of fracture parameters

3.7.1 Computation of the Extended Stress Intensity Factors

For the computation of the ESIF, in this work the displacement method has been used, using the extrapolation monopoint formulation proposed by Sáez et al. (1995). For this purpose, the extended displacement on the nearest node to the crack tip must be computed and then substituted, as well as its coordinates, in the analytical expressions of the asymptotic fields (2.36). An algebraic system of equations shall be obtained, which solution provides the stress, electric displacement and magnetic induction intensity factors.

Due to the generality of the regularization process followed in this work, it is possible the use of a discontinuous quarter point element which contains the crack tip. This element, as it can be seen in figure 3.7, is divided by the central node in two segments, which length are $L/4$ and $3L/4$ respectively, being l the whole length of the element. In this quarter point discontinuous element, which must be a straight element (Martínez and Domínguez, 1984) in order to capture properly the discontinuity in $\theta = \pm\pi$, the relation between the natural and the radial coordinate of the polar system with origin on the crack tip is

$$\zeta = 2\sqrt{\frac{r}{L}} - 1 \tag{3.143}$$

That relation allows to reproduce the $\sqrt{r}$ behavior around the crack tip of the extended displacements. This fact, together with the existence of a collocation point very close to the crack tip allows the direct evaluation

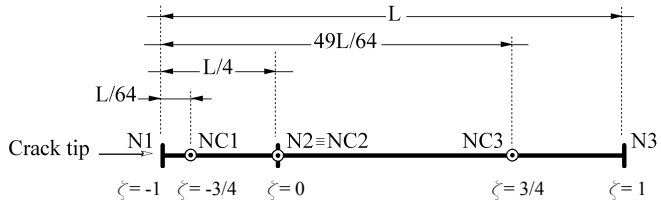

Figure 3.7: Quarter point discontinuous element

of the ESIF with a minimal postprocess of the displacement and with an excellent accuracy in the results.

The expressions of the ESIF for magnetoelectroelastic were obtained first by Gao et al. (2003a) as an extension of those obtained by Suo et al. (1992) for piezoelectric solids. Particularizing these expressions for the collocation point *NC1* (see figure 3.7), the ESIF may be directly computed from

$$\begin{pmatrix} K_{II} \\ K_I \\ K_{IV} \\ K_V \end{pmatrix} = \sqrt{\frac{8\pi}{l}} Y^{-1} \begin{pmatrix} \Delta u_1|_{r=L/64} \\ \Delta u_2|_{r=L/64} \\ \Delta \phi|_{r=L/64} \\ \Delta \varphi|_{r=L/64} \end{pmatrix} \tag{3.144}$$

where

$$\mathbf{Y} = \mathrm{Re}(i\mathbf{A}\mathbf{B}^{-1}) \tag{3.145}$$

is the Irwin matrix and $\mathbf{A}$ and $\mathbf{B}$ are the matrices obtained by solving the problem defined in (2.23).

In dynamic problems, the ESIF shall be defined in the corresponding domain (frequency or time domain), but the way to compute them is the same as for the static case, with the only difference that the displacements are also a function of either the frequency or time.

3.7.2 Computation of the Energy Release Rates

Tian and Rajapakse (2005b) defined a total energy release rate (ERR) for magnetoelectroelastic solids. It can be obtained from the ESIF as

$$G = \frac{1}{2}\mathbf{K}^T\mathbf{Y}\mathbf{K} \tag{3.146}$$

where

$$\mathbf{K} = \begin{pmatrix} K_{II} \\ K_I \\ K_{IV} \\ K_V \end{pmatrix} \tag{3.147}$$

In equation (3.146), the mechanical energy release rates (modes I and II) as well as the electric and magnetic ones are involved. Each term of the total ERR may be calculated as

$$G_I^M = \frac{1}{2}(Y_{21}K_IK_{II} + Y_{22}K_I^2 + Y_{23}K_IK_{IV} + Y_{24}K_IK_V) \tag{3.148a}$$

$$G_{II}^M = \frac{1}{2}(Y_{11}K_{II}^2 + Y_{22}K_{II}K_I + Y_{13}K_{II}K_{IV} + Y_{24}K_{II}K_V) \tag{3.148b}$$

$$G^{ELEC} = \frac{1}{2}(Y_{31}K_{IV}K_{II} + Y_{32}K_{IV}K_I + Y_{33}K_{IV}^2 + Y_{34}K_{IV}K_V) \tag{3.148c}$$

$$G^{MAGN} = \frac{1}{2}(Y_{41}K_VK_{II} + Y_{42}K_VK_I + Y_{43}K_VK_{IV} + Y_{44}K_V^2) \tag{3.148d}$$

Let us remark that a positive value denotes *released energy*, whilst a negative value represents *absorbed energy*.

Chapter 4

Results

4.1 Introduction

In this chapter, a wide number of static, frequency domain and transient fracture mechanics problems will be solved via the hypersingular formulation of the BEM previously introduced, under the assumption of impermeable cracks. In all cases, in order to validate the formulation, the proposed method will be first used to solve problems already studied with different techniques.

In all cases impermeable and self-equilibrated cracks in $BaTiO_3$–$CoFe_2O_4$ with a phase volume V_f=0.5 composite will be considered and its effective material properties are shown in table 4.1. The elastic stiffness tensor, the dielectric permittivities and the magnetic permeabilities, as well as the piezoelectric and piezomagnetic coefficientes, are obtained by the use of the *phase rule*, which is given by

$$\kappa_{ij}^{c} = \kappa_{ij}^{i} \cdot V_f + \kappa_{ij}^{m} \cdot (1 - V_f) \tag{4.1}$$

where κ_{ij} is one of the properties mentioned above, the superscripts i and m denote each phase and V_f is the phase volume. This rule can not be applied for the determination of the electromagnetic constants, since no electromagnetic coupling is present in any of the single phases. Such coupling can not been derived in a general way, since it is necessary a microstructural analysis which considers the inclusions shape.

Table 4.1: Material properties of $BaTiO_3$–$CoFe_2O_4$ (with V_f=0.5)

Properties	$BaTiO_3$	$CoFe_2O_4$	V_f=0.5
$c_{11}(GPa)$	166	286	226
$c_{12}(GPa)$	78	170	125
$c_{22}(GPa)$	162	269.5	216
$c_{66}(GPa)$	43	45.3	44
$e_{16}(C/m^2)$	11.6	0	5.8
$e_{21}(C/m^2)$	-4.4	0	-2.2
$e_{22}(C/m^2)$	18.6	0	9.3
$\epsilon_{11}(\times 10^{-10}C^2/Nm^2)$	112	0.8	56.4
$\epsilon_{12}(\times 10^{-10}C^2/Nm^2)$	126	0.93	63.5
$h_{16}(N/Am)$	0	550	275
$h_{21}(N/Am)$	0	580.3	290.2
$h_{22}(N/Am)$	0	699.7	350
$\gamma_{11}(\times 10^{-6}Ns^2/C^2)$	5	590	297
$\gamma_{12}(\times 10^{-6}Ns^2/C^2)$	10	157	350
$\beta_{11}(\times 10^{-12}Ns/VC)$	-	-	5.367
$\beta_{12}(\times 10^{-12}Ns/VC)$	-	-	2737.5

In this work, the values of the properties corresponding to fibrous com-

posites have been considered. Some authors, like Li and Dunn (1998) (where the values adopted here were obtained) published graphics which provide electromagnetic couplings, while others, such as Nan (1994) derived analytical expressions for them.

4.2 Static results

In this section, some static problems will be solved, as it has been said, considering in all cases a $BaTiO_3 - CoFe_2O_4$ composite with a $V_f = 0.5$. First, the proposed formulation will be validated by the comparison with analytical and semianalytical results available in the literature. In this epigraph, only cracks in unbounded domains will be analyzed, since static results for finite cracked domains will be presented later on, in chapters 5 and 6.

4.2.1 Straight crack in an unbounded domain

The analytical solution of straight crack in an infinite domain subjected to far field uniform electromagnetomechanic loads was first derived anallytically by Gao et al. (2003a), who established that the value of the extended stress intensity factors for such a case are independent of the material properties and of the (extended) loads in other directions. For impermeable cracks, those ESIF take the following values

$$K_I = \sigma_{22}^{\infty}\sqrt{\pi a}, \quad K_{II} = \sigma_{21}^{\infty}\sqrt{\pi a}, \quad K_{IV} = D_2^{\infty}\sqrt{\pi a}, \quad K_V = B_2^{\infty}\sqrt{\pi a}. \tag{4.2}$$

The problem is illustrated in figure 4.1, while in table 4.2, the values of the ESIF are listed for two different meshes. In the first one five equal

quadratic elements are used, while in the second one the mesh is carried out with ten equal elements. An excellent agreement is obtained in both cases.

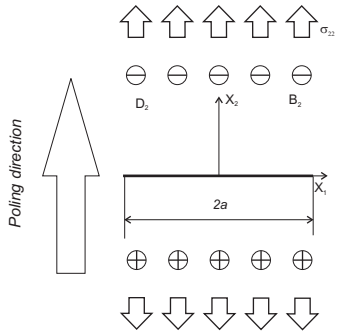

Figure 4.1: Straight crack under remote electromagnetomechanic loading

Table 4.2: Extended SIFs for a Griffith crack in a magnetoelectroelastic solid.

ESIF	5 Elements	10 Elements
$K_I/K_I^{Analytic}$	0.9981	0.9989
$K_{II}/K_{II}^{Analytic}$	0.9981	0.9989
$K_{IV}/K_{IV}^{Analytic}$	0.9981	0.9989
$K_V/K_V^{Analytic}$	0.9981	0.9989

Let us now consider a Griffith crack subjected to three different electromagnetomechanical loading combinations, whose values are shown in table 4.3.

In figure 4.2, normalized Δu_2 is plotted for the three combinations considered. It can be easily noticed that the presence of positive electromagnetic loading make the crack tends to open what, consequently, increase the ten-

Table 4.3: Loading combinations considered for the analysis of a Griffith crack in a magnetoelectroelastic media

	Combination (a)	Combination (b)	Combination (c)
$\sigma_{22}^{\infty}(N/m^2)$	$\neq 0$	$\neq 0$	$\neq 0$
$D_2^{\infty}(C/N)$	0	$10^{-9}\sigma_{22}^{\infty}$	$-10^{-9}\sigma_{22}^{\infty}$
$B_2^{\infty}(A^{-1}\cdot m)$	0	$10^{-6}\sigma_{22}^{\infty}$	$-10^{-6}\sigma_{22}^{\infty}$

dency to the fracture.

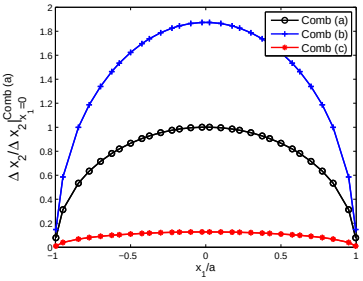

Figure 4.2: Δu_2 in a Griffith crack subjected to three different combinations of remote loading

In table 4.4 the values for total energy release rate as well as total mechanical energy release rate are included, where all the values have been normalized with the total energy release rate for pure mechanical load. It can be noticed that total energy release rate decreases as soon as either positive or negative electromagnetic loadings are applied, even when the combination increases the crack opening displacement (*combination b*). This fact implies that the maximum of the total energy release rate can not be a suitable fracture criteria for magnetoelectroelastic solids.

Table 4.4: Energy Release Rates for Griffith crack in a magnetoelectroelastic solid.

ERR	Combination (a)	Combination (b)	Combination (c)
G^*_{TOT}	1.0000	-8.8029	-12.2940
G^*_{I+II}	1.0000	1.8728	0.1272

4.2.2 Two parallel cracks

The case in which two parallel cracks with variable relative position in an unbounded magnetoelectroelastic domain and subjected to a combination of mechanic, electric and magnetic loading is now considered, as shown in figure 4.3. This problem was first solved by Tian and Gabbert (2004) for the material considered in this section.

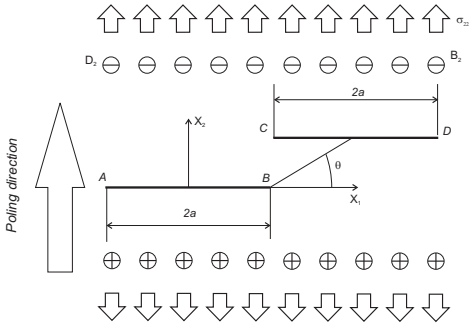

Figure 4.3: Two parallel cracks under remote electromagnetomechanic loading

Both cracks were meshed with ten equal quadratic elements. In figure 4.4, the normalized mode I stress intensity factor as well as the normalized magnetic induction intensity factor (both evaluated at crack tip

A) are plotted for different values of the angle θ and for a set of loadings defined by *combination (a)* in table 4.5. In figure 4.5, the normalized mode I energy release rate at crack tip A is plotted for two loading combinations defined as *combination (b)* in table 4.5. In all cases an excellent agreement is obtained.

Table 4.5: Loading combinations considered for the analysis of a two parallel cracks

	Combination (a)	Combination (b)
$\sigma_{22}^{\infty}(N/m^2)$	$\neq 0$	$\neq 0$
$D_2^{\infty}(C/N)$	0	$10^{-8}\sigma_{22}^{\infty}$
$B_2^{\infty}(A^{-1}\cdot m)$	$\pm 10^{-6}\sigma_{22}^{\infty}$	$\pm 10^{-6}\sigma_{22}^{\infty}$

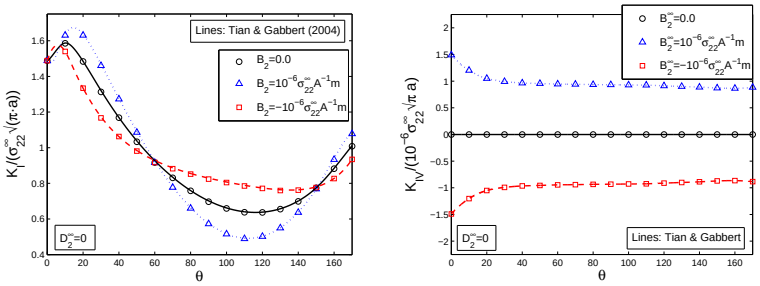

Figure 4.4: Normalized K_I (left) and K_{IV} (right) at crack tip A versus angle θ for two parallel cracks

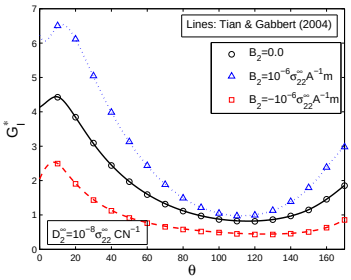

Figure 4.5: Normalized mode I ERR at crack tip A versus angle θ for two parallel cracks

4.2.3 Branched crack in an infinite domain

A branched crack in a magnetoelectroelastic infinite plane subjected to a remote combination of electromagnetomechanic loading is next studied. The geometry is illustrated in figure 4.6 and two different sets of far field electromagnetic loadings are first considered (sets *(a)* and *(b)* in table 4.6). The mesh consists in ten quadratic elements for the main crack and four for the branch.

Table 4.6: Loading combinations considered for the analysis of a branched crack

	Comb. (a)	Comb. (b)	Comb. (c)	Comb. (d)
$\sigma_{22}^{\infty}(N/m^2)$	$\neq 0$	$\neq 0$	$\neq 0$	$\neq 0$
$D_2^{\infty}(C/N)$	0	$10^{-8}\sigma_{22}^{\infty}$	$\pm 10^{-8}\sigma_{22}^{\infty}$	$\pm 10^{-8}\sigma_{22}^{\infty}$
$B_2^{\infty}(A^{-1}\cdot m)$	$\pm 10^{-6}\sigma_{22}^{\infty}$	$\pm 10^{-6}\sigma_{22}^{\infty}$	0	$\pm 10^{-6}\sigma_{22}^{\infty}$

In figure 4.7, the normalized mechanical stress intensity factors at crack tip C versus the branch angle are shown for both combinations of loads. It

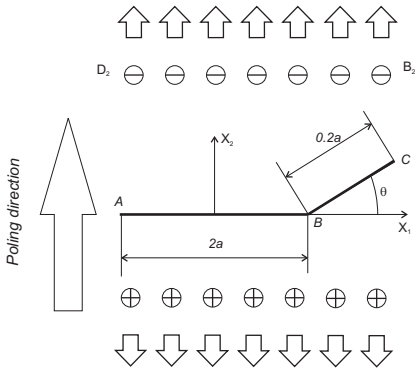

Figure 4.6: Branched crack: geometry and loads

can be noticed that positive and negative magnetic loads induce opposite effects on both modes I and II SIF and that there exist certain angles for which the magnetic loading has no effect on them. These angles are not affected by the presence of electric loadings, as can be seen by comparison between figures 4.7 (left) and 4.7 (right). In particular, the so-called neutral magnetic loading angles are $\theta_I^{NML} = 44.3^o$ and $\theta_{II}^{NML} = 38.1^o$.

In figure 4.8, the normalized EDIF and MIIF are plotted for both combination of loads. As expected, and according to the results by Gao et al. (2003a), almost no influence of the electric and magnetic loading in the MIIF and EDIF, respectively, is found.

In figure 4.9, the normalized mechanical energy release rates at crack tip C versus the branch angle are shown for both combinations of loads. The magnitudes are normalized with the total ERR corresponding to a Griffith crack with the same length as the mother crack and subjected only to a mechanical load.

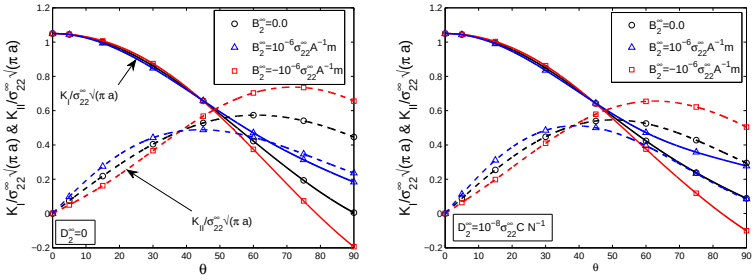

Figure 4.7: Normalized mechanical stress intensity factors at crack tip C versus branch angle θ for a magnetomechanical loading combination (left) and a full electromagnetomechanic loading combination (right)

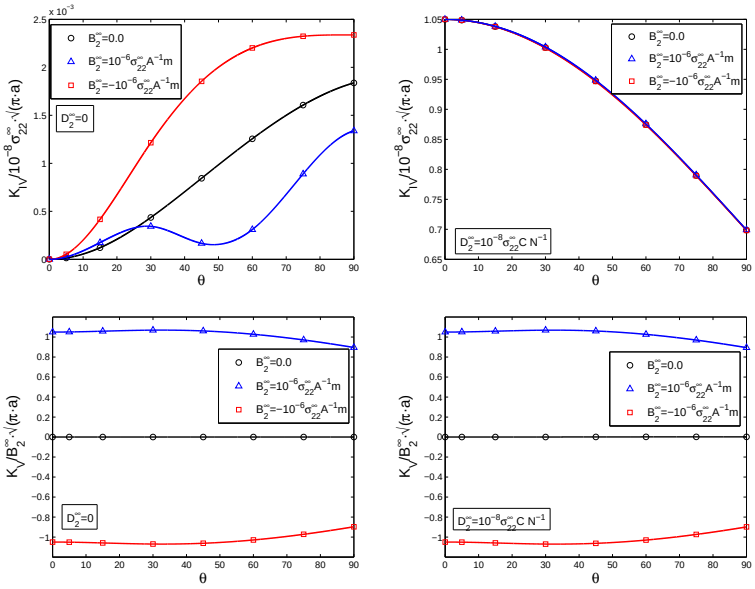

Figure 4.8: EDIF and MIIF at a crack tip C versus branch angle θ

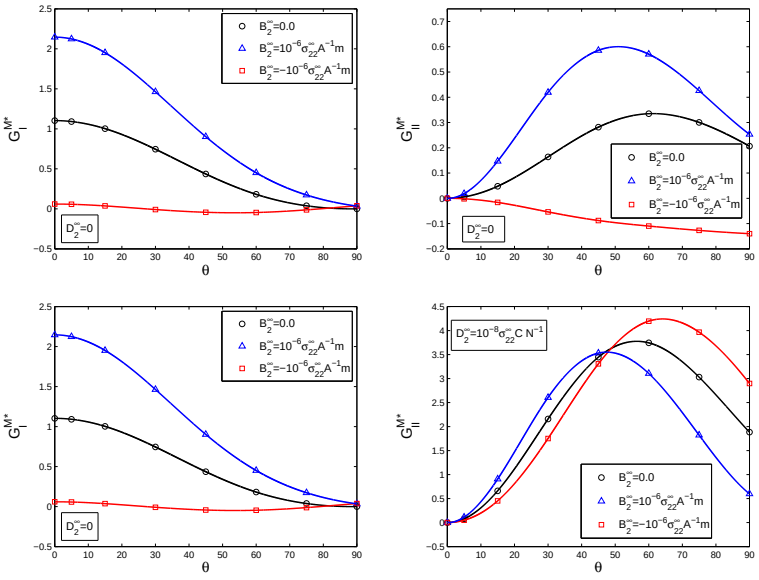

Figure 4.9: Mechanical energy release rates for combinations (a) and (b)

As we know, no fracture criteria is unanimously accepted for magneto-electroelastic materials. However, by observing figure 4.9 a first approach to a criteria may be proposed. Since the total energy release rate decreases as soon as either electric or magnetic loading are applied, even when they are positive. It seems clear that the maximum of the total ERR can not be used as a fracture criteria. Moreover, under the polarization direction and principal axes considered, it may be expected that the branched crack has a bigger tendency to grow if the branch angle θ is equal to zero and, since the maximum of the total mechanical ERR is reached just for $\theta = 0^o$, the maximum of such magnitude might be considered as a fracture criteria. This consideration is in agreement with the one proposed by Park and Sun (1995)

for piezoelectric materials (which present, as it is already known, a similar behavior to magnetoelectroelastic solids). Let us remark that the criteria proposed herein is only a first approach and, obviously, would require of experimental analysis of crack growth in magnetoelectroelastic solids, as well as a more extensive numerical analysis of different problems.

Loading sets defined as combinations *(c)* and *(d)* in table 4.6 are now considered. Mechanical and magnetic loadings will be now fixed, whilst the electric loading will take different values. Normalized mechanical stress intensity factors for such combinations are shown in figure 4.10. Similar conclusions to the previous cases analyzed can be drawn. In particular, there exist two neutral electric loading angles, one for each mechanical fracture mode, which are independent of the presence of magnetic loads, which take the following values: $\theta_I^{NEL} = 59.6^{\text{o}}$ and $\theta_{II}^{NEL} = 48.1^{\text{o}}$.

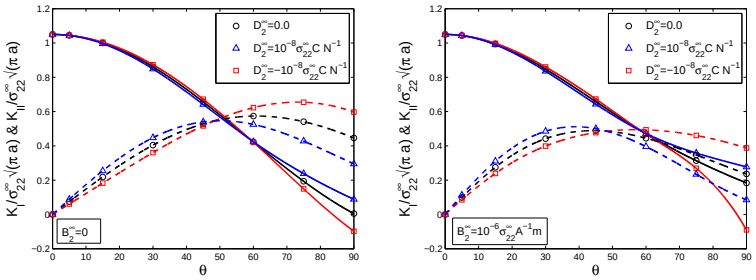

Figure 4.10: Normalized mechanical stress intensity factors at crack tip C versus branch angle θ for combinations (c) (left) and a (d) (right)

4.2.4 Circular arch crack in an infinite domain

A circular arch crack subjected to far field electromagnetomechanic loads like the one in figure 4.11 is next considered. A 10 elements mesh is used to discretize the crack, being the ones at the tips very small (arch length/30) quarter-point straight elements whilst the rest are curved quadratic discontinuous boundary elements. Identical mechanical positive loading is considered for all the cases and two sets of remote electromagnetic loadings are analyzed, listed in table 4.7.

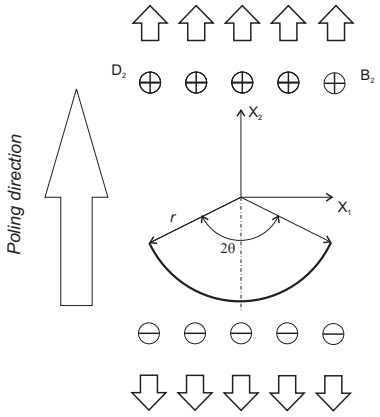

Figure 4.11: Circular arch crack: geometry and loads

Figure 4.12 shows the normalized modes I and II stress intensity factor ($K^*_{I,II} = K_{I,II}/\sigma^\infty_{22}\sqrt{\pi r \sin\theta}$, being r the arch radius) versus the arch angle, for the two load combinations considered. When $D^\infty_2 = 0$, figure 4.12 (left) shows again that positive and negative magnetic load induces an opposite effect on both the mode I and mode II SIF. However, when electric loading comes into play ($D^\infty_2 = 10^{-8}\sigma^\infty_{22}CN^{-1}$), figure 4.12 (right) illustrates how the SIF are hardly affected, for the electric and magnetic loading magnitudes

Table 4.7: Loading combinations considered for the analysis of a circular arch crack

	Comb. (a)	Comb. (b)	Comb. (c)	Comb. (d)
$\sigma_{22}^{\infty}(N/m^2)$	$\neq 0$	$\neq 0$	$\neq 0$	$\neq 0$
$D_2^{\infty}(C/N)$	0	$10^{-8}\sigma_{22}^{\infty}$	$\pm 10^{-8}\sigma_{22}^{\infty}$	$\pm 10^{-8}\sigma_{22}^{\infty}$
$B_2^{\infty}(A^{-1}\cdot m)$	$\pm 10^{-6}\sigma_{22}^{\infty}$	$\pm 10^{-6}\sigma_{22}^{\infty}$	0	$\pm 10^{-6}\sigma_{22}^{\infty}$

considered in this case.

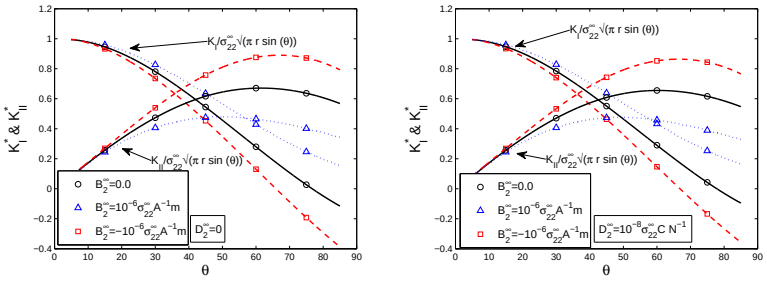

Figure 4.12: Normalized mechanical stress intensity factor for a circular arch crack under static loads.

Normalized total mechanical ERR ($G^{M*} = (G_I^M + G_{II}^M)/\frac{\pi r \sin\theta}{2}(\sigma_{22}^{\infty})^2$) versus θ are plotted in figure 4.13, where it is illustrated how a positive electric load triggers the total mechanic ERR.

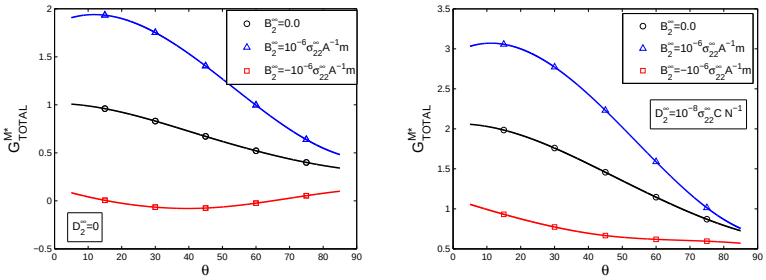

Figure 4.13: Total Energy Release Rate for a circular arch crack under static loads.

4.3 Time-harmonic results

In this section, some problems in which plane waves are impinging on impermeable cracks in magnetoelectroelastic solids will be solved, plotting, in all cases, the normalized ESIF against the wave frequency. Without lack of generality in the proposed formulation, only longitudinal (L) waves will be analyzed.

4.3.1 Plane harmonic waves in magnetoelectroelastic solids

For solving dynamic fracture mechanics it is necessary to obtain first the boundary conditions which shall be applied on both crack surfaces. Let us assume that the incident wave impinges along the x_2-axis, so the following extended displacements vector can be defined

$$\left\{ \begin{array}{c} u_1 \\ u_2 \\ \phi \\ \varphi \end{array} \right\} = \left\{ \begin{array}{c} 0 \\ u_0 \\ \phi_0 \\ \varphi_0 \end{array} \right\} e^{\frac{i\omega x_2}{c_L}} \tag{4.3}$$

where the longitudinal wave velocity, c_L, is given by

$$c_L = \sqrt{\frac{1}{\rho}\left(c_{22} + \varkappa_1 e_{22} + \varkappa_2 h_{22}\right)} \tag{4.4}$$

where

$$\varkappa_1 = \frac{\gamma_{22}e_{22} - \beta_{22}h_{22}}{\gamma_{22}\epsilon_{22} - \beta_{22}^2} \quad ; \quad \varkappa_2 = \frac{\epsilon_{22}h_{22} - \beta_{22}e_{22}}{\gamma_{22}\epsilon_{22} - \beta_{22}^2} \tag{4.5}$$

and ρ is the mass density.

The substitution of equation (4.3) in the behavior law yields to

$$\begin{pmatrix} \sigma_{11} \\ \sigma_{22} \\ \sigma_{12} \\ D_1 \\ D_2 \\ B_1 \\ B_2 \end{pmatrix} = \begin{pmatrix} c_{11} & c_{12} & 0 & 0 & e_{21} & 0 & \dots \\ c_{12} & c_{22} & 0 & 0 & e_{22} & 0 & \dots \\ 0 & 0 & c_{66} & e_{16} & 0 & h_{16} & \dots \\ 0 & 0 & e_{16} & -\epsilon_{11} & 0 & -\beta_{11} & \dots \\ e_{21} & e_{22} & 0 & 0 & -\epsilon_{22} & 0 & \dots \\ 0 & 0 & h_{16} & -\beta_{11} & 0 & -\gamma_{11} & \dots \\ h_{21} & h_{22} & 0 & 0 & -\beta_{22} & 0 & \dots \end{pmatrix} \tag{4.6}$$

$$\begin{pmatrix} \dots & h_{11} \\ \dots & h_{22} \\ \dots & 0 \\ \dots & 0 \\ \dots & -\beta_{22} \\ \dots & 0 \\ \dots & -\gamma_{22} \end{pmatrix} \begin{pmatrix} u_{1,1} \\ u_{2,2} \\ u_{1,2} + u_{2,1} \\ \phi_{,1} \\ \phi_{,2} \\ \varphi_{,1} \\ \varphi_{,2} \end{pmatrix} = \begin{pmatrix} c_{12}u_0 + e_{21}\phi_0 + h_{21}\varphi_0 \\ c_{22}u_0 + e_{22}\phi_0 + h_{22}\varphi_0 \\ 0 \\ 0 \\ e_{22}u_0 - \epsilon_{22}\phi_0 - \beta_{22}\varphi_0 \\ 0 \\ h_{22}u_0 - \beta_{22}\phi_0 - \gamma_{22}\varphi_0 \end{pmatrix} \frac{i\omega}{c_L} e^{\frac{i\omega x_2}{c_L}}$$

By the imposition now of the impermeable crack face boundary condition, a relation between the different amplitudes of the generalized displacement vector can be obtained

$$\phi_0 = \varkappa_1 u_0 \quad ; \quad \varphi_0 = \varkappa_2 u_0 \tag{4.7}$$

And finally, the extended tractions which shall be applied at the crack surface with outward unit normal $\boldsymbol{n} = (n_1, n_2)$ are given by

$$p_I = \begin{cases} p_1 = \sum_{j=1}^{2} \sigma_{1j}\, n_j = \dfrac{C_{12} + e_{21}\varkappa_1 + h_{21}\varkappa_2}{C_{22} + e_{22}\varkappa_1 + h_{22}\varkappa_2} n_1 \sigma_0 e^{\frac{i\omega x_2}{c_L}} & I = 1 \\ p_2 = \sum_{j=1}^{2} \sigma_{2j}\, n_j = n_2 \sigma_0 e^{\frac{i\omega x_2}{c_L}} & I = 2 \\ D_n = \sum_{j=1}^{2} D_j\, n_j = 0 & I = 4 \\ B_n = \sum_{j=1}^{2} B_j\, n_j = 0 & I = 5 \end{cases} \tag{4.8}$$

where

$$\sigma_0 = (C_{22} + e_{22}\varkappa_1 + h_{22}\varkappa_2)\, \frac{i\omega}{c_L} u_0 \tag{4.9}$$

Let us now introduce some quantities which will be used in this section for normalization purposes

$$c_S = \sqrt{\frac{c_{66}}{\rho}} \quad ; \quad \nu = \frac{\epsilon_{22}}{e_{22}} \quad ; \quad \mu = \frac{\gamma_{22}}{h_{22}} \tag{4.10}$$

4.3.2 Straight crack in an infinite domain

To the author's knowledge, no results for plane time-harmonic problems in magnetoelectroelastic solids were available when this work was carried out. Thus, to check the presented formulation and taking into account that piezoelectric behavior can be understood, from a mathematical point of view, as a degenerated case of the magnetoelectroelastic behavior, the problem of L-waves impinging on a Griffith crack in a PZT-6B material is solved and results compared with those obtained semianallytically by Shindo and Ozawa (1990). Material properties are shown in table 4.3.2, while the incident wave motion for such a case is defined by

$$\begin{pmatrix} \sigma_{11} \\ \sigma_{22} \\ \sigma_{12} \\ D_1 \\ D_2 \end{pmatrix} = \begin{pmatrix} c_{11} & c_{12} & 0 & 0 & e_{21} \\ c_{12} & c_{22} & 0 & 0 & e_{22} \\ 0 & 0 & c_{66} & e_{16} & 0 \\ 0 & 0 & e_{16} & -\epsilon_{11} & 0 \\ e_{21} & e_{22} & 0 & 0 & -\epsilon_{22} \end{pmatrix} \begin{pmatrix} u_{1,1} \\ u_{2,2} \\ u_{1,2}+u_{2,1} \\ \phi_{,1} \\ \phi_{,2} \end{pmatrix} =$$

$$= \begin{pmatrix} c_{12}u_0 + e_{21}\phi_0 \\ c_{22}u_0 + e_{22}\phi_0 \\ 0 \\ 0 \\ e_{22}u_0 - \epsilon_{22}\phi_0 \end{pmatrix} \frac{i\omega}{c_L} e^{\frac{i\omega x_2}{c_L}} \tag{4.11}$$

Table 4.8: Material properties of PZT-6B

Properties	$PZT-6B$
$c_{11}(GPa)$	168
$c_{12}(GPa)$	60
$c_{22}(GPa)$	163
$c_{66}(GPa)$	27.1
$e_{16}(C/m^2)$	4.6
$e_{21}(C/m^2)$	-0.9
$e_{22}(C/m^2)$	7.1
$\epsilon_{11}(\times 10^{-10}C^2/Nm^2)$	3.6
$\epsilon_{12}(\times 10^{-10}C^2/Nm^2)$	3.4

The crack is meshed with 10 discontinuous quadratic elements, being the ones at the tip quarter-point ones. Figure 4.14 shows, for the normalized mode I SIF, the good agreement between the obtained results for a quasi-piezoelectric material and Shindo and Ozawa's solution.

The ESIF for a L-wave impinging a straight crack in a $BaTiO_3 - CoFe_2O_4$ composite with a V_f=0.5 domain are shown in figures 4.15 and 4.16,

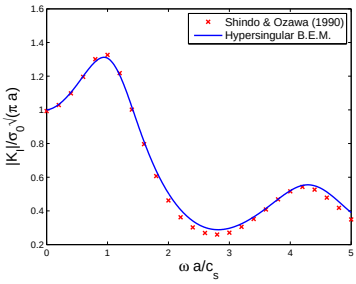

Figure 4.14: Comparison with Shindo's results

where it can be noticed that the evolution of K_I and K_{IV} with the frequency has a similar behavior to the one observed in piezoelectric materials (Sáez et al., 2006). Note that K_{II} has not been included because it is null for all frequencies.

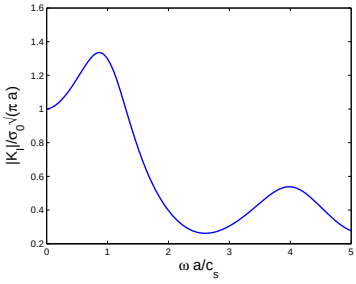

Figure 4.15: Normalized K_I for a Griffith crack when a L-wave is impinging.

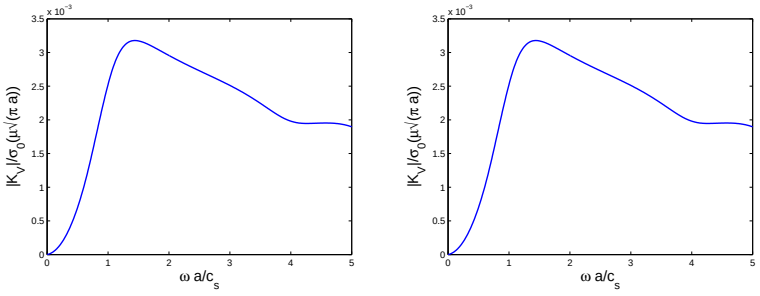

Figure 4.16: Normalized K_{IV} (left) and K_V (right) for a Griffith crack when a L-wave is impinging.

4.3.3 Branched crack in an infinite domain

Scattering of L-waves by a branched crack is now considered. In figure 4.17, it is depicted the geometry and loads of the problem which will be solved for several branch angles θ. Note that the wave impinges first on the main crack, which is meshed with 10 discontinuous quadratic elements, whilst 5 elements are used to mesh the crack branch. Elements at both crack tips are quarter-point elements. In figure 4.18, the normalized ESIF at the branch tip are plotted against the dimensionless frequency.

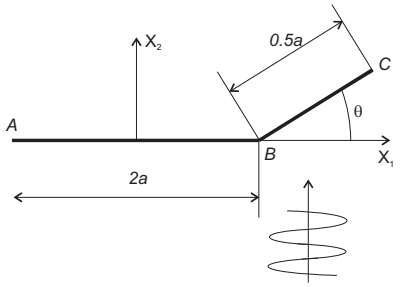

Figure 4.17: L-wave impinging on a branched crack

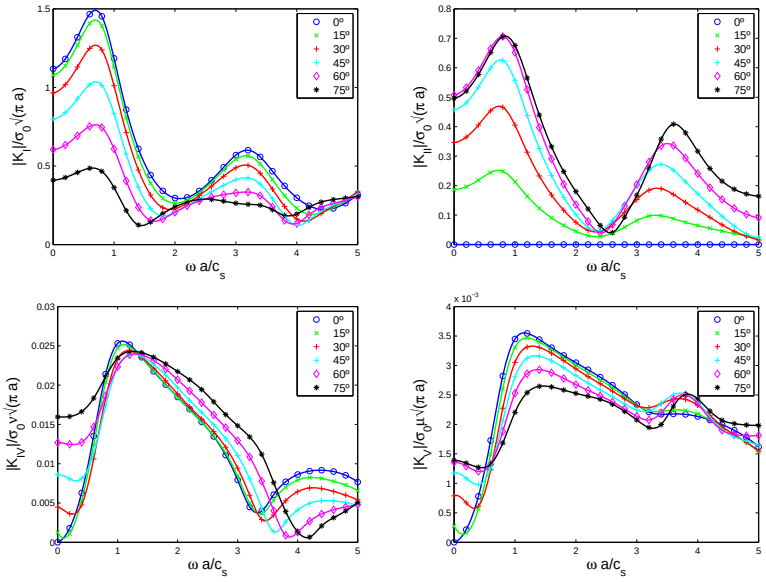

Figure 4.18: L-wave scattering by a branched crack: ESIF at branch tip vs. frequency for different branch angles

The influence of the frequency of the incident wave motion is clear from the figures, with peak values of the mode I SIF around $\omega a/c_S = 0.8$, around 1.0 for the EDIF and 1.1 for the MIIF. Again, fluctuations in the dynamic SIF and the EDIF of the magnetoelectroelastic composite exhibit a similar behavior to the previously observed for piezoelectric materials by Sáez et al. (2006). As expected, larger peak values of K_I are obtained with decreasing values of the angle branch β, while the opposite can be stated about K_{II}. For low frequencies, both K_{IV} and K_V decrease when the branch angle is increased, but that tendency changes more quickly in K_V. Moreover, peak values of the EDIF are similar for the different branch angles, while,

decreasing branch angles produce larger peak values of the MIIF.

4.3.4 Circular arch crack in an infinite domain

Scattering of L-waves by a circular arch crack is next considered. The geometry of the problem is shown in figure 4.19. Results are obtained for different values of the arch semi-angle α. The crack is meshed with 8 discontinuous quadratic curved elements with decreasing size towards the tip, plus 2 very small straight quarter-point elements at the tips with a small length of arch-length/30. The normalized field intensity factors at the crack tip are plotted against the dimensionless frequency in figure 4.20.

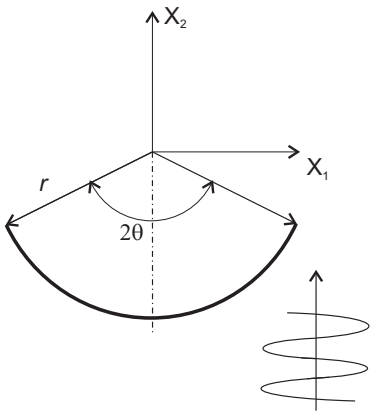

Figure 4.19: L-wave impinging on a circular arch crack

Due to the modification of the relative angle between the tangent at the crack tip and the incident motion, as it could be expected, normalized K_I decreases as the arch-angle α is increased, whilst mode-II SIF presents the opposite tendency.

To better illustrate the dynamic coupling effects, maps of the ampli-

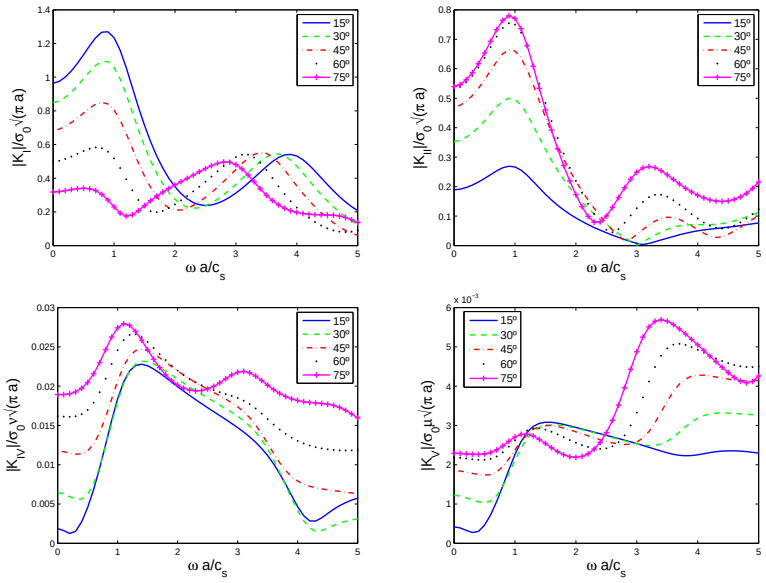

Figure 4.20: L-wave scattering by circular arch crack: ESIF at tip vs. frequency for different arch angles

tudes of the vertical displacement (u_2/u_0), the electric potential (ϕ/ϕ_0) and the magnetic potential (φ/φ_0) are presented (figures 4.21-4.22) for an arch semi-angle $\alpha = 45$. Three different frequencies ($\omega a/c_S = 0.3$, 0.8, 1.5) are considered, being them, respectively, smaller than the resonance frequency, around that value, and larger than it. Those plots show amplitudes for total fields, i.e., incident plus scattered fields due to the presence of the crack.

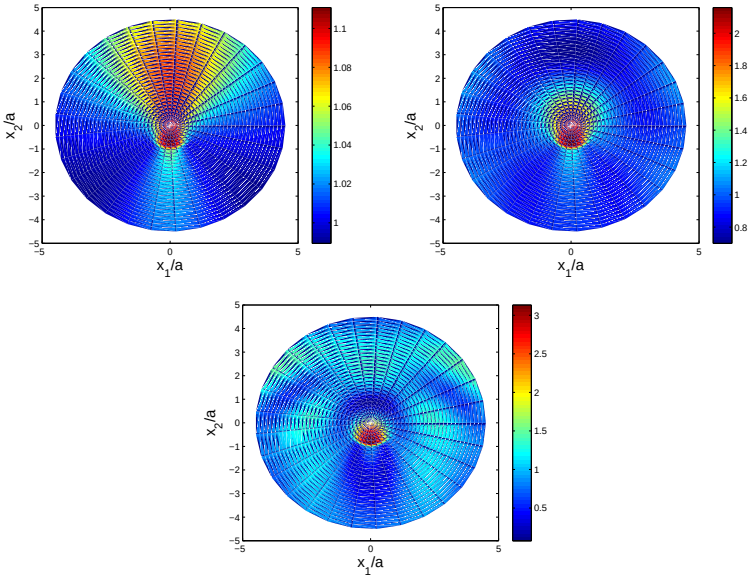

Figure 4.21: L-wave scattering by circular arch crack: vertical displacements at frequencies $\omega a/c_S$ 0.3 (top left), 0.8 (top right), 1.5 (bottom)

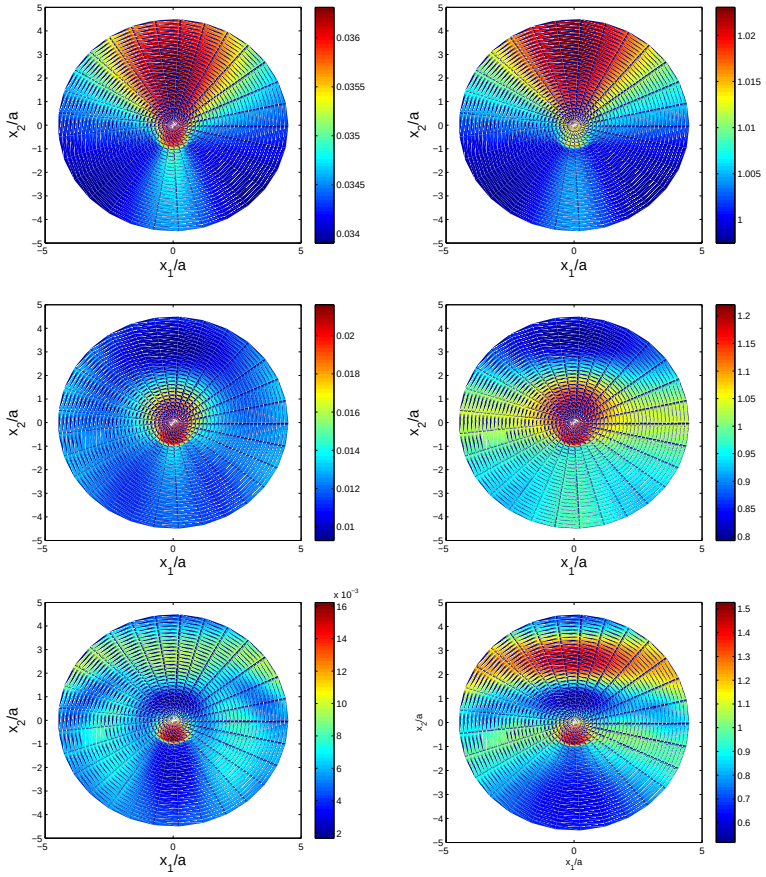

Figure 4.22: L-wave scattering by circular arch crack: electric (left) and magnetic (right) potentials at frequencies $\omega a/c_S$ 0.3 (top), 0.8 (center), 1.5 (bottom)

4.3.5 Two cracks interaction in an infinite domain

In this section, interaction between two cracks in an infinite domain when a L-wave impinges on them is studied. The geometry of the problem is illustrated in figure 4.23, and several different cases will be analyzed depending on the relative position of the cracks.

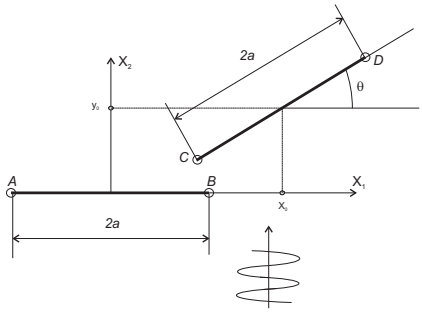

Figure 4.23: L-wave impinging on two interacting cracks

Parallel cracks in an infinite domain

The case of two parallel cracks is now analyzed. Three different distances between the cracks have been considered, namely $a/2$, a and $2a$, a being the half crack-length. The geometry of the problem is illustrated in figure 4.23 with $\theta = 0$, $x_0 = 0$ and $y_0 = a/2,\ a,\ 2a$.

Figure 4.24 shows the normalized ESIF, versus the dimensionless frequency $\omega a/c_S$. Results are given for the crack first hit by the incident L-wave (at tip A). In order to illustrate the effects of crack interactions, in the figures are included the results for a single crack. Such interactions increase as the distance between the cracks decreases. The influence of the frequency of the incident wave motion is clear from the figures, with peak

values of the field intensity factors around $\omega a/c_S = 1$.

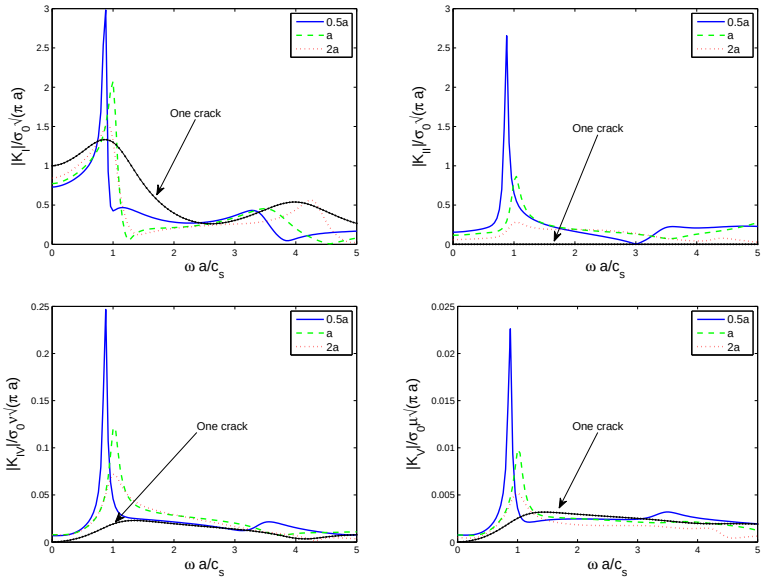

Figure 4.24: L-wave scattering by two parallel cracks: ESIF at crack tip A (figure 4.23) vs. frequency

Results for the upper crack (tip C) are included in figure 4.25. In this case the interaction effects are more significant due to the interaction among the incident field and the one scattered by the first crack. In fact, those interaction effects remain substantial at separations between cracks as large as two crack-lengths.

Figures 4.26-4.28 show images of the amplitudes of the total fields, i.e., incident plus scattered fields, due to the presence of the two cracks. Results are plotted for frequencies equal to $\omega a/c_S = 0.75, 1, 1.25$, where it is illustrated clearly the dynamic interaction effects on the distribution of

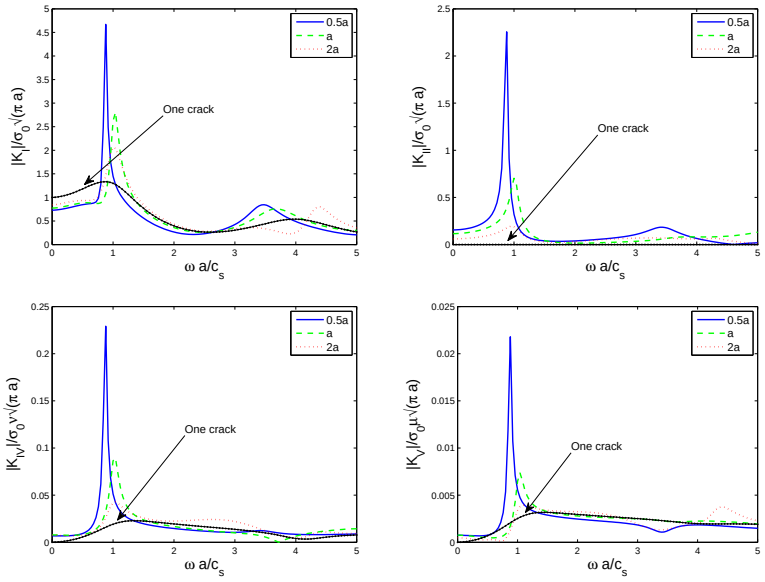

Figure 4.25: L-wave scattering by two parallel cracks: ESIF at crack tip C (figure 4.23) vs. frequency

the displacements (figure 4.26), the electric (figure 4.27) and the magnetic (figure 4.28) potentials in the analyzed magnetoelectroelastic solid.

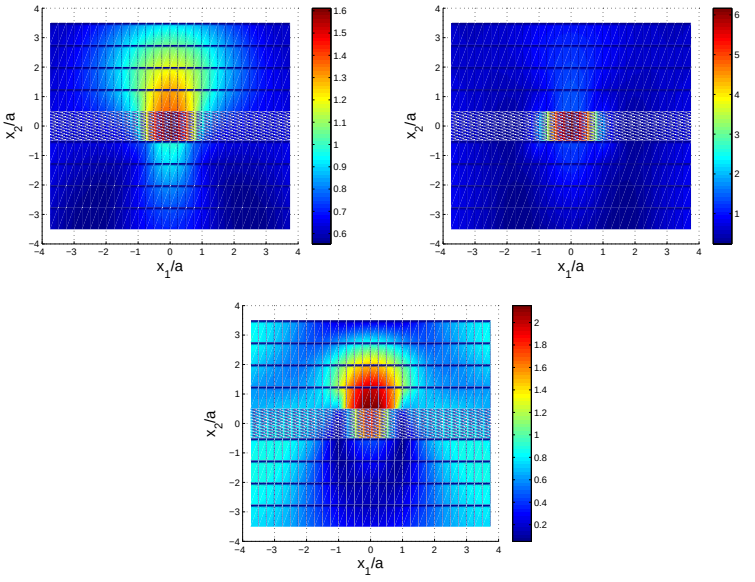

Figure 4.26: Parallel cracks ($y_0 = a$, figure 4.23): Amplitude of the total displacement field in x_2 direction at frequency values $\omega a/c_S$ equal to 0.75 (top left), 1 (to right), 1.25 (bottom)

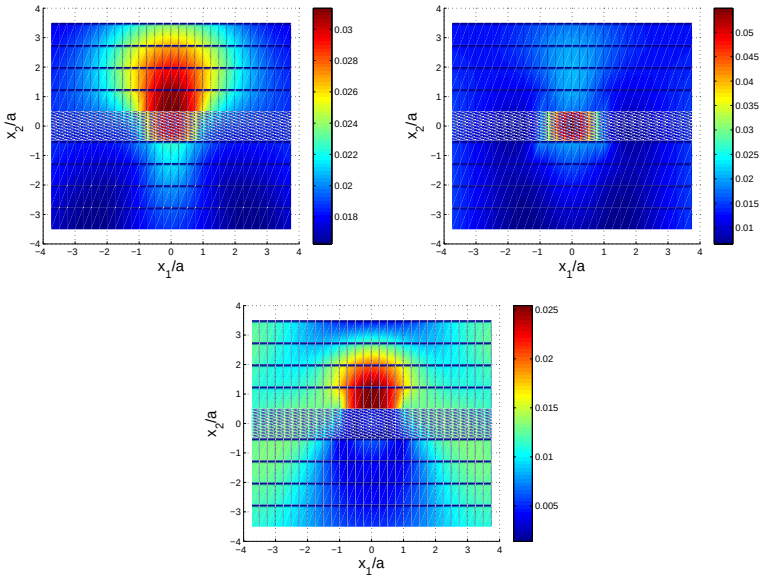

Figure 4.27: Parallel cracks ($y_0 = a$, figure 4.23): Amplitude of the total electric potential field at frequency values $\omega a/c_S$ equal to 0.75 (top left), 1 (to right), 1.25 (bottom)

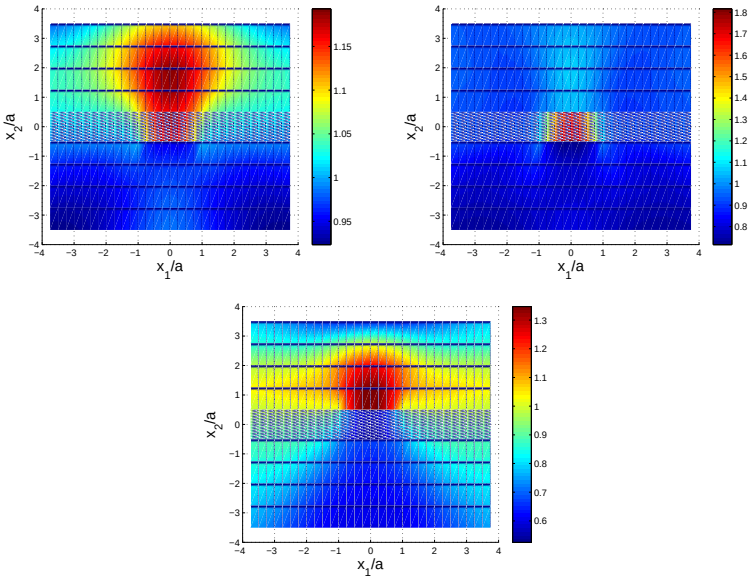

Figure 4.28: Parallel cracks ($y_0 = a$, figure 4.23): Amplitude of the total magnetic potential field at frequency values $\omega a/c_S$ equal to 0.75 (top left), 1 (to right), 1.25 (bottom)

Two collinear cracks

Wave scattering caused by to collinear cracks is next considered. The geometry of the problem is shown in figure 4.23 with $\theta = 0$, $y_0 = 0$ and $x_0 = 2a + a/2$, a, $2a$; a being the half crack-length, i.e., three different distances between the inner crack tips (tips B and C) have been studied: $a/2$, a and $2a$.

The mode-I SIF is given in figure 4.29 (top left) versus the frequency for the inner crack tip (tip B). In this case, the interaction effects are small and

only produce a shift in the frequency of the peak value for crack separations below the crack-length. However, due to the magnetoelectroelastic coupling, such interaction effects are more significant in the case of the EDIF (figure 4.29 -top right) and the MIIF (figure 4.29 -bottom).

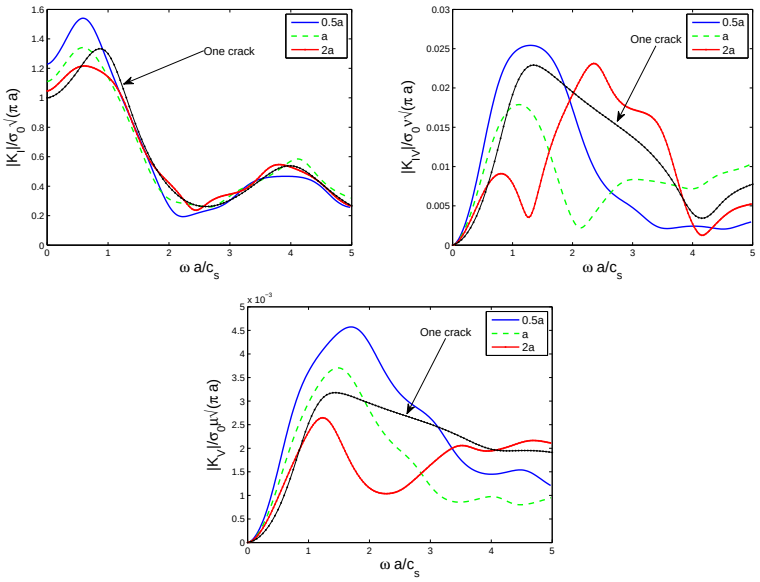

Figure 4.29: L-wave scattering by two collinear cracks: ESIF at crack tip B (figure 4.23) vs. frequency

Two cracks with an inclination angle

The case of two cracks at an angle will be the last frequency-domain problem solved and presented in this work. The geometry of the problem is shown in figure 4.23 with $\theta = \pi/4$, $x_0 = a/\sqrt{2}$ and $y_0 = a/\sqrt{2}+ a/2$, a, $2a$.

The mode-I SIF is plotted against the frequency in figure 4.30 (top left)

for the lower crack tip B and in figure 4.30 (top right) for the upper crack tip C. At tip B the interaction effects are small in the low frequency range. However, at tip C crack-shielding is observed due to the presence of the lower crack. Mode-II SIF appears as a consequence of crack interaction, as shown in figures 4.30 (bottom left) and 4.30 (bottom right) for crack tips B and C, respectively.

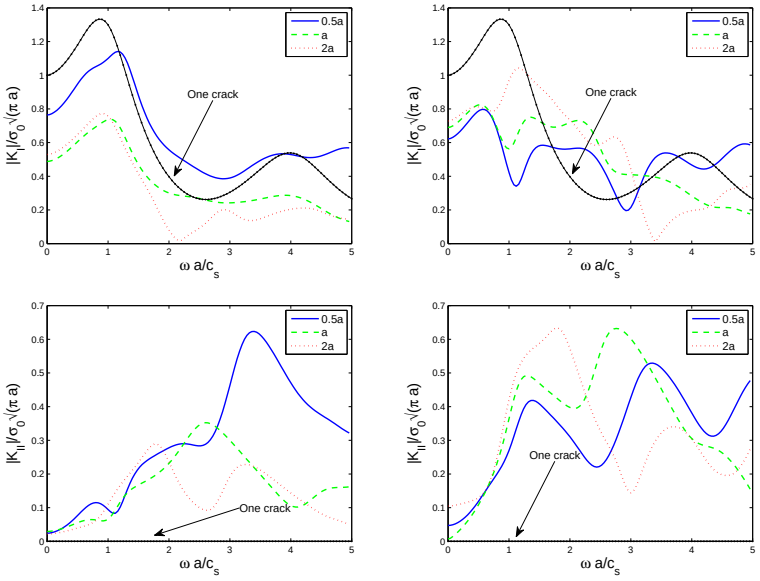

Figure 4.30: L-wave scattering by two cracks at an angle: K_I and K_{II} at tip B (top line) and tip C (bottom line) vs. frequency (figure 4.23)

In figure 4.31 the EDIF and MIIF behaviors versus the frequency at crack tips B and C are illustrated. Larger and shifted values of both the EDIF and the MIIF are observed for the upper crack, as compared with the one crack case. This phenomenon may be caused by the magnetoelectroe-

lastic coupling.

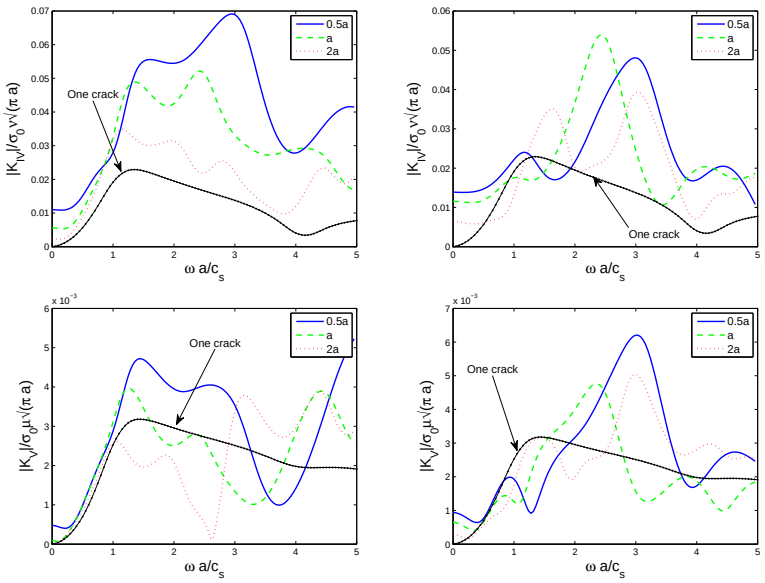

Figure 4.31: L-wave scattering by two cracks at an angle: K_{IV} and K_V at tip B (top line) and tip C (bottom line) vs. frequency (figure 4.23)

4.4 Time-domain results

In this section, transient dynamic analysis of two-dimensional homogeneous and linear magnetoelectroelastic cracked solids will be carried out by solving several problems in either finite or infinite domain under impact loading.

In all the problems solved a $BaTiO_3 - CoFe_2O_4$ composite with a V_f=0.5 is considered and, for the convenience of the presentation, the following normalized dynamic EDIF and MIIF are introduced

$$K_{IV}^{*} = \frac{e_{22}}{\varepsilon_{22}} \frac{K_{IV}}{K_I^{st}} \quad ; \quad K_V^{*} = \frac{h_{22}}{\gamma_{22}} \frac{K_V}{K_I^{st}} \tag{4.12}$$

where $K_I^{st} = \sigma_0 \sqrt{(\pi a)}$.

Moreover, to measure the intensity of the electromagnetic impacts, the following loading parameters are defined

$$\lambda = \frac{e_{22}}{\varepsilon_{22}} \frac{D_2}{\sigma_{22}} \quad ; \quad \Lambda = \frac{h_{22}}{\gamma_{22}} \frac{B_2}{\sigma_{22}} \tag{4.13}$$

Previous works for other materials, such as Dominguez (1993) for homogeneous isotropic solids, establish that, to ensure the stability of the time-stepping scheme of a time domain formulation, the spatial size of the elements and the time step can not be chosen independently, but they should satisfy the following relation

$$\eta = \frac{c_{max} \Delta t}{l_e} \approx 1 \tag{4.14}$$

where c_{max} is the maximum of the plane wave phase velocities, Δt is the time step and l_e is the element length.

Choosing too small time steps will increase the computational cost, while choosing too large ones will not permit a proper representation of quick changes in the exact solution (Dominguez, 1993).

It should be remarked that formulations based on Lubich's quadratures to compute the convolution integrals in the time domain BEM are extremely stable and the spatial and temporal discretizations are rather independent, as compared to formulations based on direct integration in the time domain.

4.4.1 Straight crack in an infinite domain

In order to validate the proposed time-domain formulation, a straight crack in an infinite domain subjected to an impact tensile mechanical loading

of the form $\sigma_{22}(t) = \sigma_0 \cdot H(t)$, where H(t) is the Heaviside step function, is analyzed. Three different time steps have been considered: $a/(15 \cdot c_S)$, $a/(30 \cdot c_S)$ and $a/(60 \cdot c_S)$ and ten equal quadratic elements have been used. The obtained results are compared with those presented by Zhong et al. (2009) by the application of the Stehfest's method (see e.g. Stehfest, 1996) to derive the Laplace transform, and shown in figure 4.32, where it can be noticed that both results reach the stationary value at a similar instant of time, but they are very different in the transient period since the results presented herein show a higher peak.

Stehfest's inversion algorithm establishes that a time-dependent function *f(t)* can be approximated by

$$f(t) = \frac{\ln 2}{t} \sum_{n=1}^{N} \nu_n \widehat{f}(n \ln 2/t) \tag{4.15}$$

where $\widehat{f}(s)$ is the laplace transform of *f(t)* and

$$\nu_n = (-1)^{n+N/2} \cdot \sum_{k=(n+1)/2}^{min\{n,N/2\}} \frac{(2k)! k^{N/2}}{(N/2-k)!k!(k-1)!(n-k)!(2k-n)!} \tag{4.16}$$

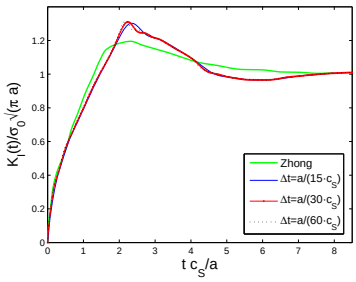

Figure 4.32: Comparison of the normalized dynamic K_I factor for a Griffith crack with the results obtained by Zhong et al.

Stehfest suggested in his works to use, at least, N=10 while Zhong uses only N=3. This is the cause of an excessively high softening of the curve in the transient period. As a matter of fact, a higher value of the peak should be expected, as works by García-Sánchez and co-workers for anisotropic and piezoelectric solids reveal (see, e.g., García-Sánchez and Zhang, 2007b; García-Sánchez et al., 2008a). Thus, it can be concluded that the model presented herein provides correct results.

As it has been said above, three different time steps have been considered, obtaining in all cases good and stable results, even for the minimum η considered here which value is $\eta \approx 0.167$.

Let us now consider different combinations of loadings defined by the interaction of an impact tensile mechanical loading ($\sigma_{22}(t) = \sigma_0 \cdot H(t)$), an impact electrical loading ($D_2(t) = D_0 \cdot H(t)$) and/or an impact mechanical loading ($B_2(t) = B_0 \cdot H(t)$). In figure 4.33 the normalized mode-I SIF is shown. As expected for all combinations of loadings, defined by equations (4.13), the value of that parameter tends to one, due to the fact that mechanical SIF for Griffith cracks are independent of the presence of electric and magnetic loadings. Moreover, as it has been said in this work, positive electric and magnetic loads make the crack open wider and this effect, although is not noticed in the permanent value, is shown in the transient period as a higher peak.

In figure 4.34, the mode-I mechanical energy release rate is plotted. The values have been normalized with the corresponding one to a crack subjected to a static mechanical loading. Positive electromagnetic loadings make higher both the peaks and the permanent values.

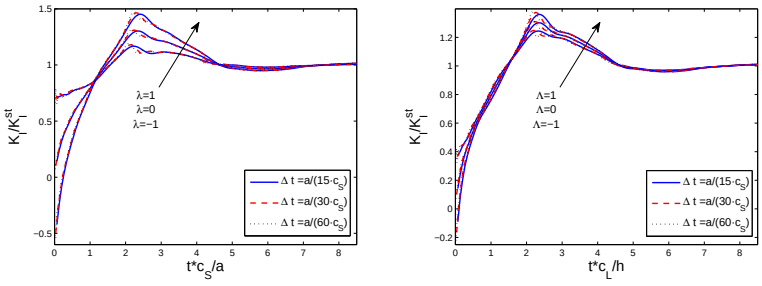

Figure 4.33: Normalized dynamic K_I versus the dimensionless time for a Griffith crack in a magnetoelectroelastic solid subjected to different impact loading combinations

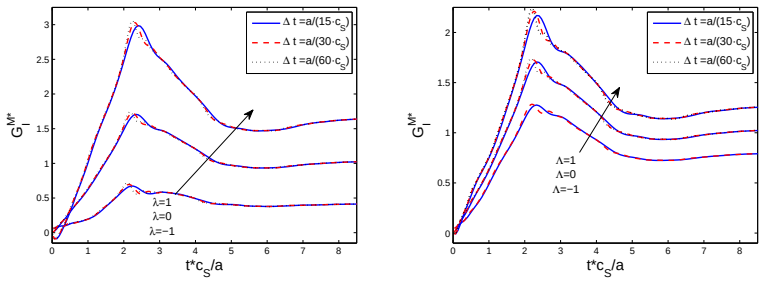

Figure 4.34: Normalized dynamic mode-I energy release rate versus the dimensionless time for a Griffith crack in a magnetoelectroelastic solid subjected to different impact loading combinations

4.4.2 Central crack in a magnetoelectroelastic plate

A center crack of length *2a* in an homogeneous linear magnetoelectroelastic plate as the one shown in figure 4.35 is now considered. The geometry of the cracked plate is described by h=20mm, w=20mm and a=2.4mm, and

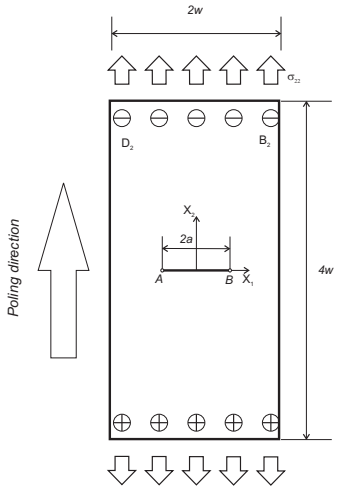

Figure 4.35: Straight crack in a magnetoelectroelastic plate.

it is subjected to different loading combinations defined by the interaction of an impact tensile mechanical loading ($\sigma_{22}(t) = \sigma_0 \cdot H(t)$), an impact electrical loading ($D_2(t) = D_0 \cdot H(t)$) and/or an impact magnetic loading ($B_2(t) = B_0 \cdot H(t)$). The external boundary is meshed with 24 quadratic elements, while ten equal quadratic discontinuous elements are used in the crack meshing.

Normalized ESIF and loading parameters as the ones defined in (4.12-4.13) are used in the representation of this problem results. In figure 4.36 the normalized mode-I SIF is plotted for several loading combinations versus the time, which is normalized with the longitudinal wave velocity and the semilength of the plate. This normalization implies that the mechanical wave impinges on the crack at the normalized time $t^* = 1$. Thus before that instant of time, if only a mechanical loading is applied, $K_I \cong 0$. However,

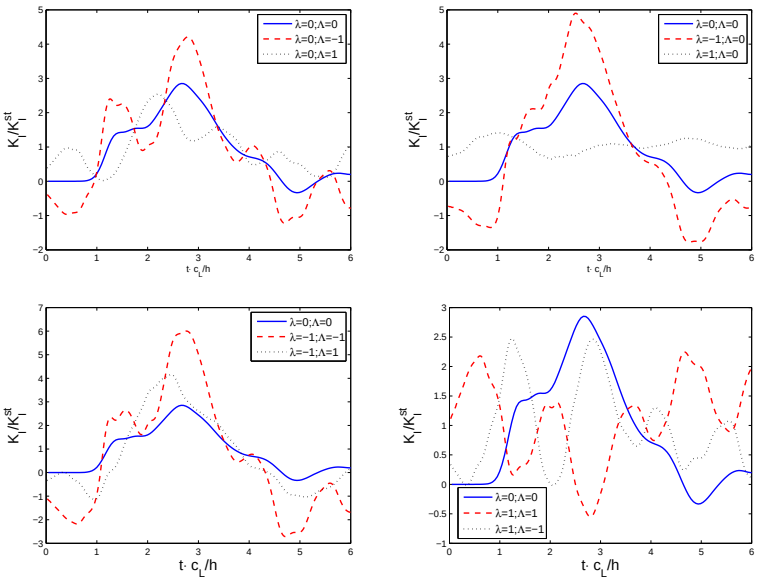

Figure 4.36: Normalized dynamic K_I versus the dimensionless time in a magnetoelectroelastic cracked plate subjected to different impact loading combinations

if either an electric or a magnetic loading is also applied, the variation on the mode-I SIF happens since $t^* = 0$, due to the quasi-electrostatic assumption for the electromagnetic fields. In all cases, it can be noticed that the maximum values of the normalized mode-I dynamic stress intensity factor are reduced with increasing electric and magnetic loading parameters λ and Λ, according to the poling direction indicated in figure 4.35.

In figures 4.37 and 4.38, normalized K_{IV} and K_V are plotted versus dimensionless time. Due to the quasi electrostatic assumption of the electromagnetic fields , almost constants values for those fracture parameters

are obtained when electric or magnetic loadings, respectively, are applied. Moreover, an almost negligible influence of the electric and magnetic loadings is found in MIIF and EDIF, respectively, as seen in figures 4.37 (top left) and 4.37 (top right).

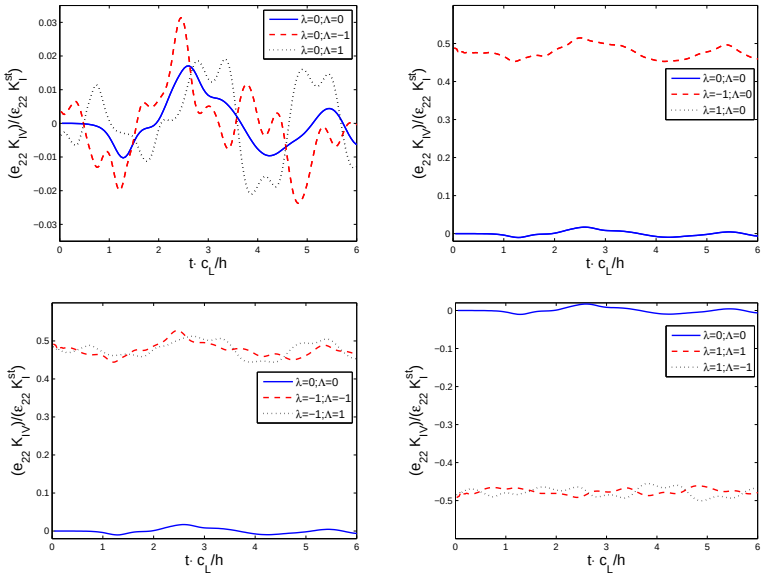

Figure 4.37: Normalized dynamic K_{IV} versus the dimensionless time in a magnetoelectroelastic cracked plate subjected to different impact loading combinations

To better illustrate the transient effects, maps of the vertical displacement (u_2), and the electric and magnetic potentials (ϕ and φ) are also included in this work for three different combinations of loads (defined, respectively, by the pairs $\lambda = \Lambda = 0$, $\lambda = 1; \Lambda = 0$ and $\lambda = 0; \Lambda = 1$) and two instants of time, smaller and bigger than one,respectively: $t^* = 0.4275$ and

$t^* = 1.52$. When $t^* \leq 1$ and only mechanical loading is applied, vertical displacements are negligible in almost all the plate.

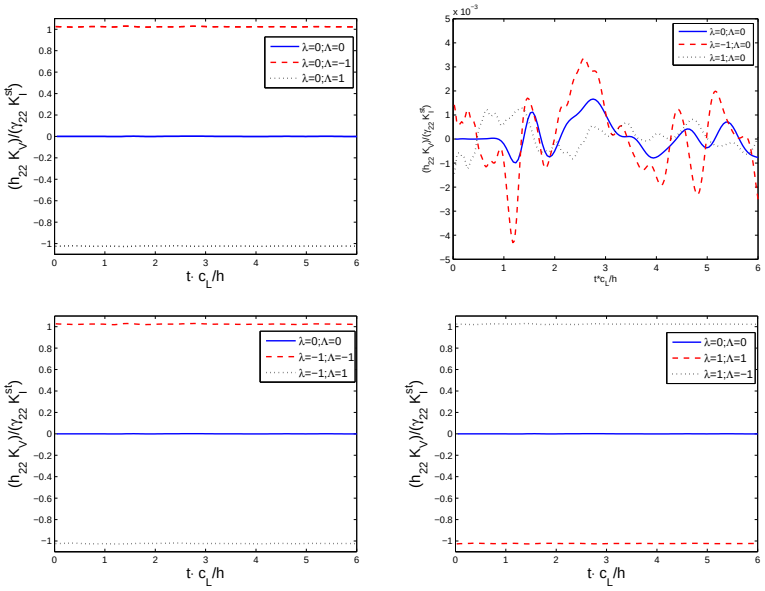

Figure 4.38: Normalized dynamic K_V versus the dimensionless time in a magnetoelectroelastic cracked plate subjected to different impact loading combinations

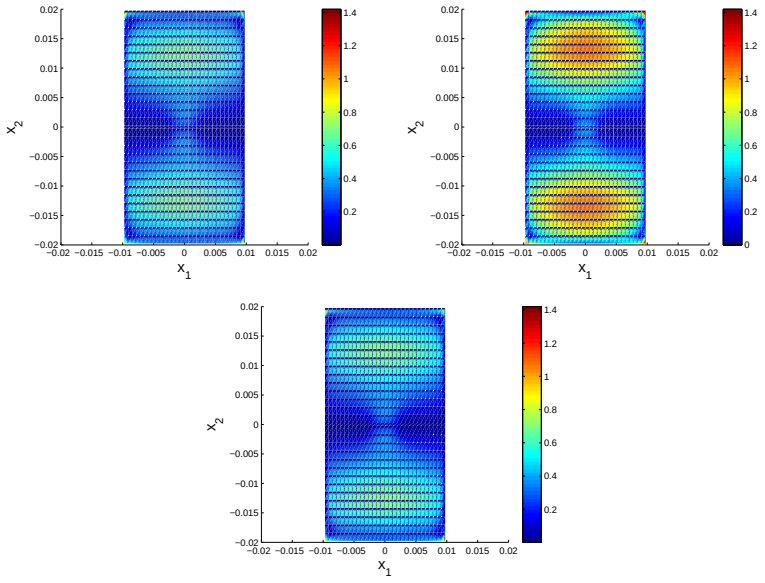

Figure 4.39: Absolute value of the normalized vertical displacement for $t^* = 0.4275$ when $\lambda = 0; \Lambda = 0$ (top left), $\lambda = 1; \Lambda = 0$ (top right) and $\lambda = 0; \Lambda = 1$ (bottom)

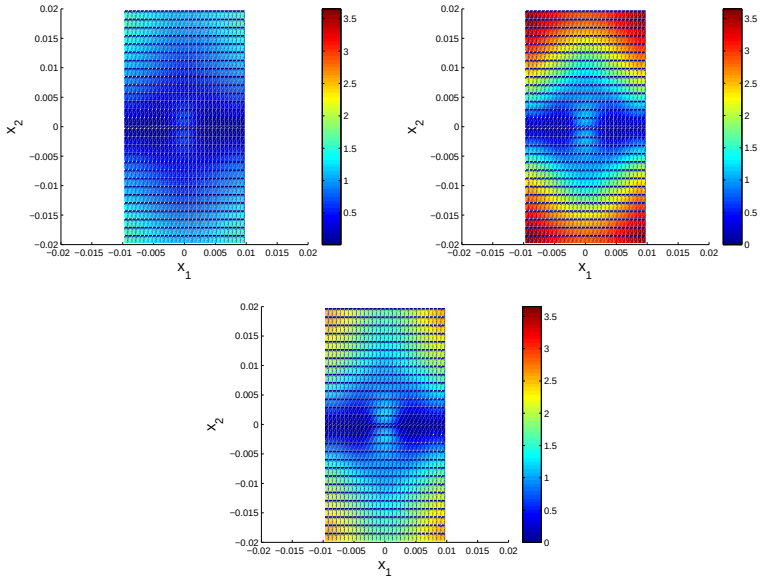

Figure 4.40: Absolute value of the normalized vertical displacement for $t^* = 1.52$ when $\lambda = 0; \Lambda = 0$ (top left), $\lambda = 1; \Lambda = 0$ (top right) and $\lambda = 0; \Lambda = 1$ (bottom)

4.4.3 Slanted edge crack in a magnetoelectroelastic plate

Let us consider now a slanted edge crack of length a in a homogeneous and linear magnetoelectroelastic plate as the one shown in figure 4.41. The crack is inclined 45^o respect to the horizontal, and the geometry of the plate is given by h=22mm, w=32mm, c=6mm and a=22.63mm.

The mesh is performed with 24 quadratic elements for the external boundary, and 4 discontinuous quadratic elements for the crack; the time step adopted in the simulations is given by $0.15 \cdot a/c_L$. In figures 4.42

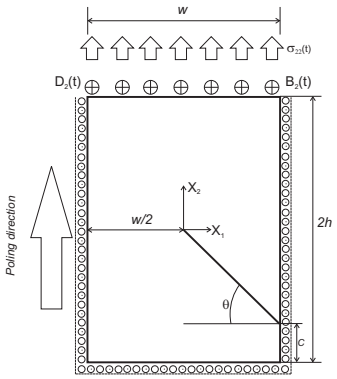

Figure 4.41: Slanted edge crack in a magnetoelectroelastic plate subjected to impact electromagnetomechanic loadings

and 4.43, mode-I and mode-II stress intensity factors are plotted for different combinations of loads. It can be noticed that, when no combination of electromagnetic loadings are applied (*top left* and *top right* figures), there exist two different time ranges in which those parameters are independent of the electric and magnetic impacts (when applied). This effect disappears when both electric and magnetic loadings act at the same time.

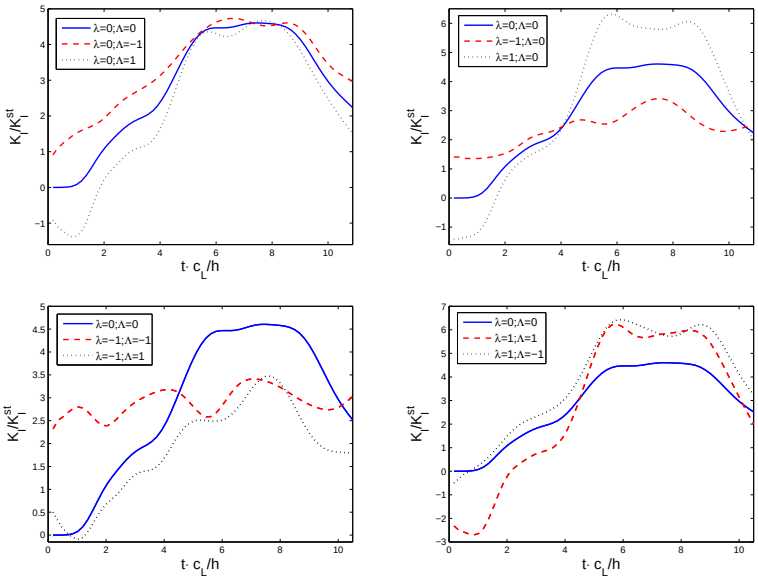

Figure 4.42: Normalized dynamic K_I versus the dimensionless time in a magnetoelectroelastic cracked plate containing an slanted edge crack subjected to different impact loading combinations

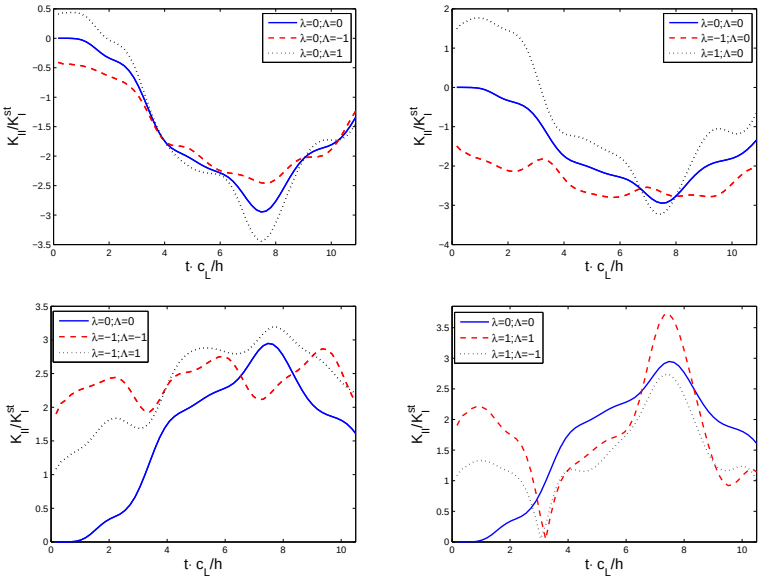

Figure 4.43: Normalized dynamic K_{II} versus the dimensionless time in a magnetoelectroelastic cracked plate containing an slanted edge crack subjected to different impact loading combinations

Chapter 5

Extended Finite Element formulation for the analysis of cracked magnetoelectroelastic solids

5.1 Introduction

In this chapter, a different numerical technique for the study of static fracture mechanics in magnetoelectroelastic materials is presented.

The analysis of cracked media with the Finite Element Method (FEM) present a big inconvenient, since the crack must merge with the mesh. This fact provokes the necessity of remeshing when crack growth problems are studied. Additionally, mesh refinement and/or singular elements such as quarter-point elements are also necessary near the crack-tip to capture the stress singularity.

To circumvent these difficulties, the eXtended Finite Element Method (X-FEM), first presented by Belytschko and Black (1999) and Möes et al. (1999), is a powerful alternative in computational fracture, which have been successfully applied to solve crack problems in materials with different behavior laws (see, e.g., works by Möes et al., 1999 in isotropic media, Sukumar et al., 2004 in bimaterials, Asadpoure and Mohammadi, 2007 in orthotropic materials and Béchet et al., 2009 in piezoelectric solids). To this end, additional (*enrichment*) functions are added to the classical finite element approximation through the framework of partition of unity (Babuska and Melenk, 1997). In other words, in certain nodes of the mesh, new degrees of freedom are added in order to modelize the discontinuity existing due to the presence of the crack. The crack interior is represented by a discontinuous (Heaviside) function and the crack-tip is modeled by the asymptotic crack-tip functions.

In this work, we present a X-FEM approach for fracture analysis in plane anisotropic magnetoelectroelastic materials. For this purpose, new crack-tip enrichment functions will be derived and, in order to validate the proposed method, some problems solved comparing the results with those obtained by the BEM formulation previously introduced.

5.2 X-FEM formulation

5.2.1 Crack modelling and selection of enriched nodes

Let us consider an arbitrary cracked domain, discretized in elements so that the nodal set is $\mathcal{N}$. Then, the displacement of a point $\mathbf{x}$ belonging to the domain considered can be determined by (Möes et al., 1999)

$$\mathbf{u}(\mathbf{x}) = \sum_{i \in \mathcal{N}} N_i(\mathbf{x})\mathbf{u}_i + \sum_{j \in \mathcal{N}^{\mathcal{H}}} N_j(\mathbf{x})H(\mathbf{x})\boldsymbol{a}_j + \sum_{k \in \mathcal{N}^{\mathcal{CT}}} N_k(\mathbf{x}) \sum_{\alpha} F_\alpha(\mathbf{x})\boldsymbol{b}_k^\alpha \quad (5.1)$$

where N_i is the shape function associated to the node i, $\mathbf{u}_i$ is the vector of the traditional nodal degrees of freedom defined in a finite elements discretization while $\mathbf{a}_j$ and $\mathbf{b}_k^l$ are the added set of degrees of freedom in those elements which contain the crack. $H(\mathbf{x})$ is the generalized Heaviside function, that simulates the displacement discontinuity on both sides of the crack faces, and F_α are the crack tip enrichment functions. In a finite element mesh, as seen in figure 5.1, the set of nodes which have to be enriched with Heaviside functions ($\mathcal{N}^H$) are marked with a solid circle, while the set of nodes which must be enriched with crack tip enrichment functions ($\mathcal{N}^{CT}$) are marked with a square.

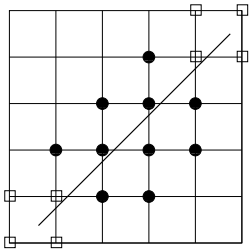

Figure 5.1: Node selection for enrichment

In a magnetoelectroelatic solid, the variables which appear in equation (5.1) are defined in an extended way, so $\mathbf{u}_i$ and $\mathbf{a}_i$ are four components vectors and $\mathbf{b}_i$ is a 32 components vector, as it will be exposed in a later section.

5.2.2 Weak formulation and discrete equations

Let us consider an arbitrary cracked domain Ω which contains a boundary Γ_t where the extended tractions are prescribed and in which impermeable crack faces condition is considered (extended traction-free crack faces). Let $\widetilde{\mathbf{u}}$ be the mechanical displacement and $\widetilde{\boldsymbol{\sigma}}$ the mechanical stress tensor, while $\mathbf{u}$ and $\boldsymbol{\sigma}$ are, respectively, the extended displacement vector and the extended stress tensor. The weak form (principle of virtual work) for a continuous problem in a magnetoelectroelastic solid is given by

$$\begin{aligned}
&\int_{\Omega} \widetilde{\boldsymbol{\sigma}} : \delta\widetilde{\boldsymbol{\varepsilon}}\, d\Omega - \int_{\Omega} \mathbf{D} : \delta\mathbf{E}\, d\Omega - \int_{\Omega} \mathbf{B} : \delta\mathbf{H}\, d\Omega = \int_{\Gamma_t} \overline{\mathbf{p}}^{mech} \cdot \delta\widetilde{\mathbf{u}} d\Gamma \\
&- \int_{\Gamma_t} \overline{\mathbf{p}}^{e} \cdot \delta\phi\, d\Gamma - \int_{\Gamma_t} \overline{\mathbf{p}}^{m} \cdot \delta\varphi\, d\Gamma + \int_{\Omega} \mathbf{f}^{mech} \cdot \delta\widetilde{\mathbf{u}}\, d\Omega \\
&- \int_{\Omega} \mathbf{f}^{e} \cdot \delta\phi\, d\Omega - \int_{\Omega} \mathbf{f}^{m} \cdot \delta\varphi\, d\Omega. \qquad (5.2)
\end{aligned}$$

where the superscripts *mech*, *e*, and *m* denote, respectively mechanical, electrical and magnetic tractions or volume forces.

The use of the generalized notation introduced in chapter 2 allows expressing the weak form in an elastic-like way

$$\int_{\Omega} \boldsymbol{\sigma} : \delta\boldsymbol{\varepsilon}\, d\Omega = \int_{\Gamma_t} \overline{\mathbf{p}} \cdot \delta\mathbf{u} + d\Gamma + \int_{\Omega} \mathbf{f} \cdot \delta\mathbf{u}\, d\Omega \qquad (5.3)$$

where : and $\cdot$ denotes, respectively, tensorial and scalar products, $\mathbf{f}$ is the extended force vector per unit volume and $\overline{\mathbf{p}}$ are the prescribed extended tractions. In particular, $\overline{\mathbf{p}}^{mech}$ are the mechanical tractions and $\overline{\mathbf{p}}^{e}$ and $\overline{\mathbf{p}}^{m}$ are, respectively, their electric and magnetic counterparts

After the appropriate discretizations of the governing equations, the

following magnetoelectroelastic finite element equations can be derived

$$\mathbf{k}_{\widetilde{u}\widetilde{u}}\widetilde{\mathbf{u}} + \mathbf{k}_{\widetilde{u}\phi}\boldsymbol{\phi} + \mathbf{k}_{\widetilde{u}\varphi}\boldsymbol{\varphi} = \mathbf{f}^{mech} \tag{5.4a}$$

$$\mathbf{k}_{\phi\widetilde{u}}\widetilde{\mathbf{u}} - \mathbf{k}_{\phi\phi}\boldsymbol{\phi} - \mathbf{k}_{\phi\varphi}\boldsymbol{\varphi} = \mathbf{f}^{e} \tag{5.4b}$$

$$\mathbf{k}_{\varphi\widetilde{u}}\widetilde{\mathbf{u}} - \mathbf{k}_{\varphi\phi}\boldsymbol{\phi} - \mathbf{k}_{\varphi\varphi}\boldsymbol{\varphi} = \mathbf{f}^{m} \tag{5.4c}$$

which can be also expressed like a simply elastic problem by means of the generalized notation

$$\mathbf{k}^{elem}\mathbf{u}^{elem} = \mathbf{f}^{elem} \tag{5.5}$$

where

$$\mathbf{k}^{elem} = \int\limits_{\Omega^{elem}} \mathbf{G}^T\mathbf{C}\mathbf{G}d\Omega = \int\limits_{-1}^{+1}\int\limits_{-1}^{+1} \mathbf{G}^T(\xi,\eta)\mathbf{C}\mathbf{G}(\xi,\eta)|J|d\xi\, d\eta \tag{5.6}$$

where $\mathbf{G}$ is the matrix of shape function derivative.

The global stiffness matrix $\mathbf{K}$ is obtained by the assembly of all the elementary stiffness matrices, and can be obtained as follows

$$\mathbf{k}_{ij}^{elem} = \begin{bmatrix} \mathbf{k}_{ij}^{uu} & \mathbf{k}_{ij}^{ua} & \mathbf{k}_{ij}^{ub} \\ \mathbf{k}_{ij}^{au} & \mathbf{k}_{ij}^{aa} & \mathbf{k}_{ij}^{ab} \\ \mathbf{k}_{ij}^{bu} & \mathbf{k}_{ij}^{ba} & \mathbf{k}_{ij}^{bb} \end{bmatrix} \tag{5.7}$$

while the element contribution to the global element force vector, $\mathbf{f}$ is

$$\mathbf{f}_i^{elem} = \{\mathbf{f}_i^{u} \quad \mathbf{f}_i^{a} \quad \mathbf{f}_i^{b1} \quad \dots \quad \mathbf{f}_i^{b\alpha}\}^T \tag{5.8}$$

where, in equations (5.7-5.8), α is the number of crack tip enrichment functions (eight in magnetoelectroelastic solids), and the indexes u, a and b refer, respectively, to the extended displacement vectors and the extended new degrees of freedom vectors. The submatrices and vectors that appear in it can be calculated as

$$\mathbf{k}_{ij}^{rs} = \int_{\Omega_e} (\mathbf{B}_i^r)^T \mathbf{C} (\mathbf{B}_i^s)\, d\Omega \quad (r,s = u,a,b) \tag{5.9a}$$

$$\mathbf{f}_i^u = \int_{\partial\Omega_e} N_i \bar{\mathbf{t}} d\Gamma + \int_{\Omega_e} N_i \mathbf{f}\, d\Omega \tag{5.9b}$$

$$\mathbf{f}_i^a = \int_{\partial\Omega_e} N_i H \bar{\mathbf{t}} d\Gamma + \int_{\Omega_e} N_i H \mathbf{f}\, d\Omega \tag{5.9c}$$

$$\mathbf{f}_i^{b\alpha} = \int_{\partial\Omega_e} N_i F_\alpha \bar{\mathbf{t}} d\Gamma + \int_{\Omega_e} N_i F_\alpha \mathbf{f}\, d\Omega \quad (\alpha = 1,8) \tag{5.9d}$$

In equation (5.9) N_i is the standard finite element shape function defined at node i, and $\mathbf{G}_i^u$, $\mathbf{G}_i^a$ and $\mathbf{G}_i^b$ are the nodal matrices of shape function derivatives, which, for a magnetoelectroelastic material, are given by

$$\mathbf{G}_i^u = \begin{bmatrix} N_{i,x_1} & 0 & 0 & 0 \\ 0 & N_{i,x_2} & 0 & 0 \\ N_{i,x_2} & N_{i,x_1} & 0 & 0 \\ 0 & 0 & N_{i,x_1} & 0 \\ 0 & 0 & N_{i,x_2} & 0 \\ 0 & 0 & 0 & N_{i,x_1} \\ 0 & 0 & 0 & N_{i,x_2} \end{bmatrix} \tag{5.10}$$

$$\mathbf{G}_i^a = \begin{bmatrix} (N_iH)_{,x_1} & 0 & 0 & 0 \\ 0 & (N_iH)_{,x_2} & 0 & 0 \\ (N_iH)_{,x_2} & (N_iH)_{,x_1} & 0 & 0 \\ 0 & 0 & (N_iH)_{,x_1} & 0 \\ 0 & 0 & (N_iH)_{,x_2} & 0 \\ 0 & 0 & 0 & (N_iH)_{,x_1} \\ 0 & 0 & 0 & (N_iH)_{,x_2} \end{bmatrix} \tag{5.11}$$

$$\mathbf{G}_i^b = \left[\begin{array}{cccccccc} \mathbf{G}_i^{b1} & \mathbf{G}_i^{b2} & \mathbf{G}_i^{b3} & \mathbf{G}_i^{b4} & \mathbf{G}_i^{b5} & \mathbf{G}_i^{b6} & \mathbf{G}_i^{b7} & \mathbf{G}_i^{b8} \end{array} \right] \tag{5.12a}$$

$$\mathbf{G}_i^{b\alpha} = \left[\begin{array}{cccc} (N_i F_\alpha)_{,x_1} & 0 & 0 & 0 \\ 0 & (N_i F_\alpha)_{,x_2} & 0 & 0 \\ (N_i F_\alpha)_{,x_2} & (N_i F_\alpha)_{,x_1} & 0 & 0 \\ 0 & 0 & (N_i F_\alpha)_{,x_1} & 0 \\ 0 & 0 & (N_i F_\alpha)_{,x_2} & 0 \\ 0 & 0 & 0 & (N_i F_\alpha)_{,x_1} \\ 0 & 0 & 0 & (N_i F_\alpha)_{,x_2} \end{array} \right] \tag{5.12b}$$

where the *comma* denotes spatial derivation.

5.2.3 Enrichment functions

The asymptotic displacement fields around the crack tip in an unbounded magnetoelectroelastic domain were presented in chapter 2. From them, a set of elementary functions that span the asymptotic fields can be obtained, for any orientation of the crack and loading combination.

While for isotropic and piezoelectric materials, only four or six functions, respectively, are necessary to describe all the possible generalized displacement states around the crack tip, for magnetoelectroelastic materials eight functions are needed. These functions, named as F_α in equation (5.1), are obtained from the asymptotic singular solution presented in section 2.4.2, and present a similar mathematical structure to those obtained by Béchet et al. (2009) for piezoelectric materials.

$$\begin{aligned} F_\alpha(r,\theta) = \sqrt{r} \, \{ & \rho_1 \cos(\theta_1/2) \quad \rho_2 \cos(\theta_2/2) \quad \rho_3 \cos(\theta_3/2) \quad \rho_4 \cos(\theta_4/2) \\ & \rho_1 \sin(\theta_1/2) \quad \rho_2 \sin(\theta_2/2) \quad \rho_3 \sin(\theta_3/2) \quad \rho_4 \sin(\theta_4/2) \} \end{aligned} \tag{5.13a}$$

where

$$\rho_K(\psi,\mu_K)=\frac{1}{\sqrt{2}}\sqrt[4]{2(|\mu_K|^2-1)(\sin\psi)^2+\mathrm{Re}(\mu_K)\sin(2\psi)-1} \tag{5.13b}$$

and

$$\theta_K=\pi\mathrm{Int}\left(\frac{\psi}{\pi}\right)+\arctan\frac{|\mathrm{Im}(\mu_K)|\tan(\psi-\pi\mathrm{Int}(\frac{\psi}{\pi}))}{1+\mathrm{Re}(\mu_K)\tan(\psi-\pi\mathrm{Int}(\frac{\psi}{\pi}))}. \tag{5.13c}$$

where *Int* denotes the integer part of a real number, μ_I are the four roots of the characteristic equation (2.45) which imaginary part are positive (or equivalently, roots of the eigenvalues problem defined by 2.23) and $\psi=\theta-\alpha$, being ψ the orientation angle of the material axes with respect to the crack (Figure 5.2). Thus, the enrichment functions may be calculated for every poling direction with respect to the crack path.

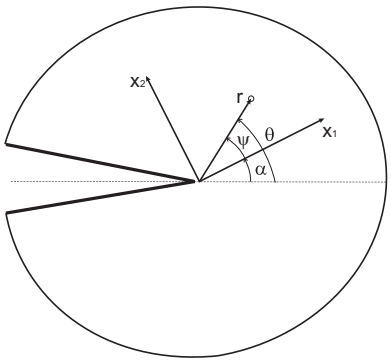

Figure 5.2: Definition of the material axes around the crack tip

5.3 Element partitioning and numerical integration

As it has been said, one of the main advances of the X-FEM respect to the classical FEM approaches in fracture mechanics problems, is the lack of necessity in matching the crack with the mesh.

However, if an element is intersected by a crack, displacement fields to be integrated (see equation 5.3) over the element become discontinuous, due to the discontinuous behavior of both Heaviside and crack tip enrichment functions. As a result of this, the use of ordinary Gauss rules do not provide accurate results of the integration.

In this sense, Dolbow (1999) proposed two methods to overcome this numerical difficulty, consisting in subdividing the intersected element into either triangles or squares.

In this work, triangulation of the partitioned elements have been adopted. This method implies that the sub-triangles edges must be adapted to crack faces (see figure 5.3), since the domain Ω must be divided into non overlapping subdomains, in which continuous functions shall be integrated.

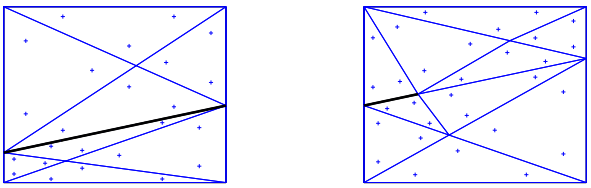

Figure 5.3: Partitioning of a square finite element in 2-D totally (left) or partially (right) intersected by the crack (dark line).

Moreover, ordinary Gauss quadratures have been used for the integration over non enriched elements and for non partitioned enriched elements (in this last case, a higher number of gauss points are considered). Non partitioned enriched elements occur when not all the nodes are enriched. In other words, either those elements which are "the transition" between partitioned elements and the non enriched elements, or, in cases where the crack merges with the mesh, those elements which are separated by the crack.

It should be remarked that when an element is subdivided in triangles, a remeshing is not carried out. As it has been said, the element belonging to the FEM mesh (*parent element*), must be partitioned into non overlapping triangular elements $\Omega_e^{\triangle}$ (*children elements*) so that $\Omega = \bigcup_{e=1}^{m} \Omega_e^{\triangle}$, being m the number of subtriangles in the partition. This partition procedure differs from remeshing in two key features. First, element partitioning is performed only to carry out the numerical integration (no additional degrees of freedom are added); second, the basis functions are tied to the parent element and not to the subtriangles.

5.4 Computation of generalized stress intensity factors

In this part of the work, the computation of ESIF has been carried out by means of an energy integral method, following the technique developed by Rao and Kuna (2008, 2010). A brief description of this approach follows.

5.4.1 Interaction integral method for magnetoelectroelastic materials

Works by Wang and Mai (2003, 2004) provide the expression for the path independent J-integral in a magnetoelectroelastic cracked solid:

$$J = \int_{\Gamma_A} (W\delta_{1j} - \sigma_{ij}u_{i,1} - D_j\phi_{,1} - B_j\varphi_{,1})n_j \, d\Gamma \tag{5.14}$$

where the index i and j vary from 1 to 2 in two-dimensional solids, Γ_A is an arbitrary enclosing contour around the crack tip and n_j is the $j-$th component of the outward unit vector normal to it. W is the electromagnetic enthalpy density which, for a linear magnetoelectroelastic solid, can be expressed as

$$W = \frac{1}{2}(\sigma_{ij}\varepsilon_{ij} - D_jE_j - B_jH_j) \tag{5.15}$$

If the divergence theorem is now applied to equation (5.14), J-integral can be transformed into an equivalent domain form as

$$\begin{aligned} J = &\int_A (\sigma_{ij}u_{i,1} + D_j\phi_{,1} + B_j\varphi_{,1} - W\delta_{1j})q_{,j} \, dA \\ &+ \int_A (\sigma_{ij}u_{i,1} + D_j\phi_{,1} + B_j\varphi_{,1} - W\delta_{1j})_{,j}q \, dA \end{aligned} \tag{5.16}$$

where A is the area inside the contour Γ_A and q is an arbitrary smoothing function such that it is unity at the crack tip and zero on the boundary domain Γ_A. In equation 5.16, the second term vanishes in homogeneous magnetoelectroelastic materials, since the material properties are constant in such solids. Thus, the expression for the J-integral results as follows

$$J = \int_A (\sigma_{ij} u_{i,1} + D_j \phi_{,1} + B_j \varphi_{,1} - W\delta_{1j}) q_{,j}\, dA. \tag{5.17}$$

Equations (5.15) and (5.17) can be rewritten in terms of the extended variables defined in chapter 2 as

$$J = \int_A (\sigma_{Ij} u_{I,1} - W\delta_{1j}) q_{,j}\, dA, \quad W = \frac{1}{2}\sigma_{Ij}\varepsilon_{Ij}. \tag{5.18}$$

Let us now consider two independent equilibrium states for the cracked body. The first one corresponds to the state that must be solved, and the second one corresponds to an auxiliary state, which can be the near-tip displacement field for any of the extended opening fracture modes. In this work, for the sake of convenience, the asymptotic fields expressed in terms of the generalized Stroh's formalism introduced in section 2.2.2 have been used.

The superposition of those two states considered produces another equilibrium state for which the J-integral is

$$\begin{aligned} J^{(S)} &= \int_A ((\sigma^1_{Ij} + \sigma^2_{Ij})(u^1_{I,1} + u^2_{I,1}) - W^S \delta_{1j}) q_{,j} dA \\ W^{(S)} &= \frac{1}{2}[(\sigma^{(1)}_{Ij} + \sigma^{(2)}_{Ij})(\varepsilon^{(1)}_{Ij} + \varepsilon^{(2)}_{Ij})] \end{aligned} \tag{5.19}$$

J-integral given in equation (5.19) can be decomposed into

$$J^{(S)} = J^{(1)} + J^{(2)} + M^{(1,2)} \tag{5.20}$$

The interaction integral M is then given by

$$M^{(1,2)} = \int_A (\sigma^{(1)}_{Ij} u^{(2)}_{I,1} + \sigma^{(2)}_{Ij} u^{(1)}_{I,1} - W^{(1,2)}\delta_{1j}) q_{,j} dA \tag{5.21}$$

with

$$W^{(1,2)} = \frac{1}{2}(\sigma^{(1)}_{Ij}\varepsilon^{(2)}_{Ij} + \sigma^{(2)}_{Ij}\varepsilon^{(1)}_{Ij}) \tag{5.22}$$

Since the elecromagnetomechanical J-integral is equal to the total energy release rate and this can be expressed in terms of the extended stress intensity factors (Tian and Rajapakse, 2005b) as seen in equation (3.146), for two dimensional problems, one can write, for any equilibrium state

$$J = \frac{1}{2}K_{II}^2 Y_{11} + \frac{1}{2}K_I^2 Y_{22} + \frac{1}{2}K_{IV}^2 Y_{44} + \frac{1}{2}K_V^2 Y_{55} + K_I K_{II} Y_{12} \qquad (5.23)$$
$$+ K_I K_{IV} Y_{24} + K_I K_V Y_{25} + K_{II} K_{IV} Y_{14} + K_{II} K_V Y_{15} + K_{IV} K_V Y_{45}$$

which, substituted in (5.20), leads to the following expression of the interaction integral

$$\begin{aligned} M^{(1,2)} &= K_{II}^{(1)} K_{II}^{(2)} Y_{11} + K_I^{(1)} K_I^{(2)} Y_{22} + K_{IV}^{(1)} K_{IV}^{(2)} Y_{44} + K_V^{(1)} K_V^{(2)} Y_{55} \\ &+ (K_I^{(1)} K_{II}^{(2)} + K_{II}^{(1)} K_I^{(2)}) Y_{12} + (K_I^{(1)} K_{IV}^{(2)} + K_{IV}^{(1)} K_I^{(2)}) Y_{24} \\ &+ (K_I^{(1)} K_V^{(2)} + K_V^{(1)} K_I^{(2)}) Y_{25} + (K_{II}^{(1)} K_{IV}^{(2)} + K_{IV}^{(II)} K_I^{(2)}) Y_{14} \\ &+ (K_{II}^{(1)} K_V^{(2)} + K_V^{(1)} K_{II}^{(2)}) Y_{15} + (K_{IV}^{(1)} K_V^{(2)} + K_V^{(II)} K_{IV}^{(2)}) Y_{45} \end{aligned} \qquad (5.24)$$

The individual extended stress intensity factors are evaluated by solving the system of linear algebraic equations obtained from (5.24) by choosing appropriate auxiliary states. For instance, if auxiliary state is taken so that $K_I^{(2)} = 1$ and $K_{II}^{(2)} = 0$, $K_{IV}^{(2)} = 0$, $K_V^{(2)} = 0$, equation (5.24) can be reduced to

$$M^{(1,I)} = K_I^{(1)} Y_{22} + K_{II}^{(1)} Y_{12} + K_{IV}^{(1)} Y_{24} + K_V^{(1)} Y_{25} \qquad (5.25)$$

Similarly, other three equations can be obtained

$$M^{(1,II)} = K_I^{(1)} Y_{12} + K_{II}^{(1)} Y_{11} + K_{IV}^{(1)} Y_{14} + K_V^{(1)} Y_{15} \qquad (5.26)$$

$$M^{(1,D)} = K_I^{(1)} Y_{24} + K_{II}^{(1)} Y_{14} + K_{IV}^{(1)} Y_{44} + K_V^{(1)} Y_{45} \qquad (5.27)$$

$$M^{(1,B)} = K_I^{(1)} Y_{25} + K_{II}^{(1)} Y_{15} + K_{IV}^{(1)} Y_{45} + K_V^{(1)} Y_{55} \qquad (5.28)$$

So, finally, the determination of the extended stress intensity factors is reduced to solving the following system of linear equations:

$$\begin{pmatrix} M^{(1,II)} \\ M^{(1,I)} \\ M^{(1,IV)} \\ M^{(1,V)} \end{pmatrix} = \mathbf{Y} \begin{pmatrix} K_{II}^{(1)} \\ K_{I}^{(1)} \\ K_{IV}^{(1)} \\ K_{V}^{(1)} \end{pmatrix}$$

5.5 Validation

Some static crack problems in magnetoelectroelastic media are solved to validate the formulation. The numerical results obtained by the X-FEM are compared with those obtained by the boundary element formulation presented previously. As in the previous chaper, a $BaTiO_3 - CoFe_2O_4$ composite with a V_f=0.5 is considered. The properties of such material are shown in table 4.1.

In all computations linear quadrilateral elements are used. A 2×2 Gauss quadrature rule is used in every non-enriched element, whereas for non-partitioned enriched elements a 5×5 Gauss rule is used. For enriched elements that are partitioned into subtriangles, a seven point Gauss rule is used in each one.

5.5.1 Slanted central crack in a magnetoelectroelastic plate

A finite magnetoelectroelastic plate with a central inclined crack under combined electro-magneto-mechanical loads is analyzed. In Figure 5.4 the geometry and loading are described. The ratio between the crack length and plate width is $a/w = 0.2$. The plate is under uniform tension in the x_2 direction, σ_{22}, and subjected to both electric and magnetic loadings: $D_2 = 0.1 \cdot 10^{-9}\sigma_{22}(C \cdot N^{-1})$ and $B_2 = 1 \cdot 10^{-9}\sigma_{22}(A^{-1} \cdot m)$. The prob-

Table 5.1: Benchmark results for a crack in a finite plate.

θ	$K_I/(\sigma_{22}\sqrt{\pi a})$	$K_{II}/(\sigma_{22}\sqrt{\pi a})$	$K_{IV}/(D_2\sqrt{\pi a})$	$K_V/(B_2\sqrt{\pi a})$
0^o	1.0241	~ 0	1.0226	1.0395
15^o	0.9562	0.2506	0.9869	1.0103
30^o	0.7720	0.4361	0.8845	0.9206

lem has been solved for three different uniform meshes (25×50, 50×100, 75×150), and for three different angles of the crack with respect to the x_1 axis ($\theta = 0°$, $15°$, $30°$). The polarization direction coincides with the x_2-axis, and the benchmark results, obtained by means of the BEM formulation proposed in this thesis are presented in table 5.1.

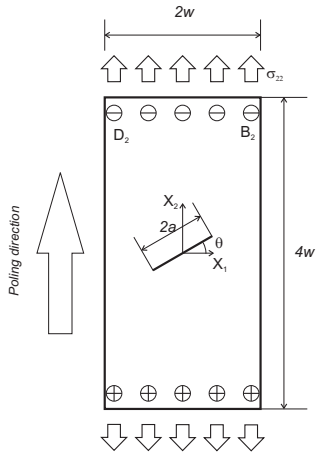

Figure 5.4: Geometry and loads for a magnetoelectroelastic plate with a slanted crack

In table 5.2, the extended finite element results, normalized with the BEM ones, are presented for three meshes. A good agreement between

both formulations is found.

Table 5.2: ESIF for a crack in a finite plate.

θ	$ESIF$	(25×50)	(50×100)	(75×150)
0^o	K_*^I	0.9822	0.9911	0.9916
	K_{II}^*	~ 1	~ 1	~ 1
	K_{IV}^*	0.9901	0.9940	0.9952
	K_V^*	0.9561	0.9827	0.9846
15^o	K_I^*	1.0256	0.9918	0.9951
	K_{II}^*	1.0311	0.9885	0.9876
	K_{IV}^*	1.0359	1.0181	1.0186
	K_V^*	0.9718	0.9575	0.9723
30^o	K_I^*	0.9803	1.0062	1.0116
	K_{II}^*	1.0541	1.0071	0.9998
	K_{IV}^*	1.0372	1.0178	1.0137
	K_V^*	0.9472	0.9995	0.9987

5.5.2 Double-edge crack in magnetoelectroelastic plate

A double-edge crack in a finite magnetoelectroelastic plate under combined electro-magneto-mechanical loads is next analyzed. The geometry and loading are illustrated in Figure 5.5. The ratio between the crack length and the plate width is given by $a/w = 0.25$, being the load values and polarization angle the same as in the previous example. In table 5.3 the benchmark results for the normalized ESIF are shown.

In table 5.4, the extended finite element results, normalized with the BEM ones, are presented for three meshes. A good agreement between

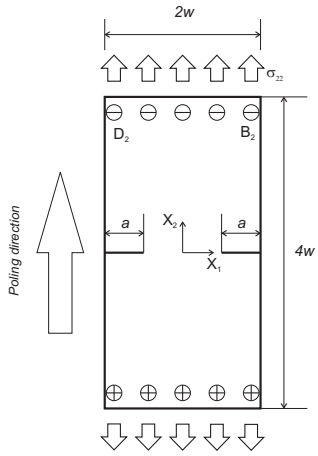

Figure 5.5: Geometry and loads for a magnetoelectroelastic plate with a double-edge crack

Table 5.3: Benchmark results for a double edge crack in a finite plate.

$K_I/(\sigma_{22}\sqrt{\pi a})$	$K_{II}/(\sigma_{22}\sqrt{\pi a})$	$K_{IV}/(D_2\sqrt{\pi a})$	$K_V/(B_2\sqrt{\pi a})$
1.1197	~ 0	1.1062	1.3636

both formulations is found. It should be remarked that identical results for both crack tips are obtained.

Table 5.4: ESIF for a double edge crack in a finite plate.

$ESIF$	(25×50)	(50×100)	(75×150)
K_I^*	0.9732	0.9844	0.9845
K_{II}^*	~ 1	~ 1	~ 1
K_{IV}^*	0.9778	0.9855	0.9848
K_V^*	0.9408	0.9825	0.9840

Chapter 6

Crack face boundary conditions

6.1 Introduction

In fracture mechanics analysis of multifield materials in general, and of magnetoelectroelastic media in particular, three different boundary conditions on open crack surfaces can be considered, depending on the electromagnetic conductivity considered between both crack faces. These conditions were summarized in chapter 2 and, in this chapter, the procedure to solve a fracture mechanics problems considering any of those crack face boundary conditions will be introduced, and the implications of them on the fracture parameters, studied by solving simple and multiple cracks problem.

For solving *impermeable* and *permeable* crack problems (ideal crack face boundary conditions), it will be enough to apply the corresponding boundary conditions to the system of equations obtained by the evaluation of the boundary integral equations (3.37-3.38). However, the more realistic

semipermeable condition is given by a non-linear equation. Then, for solving that problem, an iterative algorithm will be proposed and implemented. That algorithm is a generalization of the one proposed by Denda (2008) for piezoelectric cracked solids.

6.2 Numerical solution algorithm for semipermeable cracks

Let us call the jumps of the electric and magnetic potentials in the crack as $\delta_4 = (\phi^+ - \phi^-)$ and $\delta_5 = (\varphi^+ - \varphi^-)$. The semipermeable solution implies that the electric and magnetic potentials, the electric displacement and the magnetic induction on the crack faces are generally different to zero. Thus, the semipermeable crack solution is somewhere in between the two ideal crack surface boundary condition, so the semipermeable values of the jump in the electric and magnetic potentials, δ_4 and δ_5, will be equal to the impermeable values multiplied by a proportionality factor, h_e and h_m, lower than one. An iteration procedure to determine these factors is proposed herein. This procedure is based on the search of adequate values of δ_4 and δ_5. The use of them as boundary conditions of the problem, shall lead to the values of the permittivity and permeability in the crack, equation (2.35). The iteration will be carried out until those values are equal to the reference values of the permittivity and the permeability in the medium between the crack surfaces, ϵ_0 and γ_0. The following iteration procedure for multiple cracks problem is proposed.

1. Get the impermeable solution $\delta_4^{[0]}$, $\delta_5^{[0]}$, which will be used as the starting point of the iteration procedure. The number between brackets denotes number of iteration step.

2. Define, for each crack k, two pairs of proportionality parameters h_e^{ki} and h_m^{ki} (i=1,2), which vary in the interval (0,1). In figure 6.1 it is shown the behaviors of the permittivity and the permeability in a crack with respect to parameters h_e and h_m. In such figure, the flat grey surfaces denotes the values of ϵ_0 (left) and γ_0 (right). Let us remark that the sought point will be the intersection between the intersection lines appearing in each figure.

3. **(a)** Take, for each crack, h_e^{k1} and h_m^{k1} slightly bigger than zero (what would correspond to the quasi-permeable solution) and h_e^{k2} and h_m^{k2} slightly lower than one (what would correspond to the quasi-impermeable solution). Then, set

$$\delta_4^{[k1]} = h_e^{k1}\delta_4^{[0]} \quad ; \quad \delta_4^{[k2]} = h_e^{k2}\delta_4^{[0]}$$
$$\delta_5^{[k1]} = h_m^{k1}\delta_5^{[0]} \quad ; \quad \delta_5^{[k2]} = h_m^{k2}\delta_5^{[0]}$$

(b) Calculate the mechanical crack opening displacement, the electric displacement and the magnetic induction based on the set values introduced in the previous item.

(c) Calculate for each crack k and each parameter $h_e^{k1}, h_e^{k2}, h_m^{k1}, h_m^{k2}$ at M points (nodal points) ξ_j

$$\epsilon_j^{ki} = D_n^{ki}(\xi_j)\frac{\delta_2^{ki}(\xi_j)}{\delta_4^{ki}(\xi_j)} \tag{6.2}$$

$$\gamma_j^{ki} = B_n^{ki}(\xi_j)\frac{\delta_2^{ki}(\xi_j)}{\delta_5^{ki}(\xi_j)} \tag{6.3}$$

which are obtained by the substitution in equation (2.35) of the corresponding ECOD and the electric (D_n) and magnetic (B_n) tractions previously obtained in step (3b).

(d) Calculate the averages for each crack and each pair of parameters h_e^{ki} and h_m^{ki} of the parameteres defined in section (3c).

$$\overline{\epsilon}^{ki} = \frac{\sum_{j=1}^{M} \epsilon_j^{ki}}{M} \tag{6.4}$$

$$\overline{\gamma}^{ki} = \frac{\sum_{j=1}^{M} \gamma_j^{ki}}{M} \tag{6.5}$$

This parameter are the so-called electric permittivity in the crack and magnetic permeability in the crack, respectively.

(e) While the electric permittivity and magnetic permeability of any crack is not equal to the values for the medium between the crack surfaces, iterate using a procedure to solve non-linear equations, until a pair of values $h_e^{k[n]}$ and $h_m^{k[n]}$ for each crack is obtained. Let us remark that all those values may be different.

4. After setting $\delta_4^{k[n]} = h_e^{ki[n]}\delta_4^{[0]}$ and $\delta_5^{k[n]} = h_m^{ki[n]}\delta_5^{[0]}$, solve the problem required to get the semipermeable solution searched.

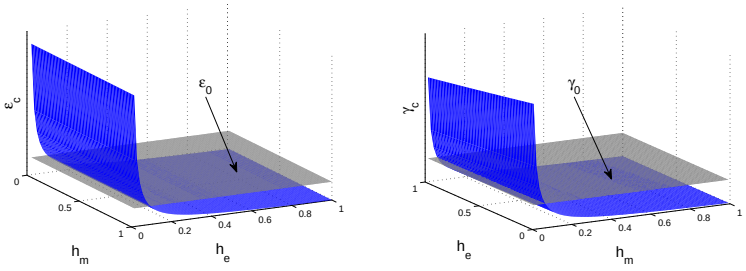

Figure 6.1: Behavior of the permittivity (left) and the permeability (right) in the crack with respect to parameters h_e^{ki} and h_m^{ki}

6.3 Validation of the algorithm

In this section, several fracture mechanics problems for different crack faces boundary conditions will be solved. In all simulations, a $BaTiO_3{-}CoFe_2O_4$ magnetoelectroelastic solid with a $V_f = 0.5$, which properties are listed in table 4.1, will be considered. In all cases, the medium between both crack faces is air, what implies that the electric permittivity and magnetic permeability are, respectively, $\epsilon_0 = 8.8542 \cdot 10^{-12} N/V^2$ and $\gamma_0 = 4\pi \cdot 10^{-7} N/A^2$.

6.3.1 Griffith crack in a magnetoelectroelastic solid

In order to validate the proposed algorithm, numerical results are obtained and compared with the analytical solution of a single horizontal crack of length *2a* in an infinite magnetoelectroelastic domain (see figure 4.1). This solution, first obtained by Wang and Mai (2006), will be briefly presented.

The extended crack opening displacements δ_I, $I = 1, ..., 5$; are given by

$$\delta_I = u_I^+ - u_I^- = 2Y_{IJ}(\sigma_{J2}^{\infty} - \sigma_{J2}^{c})\sqrt{a^2 - x_1^2} \tag{6.6}$$

where $\mathbf{Y}$ is the compliance (Irwin) matrix defined in equation (3.145), σ_{J2}^{∞} are the components of the extended stress tensor applied, σ_{J2}^{c} are the components of the extended stress tensor on the crack surfaces, and the summation rule over repeated is applied. The different crack face boundary conditions that may be considered for the crack are

(i) *Fully impermeable crack.* In this case, the crack is extended traction free, what implies that

$$D_2^c = 0 \;\; ; \;\; B_2^c = 0 \tag{6.7}$$

where, since $D_2^+ = D_2^-$ and $B_2^+ = B_2^-$, the upperindex c has been used to denote either of the crack surfaces.

(ii) *Fully permeable crack.* For fully permeable cracks no jump in the electromagnetic potential appear. This condition can be expressed as

$$\delta_4 = 0 \quad ; \quad \delta_5 = 0 \tag{6.8}$$

The substitution of that condition in (6.6) will lead to a system of equation whose solution provides the analytical expressions of the extended tractions on the crack faces

$$D_2^c = \frac{(Y_{4J}Y_{55} - Y_{5J}Y_{45})}{(Y_{44}Y_{55} - Y_{54}Y_{45})}\sigma_{J2}^{\infty} \tag{6.9a}$$

$$B_2^c = \frac{(Y_{5J}Y_{44} - Y_{4J}Y_{54})}{(Y_{44}Y_{55} - Y_{54}Y_{45})}\sigma_{J2}^{\infty} \tag{6.9b}$$

(iii) *Semipermeable crack.* The semipermeable crack conditions are

$$D_2^c\delta_2 = -\epsilon_0\delta_4 \quad ; \quad B_2^c\delta_2 = -\gamma_0\delta_5 \tag{6.10}$$

where ϵ_0 is the permittivity of the medium between the crack faces and γ_0 its permeability. Substituting now (6.10) in (6.6) and operating a non-linear system of equations which defines the extended tractions in a semipermeable crack, it will be obtained.

$$D_2^c = -\epsilon_0\frac{Y_{4J}\sigma_{J2}^{\infty} - Y_{44}D_2^c - Y_{45}B_2^c}{Y_{2J}\sigma_{J2}^{\infty} - Y_{24}D_2^c - Y_{25}B_2^c} \tag{6.11a}$$

$$B_2^c = -\gamma_0\frac{Y_{5J}\sigma_{J2}^{\infty} - Y_{54}D_2^c - Y_{55}B_2^c}{Y_{2J}\sigma_{J2}^{\infty} - Y_{24}D_2^c - Y_{25}B_2^c} \tag{6.11b}$$

where ϵ_0 is the permittivity of the medium between the crack faces and γ_0 its permeability.

The analytical solution previously deduced will be compared with the results obtained with the proposed formulation. In figure 6.2 the mechanical opening displacement are shown for the case in which only a mechanical loading is applied and in the case in which a combination of loads defined by $\sigma_{22}^{\infty} = 1N/m^2$, $D_2^{\infty} = 10^{-9}C/N$ and $B_2^{\infty} = 10^{-8}A^{-1} \cdot m$ is applied. The analytical solution is plotted in lines, comparing them with the results obtained numerically (points), and those magnitudes are normalized with their respective value under permeable conditions in $x_1 = 0$. Excellent agreement between both sets of solutions is observed. It can be seen that, in both cases, the semipermeable solution is between the permeable and the impermeable ones. When only mechanical loading is applied, the crack opening displacement under impermeable condition, δ_2^{imp}, is the smallest value, while the presence of positive electromagnetic loads, which tend to open the crack, leads to the largest values, because any degree of permeability provokes that the influence of those loads decreases. Let us remark that the permeable solution is independent of the presence of electromagnetic loading and the resulting mechanical stress intensity factors are independent of the boundary condition considered.

In figure 6.3 the analytically obtained jumps in the electric and magnetic potentials are compared with the results obtained numerically (points) with an excellent agreement again. Those magnitudes are normalized with their respective values under impermeable conditions in the center of the crack ($x_1 = 0$).

In figure 6.4, the electric displacement and magnetic induction on the crack surfaces are shown in comparison with the analytical results (lines),

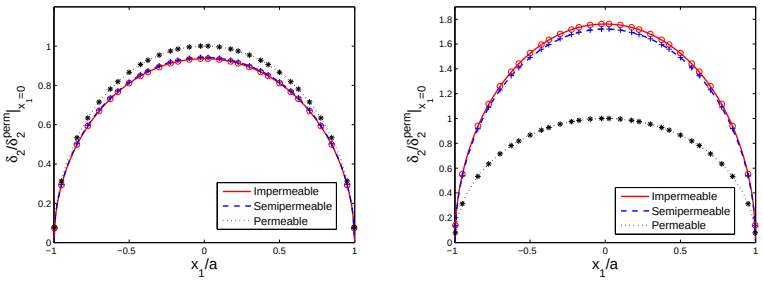

Figure 6.2: Crack opening displacement when only a mechanical loading is applied (left) and a full combination of electromagnetomechanic loading is applied (right).

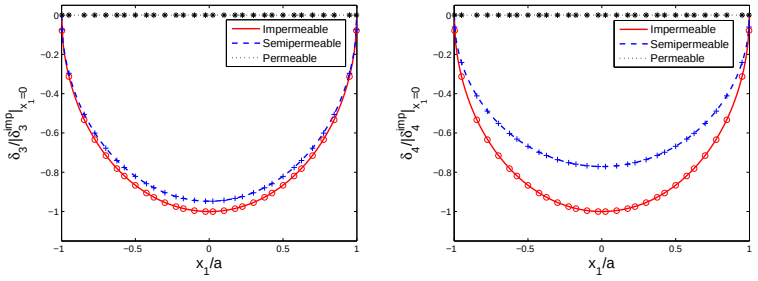

Figure 6.3: Electric (left) and magnetic (right) potentials jumps on the crack.

also for the three boundary conditions considered and normalized with the applied electric and magnetic loads. In all figures, an excellent agreement between the numerical and analytical results can be observed.

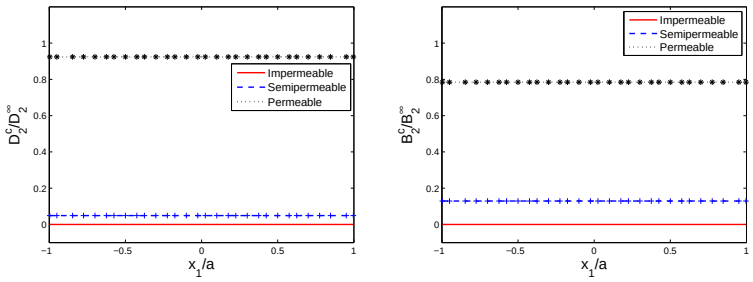

Figure 6.4: Electric displacement (left) and magnetic induction (right) on the crack surfaces.

6.3.2 Central straight crack in a finite plate

A central crack in a magnetoelectroelastic plate like the one in Figure 4.35 is analyzed. The ratio between the crack length and the plate width is $a/\omega = 0.2$. Thirty two quadratic elements were used for meshing the external boundary, while ten equal quadratic elements were taken for the crack.

In table 6.1 the normalized fracture parameters are shown when the loading combination is $\sigma_{22}^{\infty} = 1N/m^2$, $D_2^{\infty} = 10^{-9}C/N$ and $B_2^{\infty} = 10^{-8}A^{-1} \cdot m$. ESIF are normalized for the corresponding values to a Griffith impermeable crack subjected to the same loads, while the different energy release rates are normalized with the absolute value of the total energy release rate for an impermeable crack in an infinite domain. Considerable differences were found in the electromagnetic stress intensity factors when different crack face boundary conditions (CFBC) were considered but not in the mechanical SIF. As expected, electric and magnetic energy release rates are negligible when permeable cracks are analyzed, what implies that mechanical and total energies are the same.

Table 6.1: Fracture parameters for straight crack in a plate

ERR	CFBC	TIP A-B	ESIF	CFBC	TIP A-B
$\overline{G}_{Tot}$	Imp	-1.0354	$\overline{K}_I$	Imp	1.0255
	Semip	-0.9162		Semip	1.0255
	Perm	0.1276		Perm	1.0258
$\overline{G}_M^{I+II}$	Imp	0.2240	$\overline{K}_{II}$	Imp	2.4187e-009
	Semip	0.2188		Semip	2.4185e-009
	Perm	0.1276		Perm	2.4145e-009
$\overline{G}_{ELEC}$	Imp	-1.2565	$\overline{K}_{IV}$	Imp	1.0190
	Semip	-1.1330		Semip	0.9696
	Perm	~ 0		Perm	0.0777
$\overline{G}_{MAGN}$	Imp	$-0.2894 \cdot 10^{-2}$	$\overline{K}_V$	Imp	1.0205
	Semip	$-0.1946 \cdot 10^{-2}$		Semip	0.8893
	Perm	~ 0		Perm	0.2212

In figure 6.5, total energy release rate is shown for $\sigma_{22}^{\infty} = 1N/m^2$, $D_2^{\infty} = 10^{-9}C/N$ and different values of magnetic loading, for the three crack face boundary conditions considered. The results are normalized with the value of the total energy release rate corresponding to a Griffith impermeable crack subjected only to a mechanical load. If a permeable crack is considered, the normalized G_{Tot} takes a constant value equal to G_{Tot}^*=1.124, which is the same for any loading combination. The presence of electromagnetic fields shall decrease the energy release rate when the crack is not fully permeable. This fact implies that the total energy release rate can not be adopted as a fracture criteria. Moreover, it can be realized that the nonlinear effect of loadings and that the energy release rate is always smaller

in semipermeable cracks.

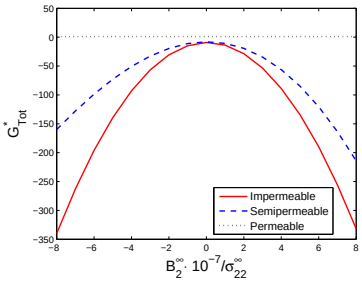

Figure 6.5: Total energy release rate for straight crack in a plate.

6.3.3 Three parallel cracks in an unbounded domain

To further confirm the validity of the iteration scheme, a case involving interaction among three parallel cracks in an infinite will be next considered. In this case the solutions for the upper or lower cracks are different to the middle one's. The distance between cracks is half the semilength of each crack as shown in Figure 6.6. The values of the loads are again $\sigma^{\infty}_{22} = 1N/m^2$, $D^{\infty}_2 = 10^{-9}C/N$ and $B^{\infty}_2 = 10^{-8}A^{-1} \cdot m$, and ten equal elements for each crack are used for meshing purposes.

In figure 6.7, mechanical opening displacement as well as the jump in the electric and the magnetic potentials are plotted. Absolute values of the ECOD are always smaller in the central crack, and any degree of permeability in the crack shall reduce them.

In table 6.2 the normalized ESIF in tips A and B (figure 6.6) are shown. Such ESIF are normalized with the corresponding ones to an impermeable Griffith crack.

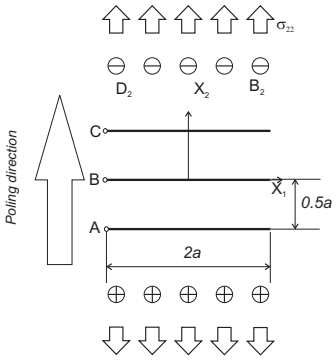

Figure 6.6: Three parallel cracks in a magnetoelectroelastic domain.

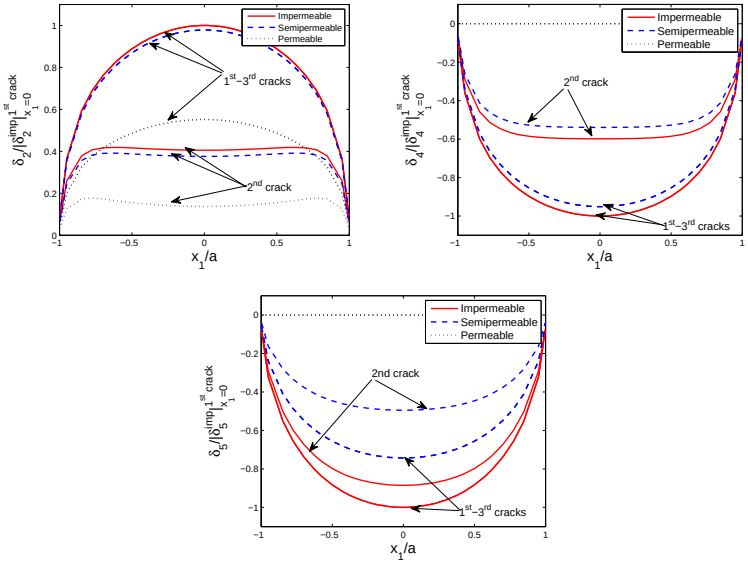

Figure 6.7: ECOD for three parallel cracks.

Table 6.2: ESIF in tips A and B (figure 6.6) for three parallel cracks

ESIF	CFBC	TIP A	TIP B
$\overline{K}_I$	Imp	0.6865	0.4634
	Semip	0.6872	0.4626
	Perm	0.6865	0.4634
$\overline{K}_{II}$	Imp	0.1379	~ 0
	Semip	0.1385	~ 0
	Perm	0.1467	~ 0
$\overline{K}_{IV}$	Imp	0.7405	0.5992
	Semip	0.7068	0.5429
	Perm	0.0514	0.0345
$\overline{K}_V$	Imp	0.7939	0.6643
	Semip	0.6717	0.4739
	Perm	0.1482	0.0993

Moreover, in tables 6.3 and 6.4, the energy release rates at tips A and B, respectively, are shown for two different combination of loads; the first one (*Comb. 1*) is only a mechanical loading, while the second one (*Comb. 2*) is the combination described above. The values obtained are normalized with total energy corresponding to a Griffith impermeable crack subjected only to a mechanical load. Total and mechanical energy release rates present the same value and are independent of the presence of electromagnetic loadings when a permeable crack face boundary condition is considered. The presence of those loads, however, change the tendency of the behavior of the mechanical energy release rate: when only a mechanical load is applied, G_M^{I+II} is increased with the permeability and permittivity of the medium

while, in the other hand the action of electromagnetical loadings make that magnitude maximum when the medium is considered to be impermeable.

Table 6.3: ERR in tip A for three parallel cracks (figure 6.6)

ERR	CFBC	TIP A - $Comb_1$	TIP A - $Comb_2$
$\overline{G}_{Tot}$	Imp	0.4889	-0.4975
	Semip	0.4949	-4.4644
	Perm	0.5241	0.5241
$\overline{G}_M^{I+II}$	Imp	0.4912	0.9254
	Semip	0.4941	0.9064
	Perm	0.5241	0.5241
$\overline{G}_{ELEC}$	Imp	$-2.2063 \cdot 10^{-3}$	-5.9026
	Semip	$0.6037 \cdot 10^{-3}$	-5.3601
	Perm	~ 0	~ 0
$\overline{G}_{MAGN}$	Imp	$-1.0118 \cdot 10^{-4}$	$-1.7043 \cdot 10^{-2}$
	Semip	$0.2032 \cdot 10^{-3}$	$-1.0714 \cdot 10^{-2}$
	Perm	~ 0	~ 0

Table 6.4: ERR in tip B for three parallel cracks (figure 6.6)

ERR	CFBC	TIP B - $Comb_1$	TIP B - $Comb_2$
$\overline{G}_{Tot}$	Imp	0.2017	-3.4715
	Semip	0.2119	-2.7697
	Perm	0.2257	0.2257
$\overline{G}_M^{I+II}$	Imp	0.2073	0.4530
	Semip	0.2119	0.4287
	Perm	0.2257	0.2257
$\overline{G}_{ELEC}$	Imp	$-5.3847 \cdot 10^{-3}$	-3.9117
	Semip	$-0.0691 \cdot 10^{-3}$	-3.1933
	Perm	~ 0	~ 0
$\overline{G}_{MAGN}$	Imp	$-0.2358 \cdot 10^{-3}$	$-1.2837 \cdot 10^{-2}$
	Semip	$-0.9695 \cdot 10^{-4}$	$-0.5118 \cdot 10^{-2}$
	Perm	~ 0	~ 0

Chapter 7

Conclusions and future developments

7.1 Conclusions

In this work, a deep study about the behavior of cracked magnetoelectroelastic solids under static, time-harmonic and impact electromagnetomechanic loadings has been carried out. For that purpose two numerical tools have been implemented, based on the hypersingular formulation of the boundary element method and the extended finite element method.

The BEM model was performed following the ideas proposed by García-Sánchez and coworkers (2005; 2008a; 2008b) for anisotropic and piezoelectric material models. For its development, certain fundamental solutions are needed. In static problems, that fundamental solution (already available in literature, like in the work by Liu et al., 2001) has an explicit form. However, for dynamic problems, the fundamental solution needed presents an integral form. These dynamic Green's functions have been obtained

during the realization of this work.

When those fundamental solutions are implemented in a BEM code, some singular integrals arise in those cases in which the collocation point belongs to the element where the integration is being performed. The most delicate issue in the dual formulation is the treatment of the strongly singular and hypersingular integrals, which are successfully carried out by means of a change of variable that decompose those integrals in some regular integrals plus singular integrals with known analytical solutions. In other words, numerical integrations are restricted to regular integrals, thus increasing the accuracy of the proposed approach.

Regarding BEM for the study of dynamic fracture, the implementation of the dynamic Green's functions admit a decomposition in two parts, a singular (which coincides with the static solution, except for a constant and, thus, is independent of the frequency) and a regular one. However, that regular part presents, in the terms corresponding to the hypersingular integrals, a logarithmic singularity (which can be solved by the use of logarithmic quadratures). Moreover, it presents and oscillatory behavior for high frequencies or integration points far from the source.

The time domain BEM formulation involves Riemann convolution products which, in this work, has been approximated by the Lubich's quadrature formula. The solution of several problems reveal a high stability in the formulation as well as an independency between spatial and time discretization, not present in other formulations.

For the computation of the fracture parameters, a quarter point discontinuous element at the crack tip has been used. This element present a collocation point very close to the crack tip, where displacements and electric and magnetic potentials have known expressions in terms of the

extended stress intensity factors. The substitution in them of the extended displacements in the nearest collocation point to the crack tip allows to obtain the fracture parameters with almost no computational cost and a great accuracy, as it has been demonstrated by comparing the results obtained numerically with the results available in the literature obtained by different methods.

Most of the work has been carried out under the assumption of impermeable cracks. However, an algorithm for the study of semipermeable and permeable cracks subjected to static loads, has been designed and implemented in the last section of this thesis. The analysis of the results obtained considering other crack faces boundary conditions reveal differences, which might be considerable, in the fracture parameters depending on the condition adopted. However, it suggests that the approximated impermeable condition is good enough to obtain a first approximation of the mechanical energy release rate, which may be involved in a fracture criteria, when air or vacuum is considered between crack surfaces. As a matter of fact, that magnitude, as well as electric and magnetic energy release rates, decrease when the permittivity and/or permeability of the medium is increased.

In this work, a X-FEM model has been developed as well for the study of static fracture. For that purpose, new crack tip enrichment functions have been obtained, and some problems solved, comparing the results with those obtained with the BEM formulation also presented. A good accuracy is obtained in the fracture parameters, which have been obtained by means of the equivalent domain form of the Interaction Integral Method.

Let us now remark that all the models developed in this work may be used for the analysis of cracked anisotropic and piezoelectric solids, by vanishing the corresponding coupling properties.

7.2 Future Developments

This work presented robust and accurate numerical models for the study of fracture mechanics problems in 2-D magnetoelectroelastic media. However, some issues are still open.

The most direct future development which can be performed in the model, might be considering different crack faces boundary conditions in dynamic problems, adopting the more realistic condition in transient periods. Recently, Landis (2004) suggested the so called *energetically consistent* boundary conditions for piezoelectric solids, which improved the crack faces boundary conditions obtained by the *capacitor analogy* proposed by Hao and Shen (1994). This new condition leads to the presence of mechanical tractions on the crack surfaces. An extension of this model and a comparative study with the results obtained in this work should be a future work.

As it has been already said, time-harmonic fundamental solution presents an oscillatory behavior which makes more difficult to obtain results for high frequency and/or far field. In this sense, it is necessary to obtain an asymptotic far field solution as an extension of the obtained by Sáez and Domínguez (2000) for transversely isotropic materials.

Both BEM and X-FEM have been proved to be accurate numerical tools for the study of crack growth in cracked solids. However, no fracture criteria is unanimously accepted for magnetoelectroelastic solids. In this sense, the performance of extensive experimental tests are definitely needed to advance in the fracture knowledge of magnetoelectroelastic materials.

The X-FEM model may be improved in a double way. First, by obtaining more compact crack tip enrichment functions based on the matrix form (Stroh's formalism) of the asymptotic displacement fields. This is an

already started work by the author. Moreover, the model may be improved by the use of blending elements, as well as by incorporating second order terms to the asymptotic expressions of the fields (T-stress), in order to develop a Hybrid Analytical and X-FEM (HAX-FEM) model in an similar way as done by Réthoré et al. (2009) for isotropic materials. With such improvements, the approximation of the ECOD may be accurate enough to obtain the fracture parameters by a direct evaluation, what would reduce the computational cost in the postprocessing.

Appendix A

Definition of the two-dimensional characteristics

The two dimensional material parameters introduced in section 2.4.3 follow from the three dimensional material properties defined in section 2.2.

$$a_{11} = \frac{1}{A}\left(c_{22}(\epsilon_{22}\gamma_{22} - \beta_{22}^2) + \epsilon_{22}h_{22}^2 + \gamma_{22}e_{22}^2 - 2\beta_{22}e_{22}h_{22}\right)$$
$$a_{12} = -\frac{1}{A}\left(c_{12}(\epsilon_{22}\gamma_{22} - \beta_{22}^2) + \epsilon_{22}h_{21}h_{22} + \gamma_{22}e_{21}e_{22} - \beta_{22}(e_{21}h_{22} - e_{22}h_{21})\right)$$
$$b_{21} = \frac{1}{A}\left(\gamma_{22}(c_{22}e_{21} - c_{12}e_{22}) - \beta_{22}(c_{22}h_{21} - c_{12}h_{22}) + h_{22}(h_{22}e_{21} - h_{21}e_{22})\right)$$
$$d_{21} = -\frac{1}{A}\left(\epsilon_{22}(c_{12}h_{22} - c_{22}h_{21}) + \beta_{22}(c_{22}e_{21} - c_{12}e_{22}) + e_{22}(h_{22}e_{21} - h_{21}e_{22})\right)$$
$$a_{22} = \frac{1}{A}\left(\gamma_{22}(c_{11}\epsilon_{22} + e_{21}^2) + \epsilon_{22}h_{21}^2 - \beta_{22}(c_{11}\beta_{22} + 2e_{21}h_{21})\right)$$
$$b_{22} = -\frac{1}{A}\left(\gamma_{22}(c_{12}e_{21} - c_{11}e_{22}) - \beta_{22}(c_{12}h_{21} - c_{11}h_{22}) + h_{21}(h_{22}e_{21} - h_{21}e_{22})\right)$$
$$d_{22} = \frac{1}{A}\left(\epsilon_{22}(c_{11}h_{22} - c_{12}h_{21}) + \beta_{22}(c_{12}e_{21} - c_{11}e_{22}) + e_{21}(h_{22}e_{21} - h_{21}e_{22})\right)$$
$$a_{33} = \frac{1}{B}\left(\gamma_{11}\epsilon_{11} - \beta_{11}^2\right)$$

$$b_{13} = \frac{1}{B}\left(\gamma_{11}e_{13} - h_{13}\beta_{11}\right)$$
$$d_{13} = -\frac{1}{B}\left(\beta_{11}e_{13} - h_{13}\epsilon_{11}\right)$$
$$\delta_{11} = \frac{1}{B}\left(\gamma_{11}c_{33} + h_{13}^2\right)$$
$$\Delta_{11} = -\frac{1}{B}\left(\beta_{11}c_{33} + e_{13}h_{13}\right)$$
$$\delta_{22} = \frac{1}{A}\left(\gamma_{22}(c_{11}c_{22} - c_{12}^2) + c_{11}h_{22}^2 + c_{22}h_{21}^2 - 2c_{12}h_{12}h_{22}\right)$$
$$\Delta_{22} = -\frac{1}{A}\left(\beta_{22}(c_{11}c_{22} - c_{12}^2) + c_{11}e_{22}h_{22} + c_{22}e_{21}h_{21} - c_{12}(e_{22}h_{21} + e_{21}h_{22})\right)$$
$$\zeta_{11} = \frac{1}{B}\left(\epsilon_{11}c_{33} + e_{13}^2\right)$$
$$\zeta_{22} = \frac{1}{A}\left(\epsilon_{22}(c_{11}c_{22} - c_{12}^2) + c_{11}e_{22}^2 + c_{22}e_{21}^2 - 2c_{12}e_{12}e_{22}\right)$$

where the Voigt notation has been used and

$$\begin{aligned} A =& (c_{11}c_{22} - c_{12}^2)(\epsilon_{22}\gamma 22 - \beta_{22}^2) + e_{21}^2(c_{22}\gamma 22 + h_{22}^2) + e_{22}^2(c_{11}\gamma 22 + h_{21}^2) \\ &+ 2\beta_{22}(e_{21}(c_{12}h_{22} - c_{22}h_{21}) + e_{22}(c_{12}h_{21} - c_{11}h_{22})) \\ &- 2e_{21}e_{22}(c_{12}\gamma_{22} + h_{21}h_{22}) + \epsilon_{22}(c_{11}h_{22}^2 + c_{22}h_{21}^2 - c_{12}h_{21}h_{22}) \end{aligned}$$

and

$$B = \epsilon_{11}(c_{33}\gamma_{11} + h_{13}^2) - \beta_{11}(c_{33}\beta_{11} + 2e_{13}h_{13}) + \gamma_{11}e_{13}^2$$

Appendix B

Radon transform

The Radon transform of an arbitrary function $f(\mathbf{x})$ is defined by

$$\hat{f}(s,\mathbf{n}) = \mathsf{R}\left\{f(\mathbf{x})\right\} = \int\limits_{s} f(\mathbf{x})\delta(s-\mathbf{n}\cdot\mathbf{x})d\mathbf{x}\,, \tag{B.1}$$

where $s = \mathbf{n}\cdot\mathbf{x}$ is a real transform parameter and $\mathbf{n}$ is a unit normal vector. The Radon transform is an integration of $f(\mathbf{x})$ over $\mathbf{n}\cdot\mathbf{x} = s$, i.e., over a surface for 3-D and along a line for 2-D.

The inverse Radon-transform is given by

$$f(\mathbf{x}) = \mathsf{R}^*\left\{\bar{f}(s,\mathbf{n})\right\} = \int\limits_{|\mathbf{n}|=1} \bar{f}(\mathbf{n}\cdot\mathbf{x},\mathbf{n})d\mathbf{n}\,, \tag{B.2}$$

where

$$\bar{f}(s,\mathbf{n}) = \mathsf{K}\left\{\hat{f}(s,\mathbf{n})\right\} = \begin{cases} -\dfrac{1}{8\pi^2}\partial_s^2\hat{f}(s,\mathbf{n})\,, & \text{for} \quad \text{3-D} \\ \dfrac{1}{4\pi^2}\displaystyle\int\limits_{-\infty}^{\infty}\frac{\partial_\sigma\hat{f}(\sigma,\mathbf{n})}{s-\sigma}d\sigma\,, & \text{for} \quad \text{2-D} \end{cases} \tag{B.3}$$

The inverse Radon transform R^* defined by (B.2) is a surface integral over a unit sphere in 3-D case and a line integral over a unit circle in 2-D case.

The main properties of the Radon transform defined in equation (B.1) are

A Homogeneity

$$\widehat{f}(cs, c\mathbf{n}) = \frac{1}{c}\widehat{f}(s, \mathbf{n}) \tag{B.4}$$

B Linearity

$$R\{c_1 f + c_2 g\} = c_1\widehat{f} + c_2\widehat{g} \tag{B.5}$$

C Transform of derivatives

$$R\left\{\frac{\partial}{\partial x_i} f(\mathbf{x})\right\} = n_i \frac{\partial}{\partial s}\widehat{f}(s, \mathbf{n}) \tag{B.6}$$

$$R\left\{\frac{\partial}{\partial x_i}\frac{\partial}{\partial x_j} f(\mathbf{x})\right\} = n_i n_j \frac{\partial^2}{\partial^2 s}\widehat{f}(s, \mathbf{n}) \tag{B.7}$$

D Transform of Dirac's delta

$$R\{\delta(\mathbf{x})\} = \delta(s) \tag{B.8}$$

Bibliography

A. Asadpoure and S. Mohammadi. Developing new enrichment functions for crack simulation in orthotropic media by the extended finite element method. *International Journal for Numerical Methods in Engineering*, 69:2150–2172, 2007.

M. Avellaneda and G. Harshe. Magnetoelectric effect in piezoelectric/magnetostrictive multiplayer (2–2) composites. *Journal of Intelligent Material Systems and Structures*, 5:501–513, 1994.

I. Babuska and J. Melenk. The partition of unity method. *International Journal for Numerical Methods in Engineering*, 4:607–632, 1997.

D. Barnett and J. Lothe. Dislocations and line charges in anisotropic piezoelectric insulators. *Phys. stat. sol.*, 76:105–111, 1975.

E. Béchet, M. Scherzer, and M. Kuna. Application of the X-FEM to the fracture of piezoelectric materials. *International Journal for Numerical Methods in Engineering*, 77:1535–1565, 2009.

T. Belytschko and T. Black. Elastic crack growth in finite elements with minimal remeshing. *International Journal for Numerical Methods in Engineering*, 45:601–620, 1999.

Y. Beneviste. Magnetoelectric effect in fibrous composites with piezoelectric and piezomagnetic phases. *Physical Review*, B 51:16424–16427, 1995.

C. Brebbia and J. Domínguez. *Boundary Elements: An Introductory Course (second edition)*. Computational Mechanics Publications, 1992.

G. Daví and A. Milazzo. Multidomain boudary integral formulation for piezoelectric materials fracture mechanics. *International Journal of Solids and Structures*, 38:7065–7078, 2001.

S. Deans. *The Radon transform and some of its applications*. Wiley-Interscience Publication, 1983.

M. Denda. BEM analysis of semipermeable piezoelectric cracks. *Key Engineering Materials*, 383:67–84, 2008.

M. Denda, Y. Araki, and Y. Yong. Time-harmonic BEM for 2-d piezoelectricity applied to eigenvalue problems. *International Journal of Solids and Structures*, 26:7241–7265, 2004.

J. Dolbow. *An Extended Finite Element Method with Discontinuous Enrichment for Applied Mechanics)*. PhD thesis, Northwestern University, USA, 1999.

J. Dominguez. *Boundary Elements in Dynamics*. Computational Mechanics Publications, 1993.

A. Eringen and E. Suhubi. *Elastodynamics, Vol. 2: Linear Theory*. Academic Press, New York, 1975.

W. Feng and E. Pan. Dynamic fracture behavior of an internal interfacial crack between two dissimilar magneto-electro-elastic plates. *Engineering Fracture Mechanics*, 75:1468–1487, 2008.

W. Feng and R. Su. Dynamic internal crack problem of a functionally graded magneto-electro-elastic strip. *International Journal of Solids and Structures*, 43:5196–5216, 2006.

W. Feng, E. Pan, and X. Wang. Dynamic fracture analysis of a penny-shaped crack in a magnetoelectroelastic layer. *International Journal of Solids and Structures*, 44:7955–7974, 2007.

C. Gao, H. Kessler, and H. Balke. Crack problems in magnetoelectroelastic solids. part i: exact solution of a crack. *International Journal of Engineering Science*, 41:969–981, 2003a.

C. Gao, H. Kessler, and H. Balke. Crack problems in magnetoelectroelastic solids. part ii: General solution of collinear cracks. *International Journal of Engineering Science*, 41:983–994, 2003b.

C. Gao, P. Tong, and T. Zhang. Interfacial crack problems in magneto-electroelastic solids. *International Journal of Engineering Science*, 41: 2105–2121, 2003c.

C. Gao, P. Tong, and T. Zhang. Fracture mechanics for a mode III crack in a magnetoelectroelastic solid. *International Journal of Solids and Structures*, 41:6613–6629, 2004.

F. García-Sánchez. *Numerical study of fracture problems in anisotropic elastic and piezoelectic solids (in Spanish. English version available).* PhD thesis, University of Sevilla, Spain, 2005.

F. García-Sánchez and C. Zhang. A comparative study of three bem for trnasient dynamic crack analysis of 2-d anisotropic solids. *Computational Mechanics Fracture Mechanics*, 40:753–769, 2007b.

F. García-Sánchez, A. Sáez, and J. Domínguez. Traction boundary elements for cracks in anisotropic solids. *Engineering Analysis with Boundary Elements*, 28:667–676, 2004.

F. García-Sánchez, A. Sáez, and J. Domínguez. Anisotropic and piezoelectric materials fracture analysis by BEM. *Computer and Structures*, 83: 804–820, 2005a.

F. García-Sánchez, A. Sáez, and J. Domínguez. Two-dimensional time-harmonic BEM for cracked anisotropic solids. *Engineering Analysis with Boundary Elements*, 2005b.

F. García-Sánchez, C. Zhang, and A. Sáez. 2-d transient dynamic analysis of cracked piezoelectric solids by a time-domain BEM. *Computer Methods in Applied Mechanics and Engineering*, 197, 33-40:3108–3121, 2008a.

F. García-Sánchez, C. Zhang, and A. Sáez. A two-dimensional time-domain boundary element method for dynamic crack problems in anisotropic solids. *Engineering Fracture Mechanics*, 75, 33-40:1412–1430, 2008b.

L. Gaul and M. Schanz. A comparative study of three boundary element approaches to calculate the transient response of viscoeleastic solids with unbounded domains. *Computer Methods in Applied Mechanics and Engineering*, 179:11–123, 1999.

K. Graff. *Wave motion in elastic solids*. Oxford University press, 1975.

D. Graffi. Sul teorema di reciprocitá nella dinamica dei corpi elastici. *Mem. Accad. Sci., Bologna*, Ser 10, Vol 4:103–111, 1946.

T. Hao and Y. Shen. A new electrical boundary condition of electric fracture

mechanics and its applications. *Engineering Fracture Mechanics*, 47:793–802, 1994.

H. Hong and J. Chen. Derivations od integral equations of elasticity. *ASCE*, 114:1028–1044, 1988.

K. Hu and G. Li. Constant moving crack in a magnetoelectroelastic material under anti-plane shear loading. *International Journal of Solids and Structures*, 42:2823–2835, 2005.

K. Hu, Y. L. Kang, and G.Q. Moving crack at the interface between two dissimilar magnetoelectroelastic materials. *Acta Mechanica*, 182:1–16, 2006.

N. Iokamidis. A new singular integral equation for the classical crack problem in plane and antiplane elasticity. *International Journal of Fracture*, 21:115–122, 1983.

H. Ishikawa. Application of the BEM to anisotropic crack problems. In M. A. y C.A. Brebbia, editor, *Advances in boundary element methods for fracture mechanics*, Computational mechanics publications. Southampton and Elsevier Applied Science, London, 1990.

X. Jiang and E. Pan. Exact solution for 2d polygonal inclusion problem in anisotropic magnetoelectroelastic full-, half-, and bimaterial-planes. *International Journal of Solids and Structures*, 41:4361–4382, 2004.

C. Landis. Energetically consistent boundary conditions for electromechanical fracture. *International Journal of Solids and Structures*, 41:6291–6315, 2004.

S. Lekhnitskii. *Theory of elasticity of an anisotropic elastic body*. Holden-Day, San Francisco, 1963.

J. Li and M. Dunn. Micromechanics of magnetoelectroelastic composite materials: average field and effective behavior. *Journal of Intelligent Material Systems and Structures*, 9:404–416, 1998.

X. Li. Dynamic analysis of a cracked magnetoelectroelastic medium under antiplane mechanical and inplane electric and magnetic impacts. *International Journal of Solids and Structures*, 42:3185–3205, 2005.

J. Liang. The dynamic behavior of two parallel symmetric cracks in functionally graded piezoelectric/piezomagnetic materials. *Archive of Applied Mechanics*, 78:443–464, 2008.

J. Liu, X. Liu, and Y. Zhao. Green's functions for anisotropic magnetoelectroelastic solids with an elliptical cavity or a crack. *International Journal of Engineering Science*, 39:1405–1418, 2001.

C. Lubich. Convolution quadrature and discretized operational calculus. part i. *Numerische mathematik*, 52:129–145, 1988a.

C. Lubich. Convolution quadrature and discretized operational calculus part ii. *Numerische mathematik*, 52:413–425, 1988b.

D. Ludwig. The radon transform on euclidean space. *Communications on pure and applied mathematics*, 19:49–81, 1966.

J. Martínez and J. Domínguez. On the use of quarte-point boundary elements for stress intensity factor computations. *International Journal for Numerical Methods in Engineering*, 20:1941–1950, 1984.

N. Möes, J. Dolbow, and T. Belytschko. A finite element method for crack growth without remeshing. *International Journal for Numerical Methods in Engineering*, 46:131–150, 1999.

M. Mußchelichwilli. *Einige Grundaufgaben zur mathematischen Elastizitaetstheorie*. VEB Fachbuchverlag: Leipzig, 1971.

C.-W. Nan. Magnetoelectric effect in composite of piezoelectric and piezomagnetic phases. *Physics Review*, B 50:6082–6088, 1994.

Y. Pak. Linear electro-elastic fracture mechanics of piezoelectric materials. *International Journal of Fracture*, 54:79–100, 1992.

E. Pan. A general BEM analysis of 2D linear elastic fracture mechanics. *International Journal of Fracture*, 88:41–59, 1997.

E. Pan. A BEM analysis of fracture mechanics in 2d anisotropic piezoelectric solids. *Engineering Analysis with Boundary Elements*, 23:67–76, 1999.

S. Park and C. Sun. Fracture criteria for piezoelectric ceramics. *Journal of American Ceramics Society*, 78:1475–1480, 1995.

V. Parton and B. Kudryatsev. *Electromagnetoelasticity*. Gordon and Breach science publisher, New York, 1988.

A. Portela, M. Aliabadi, and D. Rooke. The dual BEM: effective implementation for crack problems. *International Journal for Numerical Methods in Engineering*, 33:1269–1287, 1992.

B. Rao and M. Kuna. Interaction integrals for fracture analysis of functionally graded magnetoelectroelastic materials. *International Journal of Fracture*, 153:15–37, 2008.

B. Rao and M. Kuna. Erratum to: Interaction integrals for fracture analysis of functionally graded magnetoelectroelastic materials. *International Journal of Fracture*, 161:199–201, 2010.

J. Réthoré, S. Roux, and F. Hild. Hybrid analytical and extended finite element method (HAX-FEM): A new enrichment procedure for cracked solids. *International Journal for Numerical Methods in Engineering*, 81 (3):269–285, 2009.

J. Rice. A path independent integral and the approximate analysis of strain concentration by notches and cracks. *Journal of Applied Mechanics*, 33: 379–386, 1968.

A. Sáez and J. Domínguez. Far field dynamic green's functions for bem in transversely isotropic solids. *Wave motion*, 32 (2):113–123, 2000.

A. Sáez, R. Gallego, and J. Domínguez. Hypersingular quarter-point boundary elements for crack problems. *International Journal for Numerical Methods in Engineering*, 38:1681–1701, 1995.

A. Sáez, F. García-Sánchez, and J. Domínguez. Hypersingular BEM for dynamic fracture in 2-d piezoelectric solids. *Computer Methods in Applied Mechanics and Engineering*, 196:235–246, 2006.

G. Savin. *Distribution of Stresses at Holes*. Naukova Dumka: Kiev, 1968.

M. Schanz. A boundary element formulation in time domain for viscoelastic solids. *Communications in Numerical Methods in Engineering*, 15:799–809, 1999.

M. Schanz. *Wave propagation in viscoelastic and poroelastic continua*. Springer-Verlag, Berlin, Heidelberg, 2001.

M. Scherzer and M. Kuna. Combined analytical and numerical solution of 2d interface corner configurations between dissimilar piezoelectric materials. *International Journal of Fracture*, 153:61–99, 2004.

Y. Shindo and E. Ozawa. Dynamic analysis of a cracked piezoelectric material. In R. Hsieh, editor, *Mechanical Modelling of New Electromagnetic Materials*. Elsevier, 1990.

G. Sih and E. Chen. Dilatational and distortional behavior of cracks in magnetoelectroelastic materials. *Theoretical and Applied Fracture Mechanics: Mechanics and Physics of Fracture*, 40:1–21, 2003b.

G. Sih and Z. Song. Magnetic and electric poling effects associated with crack growth in $batio_3$-$cofe_2o_4$ composite. *Theoretical and Applied Fracture Mechanics: Mechanics and Physics of Fracture*, 39:209–227, 2003a.

G. Sih, R. Jones, and Z. Song. Piezomagnetic and piezoelectric poling effects on mode I and II crack initiation behavior of magnetoelectroelastic materials. *Theoretical and Applied Fracture Mechanics: Mechanics and Physics of Fracture*, 40:161–186, 2003c.

J. Sladek, V. Sladek, P. Solek, and E. Pan. Fracture analysis of cracks in magneto-electro-elastic solids by the MLPG. *Computational Mechanics*, 42:697–714, 2008.

M. Snyder and T. Cruse. Boundary-integral analysis of anisotropic cracked plates. *International Journal of Fracture mechanics*, 315-328, 1975.

A. Soh and J. Liu. On the constitutive equations of magnetoelectroelastic solids. *Journal of Intelligent Material Systems and Structures*, 16:597–602, 2005.

P. Sollero. *Fracture analysis of anisotropic composite laminates by the boundary element method*. PhD thesis, Wessex Institute of Technology, UK, 1994.

P. Sollero and M. Aliabadi. Anisotropic analysis of cracks in composite laminates using the dual BEM. *Composite Structures*, 31:229–233, 1995.

Z. Song and G. Sih. Crack initiation behavior in magnetoelectroelastic composite under in-plane deformation. *Theoretical and Applied Fracture Mechanics: Mechanics and Physics of Fracture*, 39:189–207, 2003.

H. Sosa. Plane problems in piezoelectric media with defects. *International Journal of Solids and Structures*, 28:491–505, 1991.

H. Stehfest. Comun. algorithm 368: numerical inversion of laplace transform; an overview and recent developments. *Computational Methods in Applied Mechanics and Engineering*, 139:3–47, 1996.

A. Stroh58. Dislocation and racks in anisotrpic elasticity. *Philosophical magazine*, 3:625–646, 1958.

R. Su, W. Feng, and J. Liu. Transient response of interface cracks between dissimilar magneto-electro-elastic strips under out-ofplane mechanical and in-plane magneto-electrical impact loads. *Composite Structures*, 78:119–128, 2007.

N. Sukumar, Z. Y. Huang, J.-H. Prévost, and Z. Suo. Partition of unity enrichment for bimaterial interface cracks. *International Journal for Numerical Methods in Engineering*, 59:1075–1102, 2004.

Z. Suo, C.-M. Kuo, D. Barnett, and J. Willis. Fracture mechanics for

piezoelectric ceramics. *Journal of Mechanics and Physics of Solids*, 4: 739–765, 1992.

A. Tan, S. Hirose, C. Zhang, and C.-Y. Wang. A time-domain BEM for transient wave scattering analysis by a crack in anisotropic solids. *Engineering Analysis with Boundary Elements*, 29:610–623, 2005a.

A. Tan, S. Hirose, and C. Zhang. A time-domain collocation-galerkin BEM for transient dynamic crack analysis in anisotropic solids. *Engineering Analysis with Boundary Elements*, 29:1025–1038, 2005b.

W. Tian and U. Gabbert. Multiple crack interaction problem in magnetoelectroelastic solids. *European Journal of Mechanics - A/Solids*, 23: 599–614, 2004.

W. Tian and R. Rajapakse. Fracture analysis of magnetoelectroelastic solids by using path independent integrals. *International Journal of Fracture*, 131:311–335, 2005b.

W. Tian and R. Rajapakse. Theoretical modelling of a conducting crack in a magnetoelectroelastic solid. *International Journal of Applied Electromagnetics and Mechanics*, 22:141–158, 2005c.

T. Ting. *Anisotropic Elasticity*. Oxford University Press, New York, 1996.

B. Wang and J. Han. Discussion on electromagnetic crack face boundary conditions for the fracture mechanics of magneto-electro-elastic materials. *Acta Mechanica Sinica*, 22:233–242, 2006b.

B. Wang and Y. Mai. Crack tip field in piezoelectric/piezomagnetic media. *European Journal of Mechanics - A/Solids*, 22:591–602, 2003.

B. Wang and Y. Mai. Fracture of piezoelectromagnetic materials. *Mechanics Research Communications*, 31:65–73, 2004.

B. Wang and Y. Mai. Applicability of the crack-face boundary conditions for fracture of magnetoelectroelastic materials. *International Journal of Solids and Structures*, 44:387–398, 2006.

B. Wang and Y. Mai. Self-consistent analysis of coupled magnetoelectroelastic fracture. theoretical investigation and finite element verification. *Computer Methods in Applied Mechanics and Engineering*, 196: 2044–2054, 2007.

C.-Y. Wang and J. Achenbach. Elastodynamic fundamental solutions for anisotropic solids. *Geophysical Journal International*, 18:384–392, 1994.

C.-Y. Wang and J. Achenbach. 3-d time-harmonic elastodynamic green's functions for anisotropic solids. *Procceedings Royal Society of London*, A449:441–458, 1995.

C.-Y. Wang and C. Zhang. 3-d and 2-d dynamic green's functions and time-domain BIEs for piezoelectric solids. *Engineering Analysis with Boundary Elements*, 29:454–465, 2005.

H. Yong and Y. Zhou. Transient response of a cracked magnetoelectroelastic strip under anti-plane impact. *International Journal of Solids and Structures*, 44:705–717, 2007.

C. Zhang. Transient elastodynamic antiplane crack analysis of anisotropic solids. *International Journal of Solids and Structures*, 37:6107–6130, 2000.

C. Zhang. A 2-d time-domain BIEM for dynamic analysis of cracked orthotropic solids. *Computer Modelling in Engineering and Sciences*, 3: 381–398, 2002a.

C. Zhang. A 2d hypersingular time–domain traction BEM for transient elastodynamic crack analysis. *Wave Motion*, 35:17–40, 2002b.

C. Zhang. Transient dynamic crack analysis in anisotropic solids. In A. Ivankovic and M. Aliabadi, editors, *Crack Dynamics*. WIT Press, Southampton, Boston, 2005.

X. Zhong, X.-F. Li, and K. Lee. Transient response of a cracked magneto-electric material under the action of in-plane sudden impacts. *Computational Materials Science*, 45:905–911, 2009.

Z.-G. Zhou and B. Wang. Scattering of harmonic anti-plane shear waves by an interface crack in magneto-electro-elastic composites. *Applied Mathematics and Mechanics*, 26:17–26, 2005a.

Z.-G. Zhou and B. Wang. Dynamic behavior of two parallel symmetry cracks in magneto-electro-elastic composites under harmonic anti-plane waves. *Applied Mathematics and Mechanics*, 27:583–591, 2006a.

Z.-G. Zhou and B. Wang. An interface crack between two dissimilar functionally graded piezoelectric/piezomagnetic material half infinite planes subjected to the harmonic anti-plane shear stress waves. *International Journal of Applied Electromagnetics and Mechanics*, 27:117–132, 2008.

Z.-G. Zhou, L.-Z. Wu, and B. Wang. The dynamic behavior of two collinear interface cracks in magneto-electro-elastic materials. *European Journal of Mechanics, A/Solids*, 24:253–262, 2005b.

Z.-G. Zhou, L.-Z. Wu, and S.-Y. Du. The dynamic behavior of two parallel interface cracks in magneto-electro-elastic materials under the harmonic anti-plane shear stress waves. *Strength, Fracture and Complexity*, 4:169–184, 2006b.

Publications

The present work has given rise to the following national and international publications.

Journal Papers

International

- R. Rojas-Díaz, F. García-Sánchez, A. Sáez. Analysis of cracked magnetoelectroelastic composites under time-harmonic loading. *International Journal of Solids and Structures*,**47**:71–80, 2010.
- R. Rojas-Díaz, F. García-Sánchez, A. Sáez, Ch. Zhang. Dynamic crack interactions in magnetoelectroelastic composite materials. *International Journal of Fracture*, **157**:119-130, 2009.
- R. Rojas-Díaz, A. Sáez, F. García-Sánchez, Ch. Zhang. Time-harmonic Green's functions for anisotropic magnetoelectroelasticity. *International Journal of Solids and Structures*, **45**:144-158, 2008.
- R. Rojas-Díaz, F. García-Sánchez, A. Sáez, Ch. Zhang. Fracture analysis of magnetoelectroelastic composite materials. *Key Engineering Materials*, **348-349**:69-72, 2007.
- F. García-Sánchez, R. Rojas-Díaz, A. Sáez, Ch. Zhang. Fracture of magnetoelectroelastic composite materials using boundary element method (BEM). *Theoretical and Applied Fracture Mechanics: Mechanics and Physics of Fracture*, **47**:192-204, 2007.

- R. Rojas-Díaz, N. Sukumar, A. Sáez, F. García-Sánchez. Fracture in Magnetoelectroelastic Materials using the Extended Finite Element Method. Submitted for publication to *International Journal of Numerical Methods in Engineering*.
- R. Rojas-Díaz, F. García-Sánchez, A. Sáez, Ch. Zhang. Fracture Analysis of plane piezoelectric/piezomagnetic multiphase composites under transient loading. Submitted for publication to *Computer Methods in Applied Mechanics and Engineering*.
- R. Rojas-Díaz, M. Denda, A. Sáez, F. García-Sánchez. Dual BEM Analysis of different crack faces boundary conditions in magnetoelectroelastic solids. Submitted for publication to *European Journal of Mechanics - A/Solids*.

National

- F. García-Sánchez, R. Rojas-Díaz, A. Sáez. Formulación del Método de los Elementos de Contorno para problemas dinámicos transitorios de fractura en sólidos magnetoelectroelásticos. *Anales de Mecánica de la Fractura*, **2**:445-450, 2008.
- A. Sáez, R. Rojas-Díaz, F. García-Sánchez. Modelo numérico para problemas de fractura en materiales compuestos magnetoelectroelásticos bajo carga dinámica armónica. *Anales de Mecánica de la Fractura*, **2**:439-444, 2008.
- R. Rojas-Díaz, F. García-Sánchez, A. Sáez. Simulación numérica de fractura en sólidos magnetoelectroelásticos. *Anales de Mecánica de la Fractura*, **2**:439-444, 2008.

Conferences papers

International

- R. Rojas-Díaz, M. Denda, F. García-Sánchez, A. Sáez. Hypersingular BEM analysis of semipermeable cracks in magnetoelectroelastic solids. *BeTeq 2010* July 12^{th}-14^{th}, Berlin, Germany
- R. Rojas-Díaz, A. Sáez, N. Sukumar, F. García-Sánchez. Unified formulation of the XFEM for fully anisotropic multifield problems based on the Stroh's formalism. *IV European Conference on Computational Mechanics*, May, 16^{th}-21^{th}, 2010, Paris, France
- R. Rojas-Díaz, N. Sukumar, A. Sáez, F. García-Sánchez. Crack Analysis in magnetoelectroelastic media using the Extended Finite Element Method. *X-FEM 2009: The International Conference on Extended Finite Element Method-Recent Developments and Applications*, September, 28^{th}-30^{th}, Aachen, Germany
- R. Rojas-Díaz, F. García-Sánchez, A. Sáez, Ch. Zhang. A 2D hypersingular BEM for transient analysis of cracked magnetoelectroelastic solids. *BeTeq 2008* July 9^{th}-11^{th}, Seville, Spain (Keynote Lecture)
- A. Sáez, R. Rojas-Díaz, F. García-Sánchez. Crack Interaction in plane Magnetoelectroelastic solids under Dynamic Loading. *ECCOMAS 2008: Proceedings of the 8^{th} World Congress on Computational Mechanics and 5^{th} European Congress on Computational Methods in Applied Sciences and*

Engineering, June 30^{th}- July 4^{th}, Venice, Italy

- R. Rojas-Díaz, A. Sáez, F. García-Sánchez. Fracture Analysis of magnetoelectroelastic media under dynamic loading. *Inaugural Conference of the Engineering Mechanics Institute*, May 18^{th}- 21^{st}, Minneapolis (USA)
- R. Rojas-Díaz, A. Sáez, F. García-Sánchez, Ch. Zhang. Fracture Analysis of magnetoelectroelastic solids under time-harmonic loading. *BeTeq 2007*: July, 24^{th}-26^{th} , Naples, Italy
- F. García-Sánchez, A. Sáez, R. Rojas-Díaz, Ch. Zhang. Dual BEM for Fracture Analysis of magnetoelectroelastic solids. *BeTeq 2006*: September, 4^{th}-6^{th} , Paris, France

National

- R. Rojas-Díaz, N. Sukumar, A. Sáez, F. García-Sánchez. Simulación Numérica de Problemas de Fractura en Materiales Magnetoelectroelásticos mediante X-FEM. *MetNum09*, June 29^{th} - July 2^{nd}, Barcelona, Spain
- F. García-Sánchez, R. Rojas-Díaz, A. Sáez. Formulación del Método de los Elementos de Contorno para problemas dinámicos transitorios de fractura en sólidos magnetoelectroelásticos. *XXV Encuentro del GEF*, Sigüenza (Spain) March, 5^{th}-7^{th}
- R. Rojas-Díaz, F. García-Sánchez, A. Sáez. Formulación dinámica del método de los elementos de contorno para el análisis de sólidos magnetoelectroelásticos fisurados. *CMNE*: June, 14^{th}-16^{th} , Porto, Portugal
- R. Rojas-Díaz, F. García-Sánchez, A. Sáez. Simulación numérica

de fractura en sólidos magnetoelectroelásticos. *XXIV Encuentro del GEF*, March 21^{st}-23rd, Burgos, Spain